RADAR INTERFEROMETRY AND ITS APPLICATION TO CHANGES IN THE EARTH'S SURFACE

Didier Massonnet
Department of Radar Systems Performance
Centre National d'Etudes Spatiales
Toulouse, France

Kurt L. Feigl
Department of Terrestrial and Planetary Dynamics
Centre National de la Recherche Scientifique
Toulouse, France

Abstract. Geophysical applications of radar interferometry to measure changes in the Earth's surface have exploded in the early 1990s. This new geodetic technique calculates the interference pattern caused by the difference in phase between two images acquired by a spaceborne synthetic aperture radar at two distinct times. The resulting interferogram is a contour map of the change in distance between the ground and the radar instrument. These maps provide an unsurpassed spatial sampling density (~100 pixels km^{-2}), a competitive precision (~1 cm), and a useful observation cadence (1 pass $month^{-1}$). They record movements in the crust, perturbations in the atmosphere, dielectric modifications in the soil, and relief in the topography. They are also sensitive to technical effects, such as relative variations in the radar's trajectory or variations in its frequency standard. We describe how all these phenomena contribute to an interferogram. Then a practical summary explains the techniques for calculating and manipulating interferograms from various radar instruments, including the four satellites currently in orbit: ERS-1, ERS-2, JERS-1, and RADARSAT. The next chapter suggests some guidelines for interpreting an interferogram as a geophysical measurement: respecting the limits of the technique, assessing its uncertainty, recognizing artifacts, and discriminating different types of signal. We then review the geophysical applications published to date, most of which study deformation related to earthquakes, volcanoes, and glaciers using ERS-1 data. We also show examples of monitoring natural hazards and environmental alterations related to landslides, subsidence, and agriculture. In addition, we consider subtler geophysical signals such as postseismic relaxation, tidal loading of coastal areas, and interseismic strain accumulation. We conclude with our perspectives on the future of radar interferometry. The objective of the review is for the reader to develop the physical understanding necessary to calculate an interferogram and the geophysical intuition necessary to interpret it.

CONTENTS

1. INTRODUCTION

1.1. Radar Images

The idea of imaging the Earth by radar arose in the late 1950s, but scientific use began with the *Seasat* satellite in 1978. (Terms in italics are defined in the glossary following the main text.) Since a radar is primarily a tool for measuring the distance of objects (hence the name, an acronym for "radio detection and ranging"), the early images of ground echoes were first considered to be undesirable noise. They became a useful signal to study large areas as radars were installed on airplanes and later satellites. The physics of the radar leads to a special imaging geometry (Figure 1): *cross-track* resolution results from ordering the echoes received from each emitted pulse by their round trip travel time, while the forward motion of the plane or satellite repeats the observation. For a useful collection of papers on the

Reviews of Geophysics, 36, 4 / *November 1998*
pages 441–500
8755-1209/98/97RG-03139*$15.00*
Paper number 97RG03139

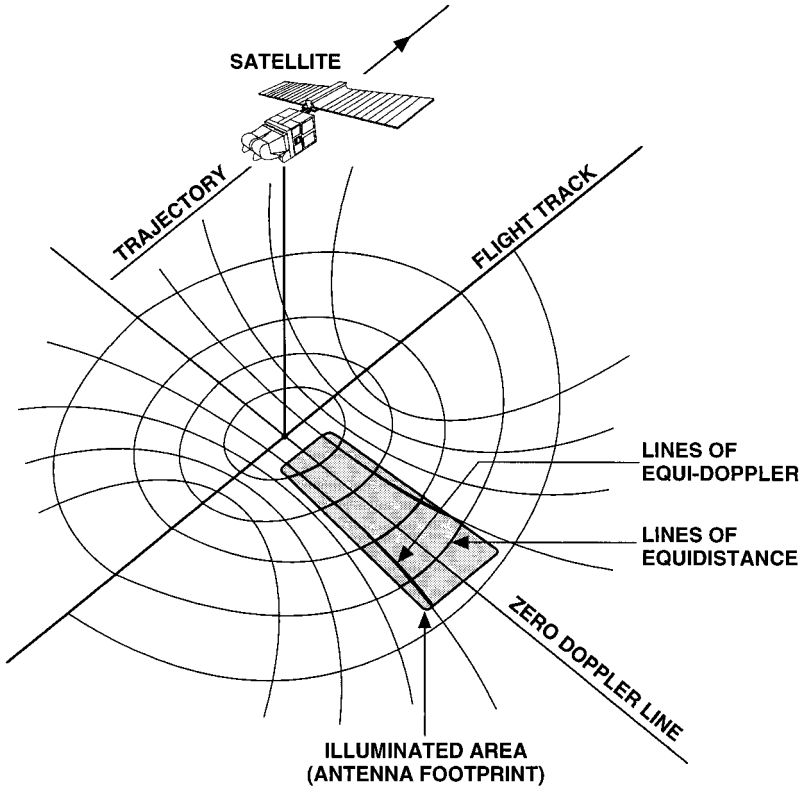

Figure 1. Imaging geometry of a side-looking radar. Two different principles help improve the resolution in a radar image. First, the samples of the returning signal are sorted according to their round trip flight time. Second, the Doppler frequency shift is then used to sort the samples along the direction of the flight. To combine these two principles and optimize resolution in both dimensions, the radar must "look to the side," perpendicular to its trajectory. Redrawn from *Kovaly* [1976] and *Elachi* [1987].

development of these issues, see *Kovaly* [1976]. For an instructive introduction to radar imagery, *Elachi* [1982, 1987] provides several well-illustrated examples. For a history of the technical developments in synthetic aperture radar (*SAR*) instruments, we recommend the first chapter of *Curlander and McDonough* [1991]. Imaging radars transmit and receive electromagnetic waves with wavelengths in the range of *X band* (3 cm), *C band* (6 cm), or *L band* (24 cm). The waves propagate through atmospheric media (e.g., clouds, fog, smoke and aerosols) without noticeable signal loss, providing all-weather and nighttime capabilities. These two advantages over optical techniques are important for monitoring rapid phenomena or in mapping cloudy places. At the time of this writing, four civilian satellites provide radar images useful for interferometric applications in geophysics: *ERS-1*, *ERS-2*, *JERS-1*, and *RADARSAT* (Table 1).

1.1.1. Synthesis and geometric properties. The natural resolution of an orbiting radar instrument observing from 1000 km is typically 10 km on the ground. This is a direct consequence of the ratio of wavelength to aperture, about 10^{-3} for a large-aperture system with an antenna size of ~10 m. For comparison, large optical telescopes of comparable size have a wavelength/aperture ratio of 10^{-8}. To improve the resolution, the synthetic aperture radar technique focuses the image. In SAR the satellite must not cover more than half of the *along-track* antenna length between the emission of successive pulses. For example, a 10-m antenna should advance only 5 m between pulses, to produce a 5-m-long final elementary resolution cell (pixel). For a satellite traveling ~6 km s^{-1} over the ground, this implies a pulse repetition frequency of ~1 kHz. For a C band instrument 1000 km from its target, the radar footprint is about 5 km long along track. We must then sort out a collection of signals, each one of which is a mixture of a thousand 5-m samples, each of which contributes to a thousand signals. Inverting this problem involves reconstructing the contribution from each 5-m cell, by a technique similar to tomography, called synthetic aperture processing, or focusing. The result is typically a thousandfold improvement in resolution, equivalent to using an imaginary antenna with a "synthetic" aperture of 20 km (Figure 2). The technique is computationally intensive, requiring some 300 billion operations. To focus a 100 km by 100 km scene requires about an hour on a typical workstation in the mid-1990s. There are several algorithms: range Doppler [*Wu et al*., 1981; *Curlander and McDonough*, 1991], seismic migration [*Prati et al*., 1990], *PRISME* architecture [*Massonnet et al*., 1994b], or chirp scaling [*Raney*, 1991; *Raney et al*., 1994]. All these algorithms are equivalent for SAR interferometry provided that they preserve the phase. They must not introduce artificial phase changes that could prevent further interferometric combination of images, as would random phase changes, or allow a misinterpretation of the result, as would structured phase changes.

The mathematical reconstruction profoundly changes the geometry of the radar image (Figure 1). Each point on the image is referred to a coordinate frame defined by the position and velocity vectors of the satellite,

TABLE 1. Characteristics of Civilian Radar Satellites Suitable for Interferometry

Abbreviation	*Name*	*Launch Date*	*Wavelength, mm*	*Band*	*Orbital Repetition Cycle, days*	*Unit Vector § From Ground to Satellite at 35°N Latitude, Midswath and "Descending" Orbit (East, North, Up)*	*Mean Incidence Angle, deg*	*Data Recorder on Board?*
SEASAT[a]		1978	235	L	3		23	no
ERS-1[b]	European Remote Sensing Satellite 1	1991	56.7	C	3, 35, 168	[−0.33, +0.07, +0.94]	23	no
ERS-2[c]	European Remote Sensing Satellite 2	1995	56.7	C	35	[−0.33, +0.07, +0.94]	23	no
JERS-1[d]	Japanese Earth Resource Satellite 1	1992	235	L	44	[−0.61, +0.11, +0.79]	35	yes
RADARSAT[e]		1995	57.7	C	24	variable	variable	yes
SIR-C[f]	Shuttle Imaging Radar C	1994		X, C, L	variable	variable	variable	yes
ENVISAT[g]				C			variable	yes
SRTM[h]	Shuttle Radar Topography Mission	2000	56	C	35		wide swath	yes
ALOS[i]	Advanced Land Observation Satellite	2003	235	L				yes
ECHO Elsie[j]	Earth Change and Hazard Observatory	2003	235, 56.7	L, C	3, 8, 35	variable	variable	yes

[a]See Plate 4 and *Gabriel et al*. [1989].

[b]The orbital history of ERS-1 includes seven distinct phases using five different cycles of 3, 35, and 168 days. Data from any of the 35-day phases can be combined to form an interferogram. Data from the two different 3-day phases cannot. The same applies to the two different 168-day cycles. No new acquisitions with a 3-day cycle are planned. See *Scharroo and Visser* [1998].

[c]In the "tandem" mission of ERS-1 and ERS-2, the two satellites use the same 35-day orbital cycle, but shifted by 1 day. Since ERS-1 and ERS-2 images can form interferograms together, such tandem interferograms span only one day, minimizing temporal decorrelation.

[d]The JERS-1 satellite produces images of a lower quality than ERS because the signal-to-noise ratio is smaller and the radar is more sensitive to pollution by ground radars [*Rossi et al*., 1996]. It was used to image the Northridge earthquake [*Massonnet et al*., 1996a; *Murakami et al*., 1996].

[e]The variable resolutions and incidence angles in the RADARSAT data set will reduce the probability of obtaining long series of images under identical conditions, as is required for interferometric applications. *Vachon et al*. [1995] compare the interferometric capabilities of ERS-1 and RADARSAT, which cannot form interferograms together. RADARSAT 2, planned for launch in 2001, will feature improved resolution and should offer some interoferometric compatibility with RADARSAT 1.

[f]The space shuttle is the only platform to carry an X band (3-cm wavelength) radar [*Moreira et al*., 1995; *Coltelli et al*., 1996]. The shuttle offers the interesting possibility of comparing C band and L band interferograms for the same scenes acquired at the same time; see *Rosen et al*. [1996] and section 3.1.

[g]The European Space Agency plans to launch ENVISAT at the turn of the century. Like RADARSAT, ENVISAT is a complex satellite equipped with a radar with multiple possibilities in terms of pointing. ENVISAT data will not be compatible with ERS data for calculating interferograms. See *McLeod et al*. [1998].

[h]For mapping topographic relief, SRTM will yield an elevation model covering 80% of the Earth's land surface, except near the poles, with a vertical accuracy of better than 16 m. SRTM will use the same radar instrument as SIR-C and an additional C band imaging antenna at the end of a 60-m boom, allowing interferometry with a single pass but eliminating the possibility of detecting group movements. The Defense Mapping Agency (DMA) plans to use the radar data from the SRTM to fulfill a joint defense requirement for a digital global terrain elevation map with data points spaced approximately every 30 m. If made public, this map will offer a substantial improvement over the 100-m posting of the current best elevation model for most of the globe. Called the Digital Terrain Elevation Data (DTED), the current elevation model is based on stereoscopic analysis photographs acquired from high-altitude aircraft and satellites. It covers only 65% of the Earth's land mass. The DMA has not made the DTED available to the public for areas outside the United States.

[i]ALOS is a follow-on to JERS-1 that will include active array SAR with variable incidence angle and a low-resolution scansar mode. Pixel size is planned to be 10 m. Orbit will be polar at 700 km. Precision orbit keeping is planned to make interferometry easier. It is not clear whether ALOS images will not be interferometrically compatible with JERS-1 images.

[j]Proposed by NASA and Centre National d'Etudes Spatiales. See section 5.

independently of the instrument's orientation. Consequently, we know the position of each point on a radar image to within the resolution of the image, if its topographic elevation is known. By working with two images acquired in crossing orbital trajectories, a point recognized in both images can be absolutely positioned without prior knowledge of its elevation. In contrast, the geometric precision of optical images depends on imprecise knowledge of the orientation angles of the instrument, requiring the use of control points. This feature alone turns a space imaging radar into an extraordinary geodetic tool that could estimate the geodetic coordinates of millions of points with accuracy of the order of 1 m. This property has not been sufficiently recognized and applied on a large scale.

The radar imaging geometry inherits a drawback from sorting the echos by their distance from the antenna. In mountainous areas, several points in a pulse line may share the same distance to the instrument and therefore will mix their contributions in the same range pixel. This phenomenon, called "layover," occurs where the average topographic slope between two points exceeds the incidence angle of the radar. For a radar with steep incidence, like ERS-1 or SEASAT (23° from vertical on average), many areas appear overlaid.

1.1.2. Properties of image amplitude. The amplitude of the radar image records reflectivity, the variable ability of the terrain to send the incident energy back to the radar. A calm lake appears dark in a radar image because the water surface acts as a perfect reflector, sending the radar signal away from the satellite. For the same reason, you cannot see yourself in a mirror unless you are in front of it. If the surface of the water is ruffled, reflective facets comparable in size to the wavelength are not directional and transmit part of the energy back to the radar. Some of these facets may even face the radar, especially for a small angle of incidence such as that used by ERS-1. In this case, water appears bright. Most natural objects are diffuse reflectors, sending a greater or lesser part of the signal back to the radar. Multiple reflection is an efficient mechanism, mimicking a pair of mirrors at right angles. For example, trees standing in water are very bright because the reflection from the water, then from the trunks, sends the signal back toward the radar. Corner-like structures such as sidewalk curbs, windows, and roofs, as well as fault scarps or ground fissures, can create very bright returns, as can bridges over water [*Zebker and Goldstein*, 1986]. Radar waves can penetrate dry materials with low conductivity, such as soil in arid deserts, snow on very cold ice fields, or sparse vegetation [*Blom and Elachi*, 1981]. Longer wavelengths (e.g., 24-cm L band) penetrate a relatively thin tree canopy more deeply than shorter ones (e.g., 6-cm C band) [*Hagberg et al*., 1995; *Rignot*, 1996].

1.1.3. Properties of the image phase. Like all electromagnetic signals, a radar echo carries an amplitude and a *phase*. Thus the data are complex numbers, an indispensable feature for SAR focusing. The resulting high-resolution image is also complex. The phase measurement records so many different effects that it appears as a noisy image with values uniformly distributed between 0° and 360°. The phases become meaningful only when some of these effects are isolated by comparing radar images. In this way, we recover the full value of the phase information, or its geometric accuracy, as with the microwave signals used in geodetic applications of the Global Positioning System (*GPS*) [*Dixon*, 1991; *Hager et al*., 1991; *Segall and Davis*, 1997] and very long baseline interferometry (*VLBI*) [*Herring*, 1992].

1.2. Principles of Radar Phase and Interferometry

The principle of interferometry exploits carefully engineered differences between radar images. Introduced in the 1970s, the first applications involved observing the moving Moon [*Shapiro et al*., 1972; *Zisk*, 1972a, b; *Stacy and Campbell*, 1993], Venus [*Campbell et al*., 1970], or airborne radars [*Graham*, 1974]. The phases of images with a difference of position (e.g., two antennae on one plane acquire images simultaneously) or with a difference of time (e.g., one antenna acquires images at two distinct times) can be compared after proper image registration. The resulting difference of phases is a new kind of image called an interferogram. It is an interference pattern of *fringes* containing all the information on relative geometry. If certain conditions are met, it is no longer noisy (see *Gens and Van Genderen* [1996] and *Griffiths* [1995] for technical overviews). Many physical phenomena contribute to the phase measurement; these phenomena are discussed in the following subsections.

1.2.1. Phase variations within a pixel. The surface area on the ground represented by a pixel in a radar image generally contains hundreds of elementary targets. Each of these targets contributes to the pixel through a complex reflection coefficient. The phase can rotate upon reflection, depending on the dielectric properties of the target, or be delayed to a greater or lesser extent depending on the relative position of the target within the pixel. Since the wavelength is much smaller than the pixel (by a factor of about 300 for ERS-1), the phase of the pixel is the argument of a complex number that is the sum of hundreds of unknown complex numbers. The resulting phase is therefore random, while the amplitude increases stochastically with the number and the reflectivity of the elementary targets and can be partially modeled [e.g., *Beaudoin et al*., 1990; *Posner*, 1993]. Differencing the phases may, however, isolate other contributions to the phase signal, or to its changes, by eliminating the random contribution.

For this, the elementary targets must remain stable (see section 1.3.1). This condition is met if the two images are taken at the same time. A more geometric condition requires that elementary targets within a pixel contribute the same way to both images. Therefore the pixel must not stretch or shrink by more than a fraction of the wavelength from one image to the other. Otherwise, targets at both ends of a given pixel will add

Figure 2. Improvement in resolution introduced by the synthetic aperture technique. A radar satellite "illuminates" an area with dimensions equal to the natural resolution (without synthetic aperture) of the antenna in azimuth (i.e., along the track) and the width of the electromagnetic pulse in range (i.e., across the track). On the ground these values give a resolution of about 5 km in azimuth and 14 km in range for ERS. These values are also typical of other spaceborne radar systems. The left panel shows the amplitude image of a full 100 × 100 km frame acquired by ERS-1 over Crimea (southern Ukraine) as it was transmitted to the ground receiving station at Toulouse, France, on September 25, 1991, at ~2300 LT. In this image, the eye can barely distinguish the land from the sea. The synthetic aperture process leads to the full-resolution image on the right. The sea appears bright where its surface is ruffled by wind and is dark in the lee of the coast.

differently in each image, leading to internal phase contributions that do not cancel by subtraction. Mathematically, let L represent the length perpendicular to the trajectory of a pixel on the ground (~20 m for ERS-1), let λ represent the wavelength (56 mm for ERS-1), and let θ_1 and θ_2 represent the angles of incidence (from local vertical) in the first and second image, respectively. The difference in round trip distance of targets at both ends of a pixel is $2L \sin \theta$. Hence the fundamental condition for interferometry

$$2L \ (\sin \theta_1 - \sin \theta_2) < \lambda \qquad (1)$$

restricts the separation between the satellite's orbital trajectories during the two image acquisitions to typically less than 1 km (for ERS-1). Fortunately, satellite orbits are designed to repeat identically after a period of time called the orbital cycle and generally meet this condition.

The local slope of the terrain influences this condition. Close to the interferometric limit (1), even a moderate slope with the wrong orientation will blur fringes. According to (1), steep incidence, coarse resolution, and short wavelength all make the condition harder to satisfy.

Similarly, the direction of observation must also be identical for the two images; otherwise, elementary targets will sum differently in the along-track direction of the pixel. The interferogram degrades linearly with the angle between the two directions of observation. The degradation becomes total when this angle exceeds the width of the antenna beam (typically 0.3° for ERS-1). In signal-processing terms, this happens as soon as the illuminated areas (Figure 1) cease to overlap in the along-track direction, creating an excessively large difference between the "mean Doppler" of the two images.

The way the synthetic aperture algorithm constructs phase in a pixel randomly filled with scatterers practically forbids interferometric combination with two images acquired by different satellites or by the same satellite in a different orbital configuration. As a result, SAR interferometry is not possible with images from the same satellite that are separated a fraction of a full orbital cycle or that do not belong to the same orbital cycle (such as the 3-day and 35-day cycles of ERS-1). Although exceptional opportunities may occur where distinct orbits cross, such a result would have limited spatial extent. Similarly, the technique does not apply to images made with different wavelengths. ERS-1 and its twin ERS-2 produce images that can be combined, however, because they have identical radar instruments and orbits. Indeed, we shall use ERS to refer to ERS-1 or ERS-2. Once they are formed, however, interferograms of various origins can be usefully combined, as we shall see in section 2.5.4.

The user may also spoil the interferometric effect by applying slightly different processing procedures to each image. Such a slight mistake can damage the interferogram more than a huge error consistently applied to both images in the pair.

1.2.2. Contribution of the orbital trajectories. With the internal phase difference eliminated, most of the observed path difference corresponds to the difference in viewpoint caused by any shift in orbital trajectory between the two image acquisitions. The images must not shift by more than half a wavelength (that is, one fringe) per pixel, or else the interferometric effect will vanish, as was seen in the previous section. Since an image can be 6000 pixels wide (a typical swath width for radar satellite), the difference in viewpoint can commonly create hundreds of fringes. The convergence or divergence, even if less than 1 m, of the orbital trajectories over the length of the image can also create "along-track" fringes. Once all the a priori knowledge of the orbits has been used to eliminate this type of contribution, there may be residual fringes, which we can eliminate by "orbital tuning" (Plate 1; section 2.5.2). As a by-product of this procedure, the second orbital pass is positioned relative to the first to a few centimeters. This approach applies to regular satellite trajectories but not to airplane trajectories, which are much less regular and harder to repeat.

1.2.3. Contribution of the topography. Eliminating the bulk of the orbital contribution reveals an underlying stereoscopic effect, as the radar observes the topography from two slightly different points of view (section 2.4.1). This topographic contribution yields fringes which hug the topography like contour lines (Plate 2). These we call "topographic fringes." To establish orders of magnitude, it is convenient to use the notion of altitude of ambiguity, or the shift in altitude needed to produce one topographic fringe. The magnitude of this quantity h_a can range from infinity (if the satellite happens to acquire the two images from exactly the same viewpoint, eliminating the stereoscopic effect), to values of the order of 10 m (with the largest orbital separation tolerated by interferometry, and maximum stereoscopic effect). If the trajectories have a horizontal separation of d, the *altitude of ambiguity* is

$$h_a = \frac{R_s \lambda \tan \theta_m}{2d} \qquad (2)$$

where R_s is the range from the slave trajectory to the target, θ_m is the angle of incidence for the reference image, and λ is the wavelength. Figure 3 shows the general case derived in section 2.4.1. This sensitivity to topographic relief can be used to calculate a digital elevation model (*DEM*) (Plate 3). Although such models are interesting to geophysicists, they extend beyond the scope of this review. We refer interested readers to *Wolf and Wingham* [1992] for a survey of existing DEMs and to *Zebker and Goldstein* [1986] and *Zebker et al.* [1994c] for a discussion of the technique. Henceforth, we will consider the topographic contribution as an artifact.

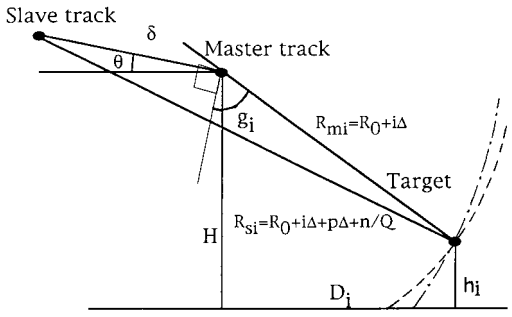

Figure 3. Geometric sketch for definition of the altitude of ambiguity h_a. Notation is explained in section 2.4.1. Assuming that h_i is the terrain elevation observed by the ith range pixel with respect to a reference ground altitude (horizontal line), we observe that the circles of equal range in the master track and the slave track cannot coincide for both the reference altitude and the altitude h_i unless the tracks themselves coincide. This effect determines whether a point located at a given range R_{mi} in the master image is located on the reference or not. The change of range is measured by the number of wavelengths, obtained by counting the number of cycles between the point and a neighbor point located at a reference altitude, and adding the residual represented by the actual value of the phase. The altitude of ambiguity h_a is the change of elevation which forces the slave range to change by half a wavelength (one-wavelength round trip) with respect to what it would be on the reference. Practically speaking, the altitude of ambiguity h_a is the elevation difference between adjacent fringes in the interferogram, after orbital correction. The fringes, as lines of equal phase in the interferogram, are like contour lines on a topographic map.

1.2.4. Contribution of the displacements. Removing the topographic and orbital contributions may reveal ground movements along the line of sight between the radar and the target (Plate 4). Any displacement of one part of the scene appears directly as a phase shift with respect to the rest of the scene. Mathematically, the radar measures scalar change $\Delta\rho$ in the satellite-to-ground distance, which equals the component of the displacement vector $\mathbf{u}$ in the direction of the radar axis

$$\Delta\rho = -\mathbf{u} \cdot \hat{\mathbf{s}} \tag{3}$$

where $\hat{\mathbf{s}}$ is the unit vector pointing from the ground point toward the satellite. A group of pixels moving by 1 cm along the radar axis between the two image acquisitions changes the round trip distance by 2 cm, or nearly 40% of a wavelength for ERS. This phase shift is easily detected. Moving along the viewing axis by half a wavelength creates one fringe, which is 28 mm for ERS. This possibility, applied to the measurement of crustal deformation, was the principal motivation for developing the technique [*Massonnet*, 1985; *Gabriel et al*., 1989].

1.2.5. Atmospheric contribution. The state of the atmosphere is not identical if the two images are acquired at different times. Any difference in the troposphere or the ionosphere between the two dates can change the apparent length of the path between the radar and the ground. We have documented examples of the effects of a heterogeneous troposphere, linked to the turbulence caused by forming storm clouds or by the interaction of high winds and relief (Plate 5). Ionospheric variations can also affect the radar propagation. Finally, even a homogeneous change in the atmosphere (pressure, humidity, and temperature) can be revealed by a contrasted relief, which modulates the thickness of the troposphere that the signal must cross. All of these effects appear as a phase change in an interferogram. Interferograms made from nighttime scenes seem to be more "coherent" (see section 1.3.1) and show fewer and smaller atmospheric artifacts than do daytime scenes. This may be due to the more quiescent state of the vegetation and the statistically more stable atmosphere at night.

1.2.6. Other contributions. Other phenomena include instrumental artifacts, such as the instability of the oscillator. In all current radar systems this frequency standard maintains a strict stability over the time of synthetic reconstruction, or about 1 s. Over longer times the frequency may drift, producing "beats" between the two phase images. This beating creates artifactual fringes perpendicular to the satellite track (Figure 4) [*Massonnet et al*., 1995b]. Improving oscillators is well within current technology and should be a priority in the design of future systems.

Changes in the reflective characteristics of the ground can also modify the phase in an interferogram (Plate 6; section 4.4) [*Gabriel et al*., 1989].

1.3. Limits of Interferometric Measurements

1.3.1. Surface preservation. The "internal" phase contribution must remain constant between the two phase images. Otherwise, it will not vanish in their difference. Extreme cases include water-covered surfaces, which have no stability. The same problem applies to tidal areas near coastlines. Agricultural fields change as soon as they are plowed or irrigated [*Wegmuller and Werner*, 1997]. Usually called "decorrelation" or "incoherence," this phenomenon destroys the organized fringe pattern in an interferogram. Each pixel undergoes a random phase change, and an area of randomly colored speckles appears in the interferogram.

The water in the Gulf of Aqaba (Plate 7) or the Gulf of Bothnia (Plate 27) appears noisy. Similarly, a small ribbon of incoherence cuts across the Landers interferogram (Plate 20a). We interpret this signature as a dry river bed where the sand shifted in the months between the acquisition of the two radar images, perhaps because water flowed in the river bed. It is, however, still possible that some stable targets, like boundary markers, ditches, or fences, remain stable in an agricultural scene and allow a partial interferometric effect over the long term, as has been observed near Kozani in Greece [*Meyer et al*., 1996].

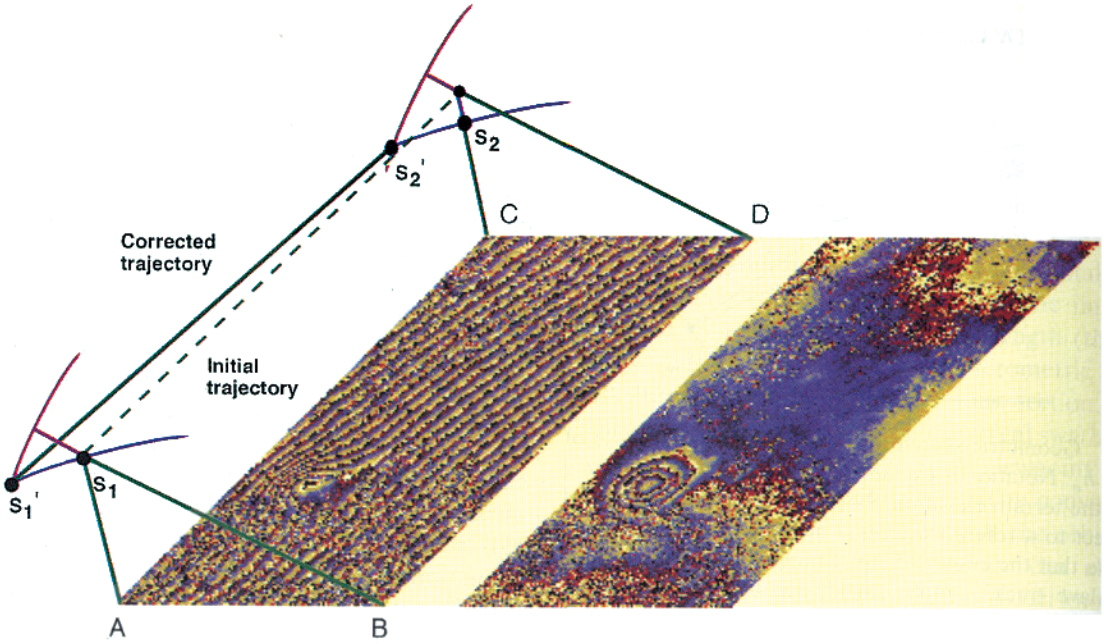

Plate 1. "Orbital" fringes representing the phase difference from the change in viewpoint between the two images. Hundreds of cycles, or fringes, may be created across an interferogram several thousand pixels wide. Most can be predicted and removed using knowledge of the satellite trajectories. However, this knowledge is not accurate to the scale of a wavelength, leaving a few tens of uncorrected fringes (left), which can in turn be used to refine the relative separation between the two trajectories. Here we count 15 fringes from point A to B, so the distance between the satellite S_1 and B should be lengthened by 15 times half the wavelength. If distance AB remains unchanged, the correct satellite position lies at the intersection of the two arcs at S'_1. Keeping A as a reference, we find that distance DS_2 should be lengthened (by 4 cycles) and distance CS_2 shortened (by 10 cycles), which puts the refined position at the end of the interferogram at S'_2. Using the refined trajectory and reprocessing the radar data suppresses orbital fringes and reveals the underlying earthquake deformation field (right), which was hardly noticeable before. This procedure may not be necessary when very accurate orbital parameters are available.

Plate 2. Topographic fringes on Mount Etna. The usual CNES processing has been altered to leave topographic fringes uncorrected while transforming the geometry to map coordinates. Here one fringe represents about 250 m of topographic elevation. The shading represents the topographic relief from the DEM, as if the illumination came from the west. The area is roughly 40 by 40 km.

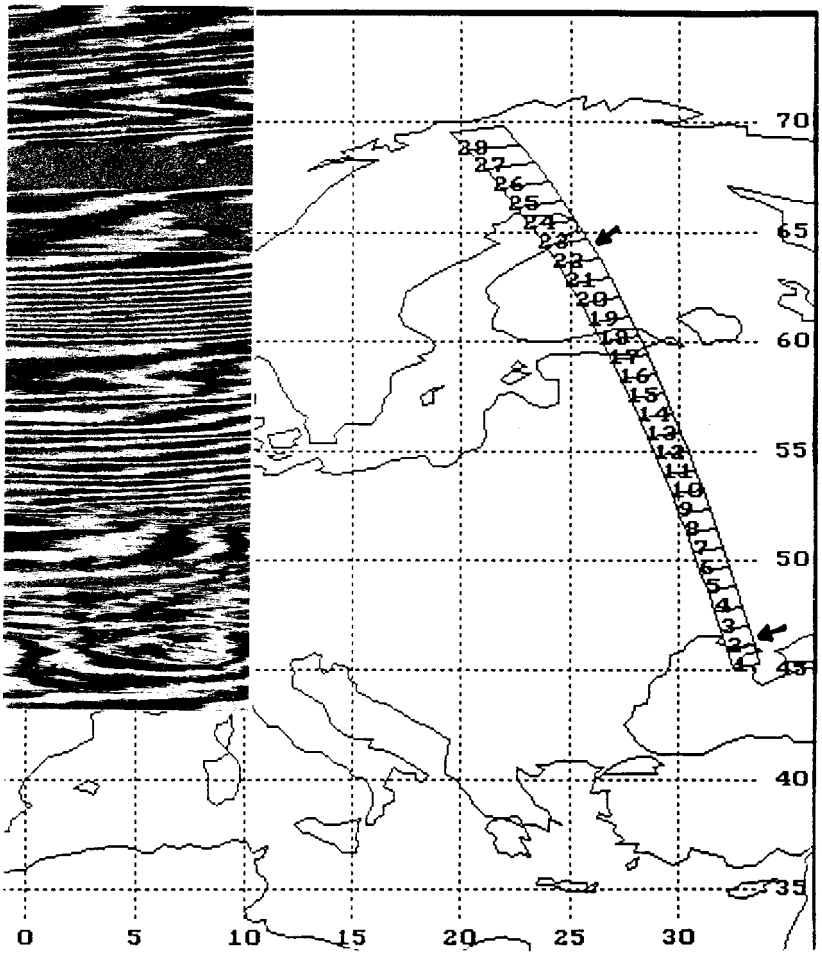

Figure 4. Apparent clock instabilities described by *Massonnet et al*. [1995b]. ERS-1 acquired the data 6 days apart (September 25 and October 1, 1991) over an area >2000 km long. The orbital separation is small: at the south end of the image the horizontal offset is 65.5 m and the vertical offset is 12.5 m; at the northern end these values are −11.5 and 8 m, respectively. The value of h_a ranges from 120 m in Crimea to −327 m in Finland. Arrows on the map delimit the radar swath. The sign change is due to the trajectories' crossing somewhere above the Gulf of Finland, where h_a becomes infinite. Also, topographic relief is moderate between southern Ukraine and northern Finland. Several groups of fringes can be observed where we expect no fringes from conventional causes or only a few fringes from the worst case atmospheric perturbation. Furthermore, these fringes are perpendicular to the satellite track. The effect is consistent with a time-dependent linear error of the carrier frequency of ERS-1 [*Massonnet et al*., 1995b].

At the other extreme lie very stable surfaces, such as rocky areas or urban areas, not counting vehicles. Arid deserts (e.g., the Atacama in Chile or Mojave in California) also conserve their phase. Snow can damage coherence temporarily (e.g., Etna summit (Plates 31b and 31i) or Iceland) or permanently. For the spectral characteristics of partial snow cover as seen by C band radar, see *Donald et al*. [1993]; for those of sea ice, see *Kwok and Cunningham* [1994]. *Guarnieri and Prati* [1997] propose a rough estimate of coherence before any interferometric processing.

1.3.2. Gradient. The necessary condition for interferometry (relation (1)) implies that the maximum detectable deformation gradient is one fringe per pixel, or the dimensionless ratio of the pixel size to the wavelength. This value depends on the satellite; it is 3×10^{-3} for ERS and 13×10^{-3} for JERS. For instance, the coseismic deformation in the Landers earthquake locally exceeded this threshold, creating incoherence (Plates 20e and 20f). For gradual movements we must choose time spans between images to remain below this threshold. Some types of deformation will thus be inaccessible if they produce strains larger than the gradient limit within a period of time shorter than the satellite's orbital cycle.

Similarly, block rotation can change the radar observation direction sufficiently to violate the necessary condition for interferometry. Such a change of direction of observation produces a set of parallel fringes oriented perpendicular to the satellite track. As for the gradient limit, where we cannot exceed one fringe of range change per range pixel, we cannot accept more than one fringe per azimuth pixel. Areas close to this limit appear in the vicinity of the Landers fault. The limit is found when a round trip range change of one wavelength is created across the azimuth pixel size. For ERS the ultimate value is 7×10^{-3} radians (28 mm divided by 4 m), or about 0.45° in the finest-resolution interferograms. If we average several adjacent pixels to form a larger pixel, these limits become more stringent, approximately 0.04° and 0.02° for spins and tilts, respectively, for an interferogram with 90-m pixels, as used at Landers. The worst case is rigid body rotation about an axis perpendicular to both the radar line of sight and the satellite velocity.

1.3.3. Ambiguity. We interpret the radar phase in terms of the round trip (two way) distance between the radar antenna and the ground. This quantity is measured only to within an additive constant corresponding to an integer number of half wavelengths (multiples of 28 mm

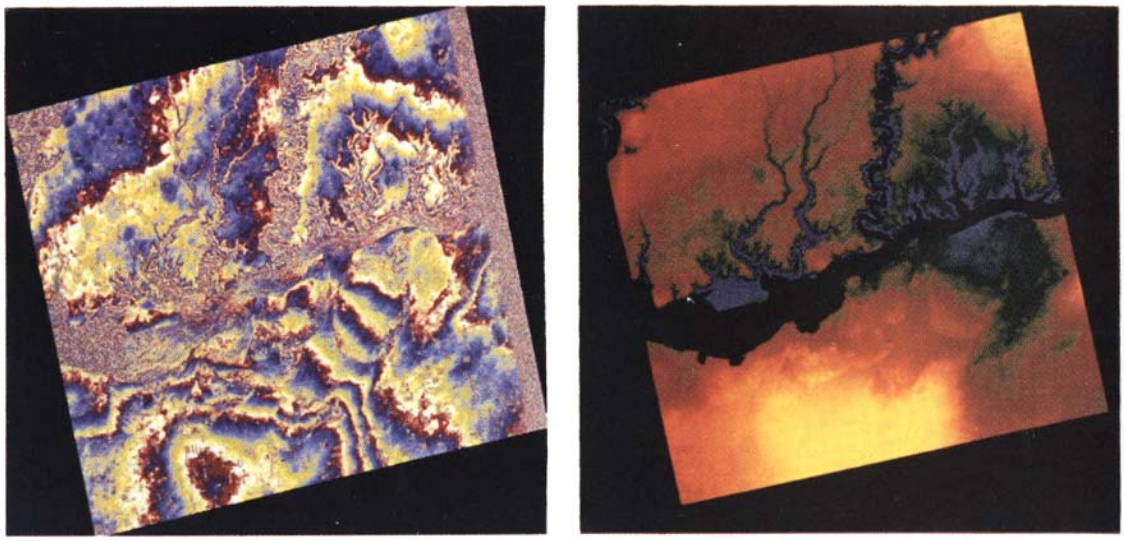

Plate 3. Example of a DEM constructed over Ukraine. ERS-1 acquired the two radar images used to form the interferogram (left) 9 days apart by ERS-1 during local night. The orbital correction uses the Dniepr River as a horizontal reference. Integer numbers were attributed to the fringes ("phase unwrapping") and multiplied by h_a to give the topographic elevation. The final product is smoothed (right). In this case the value of h_a is only 10 m and the orbital separation is slightly over 1 km, dangerously close to the theoretical limit of interferometry where the interferogram would blur, but giving the best topographic sensitivity. In some places, topographic details of $\sim$1 m are visible. This area is fairly flat with a relief of $<$60 m. Phase unwrapping was performed by ISTAR under contract to CNES.

Plate 4. Mount Etna shown in perspective with its 1-year posteruptive deformation [*Massonnet et al*., 1995a]. Up to four fringes (11 cm) of deformation can be seen, with only two on the volcano proper. This example illustrates how displacement fringes can be misinterpreted as topographic fringes or vice versa. In this case the number of fringes is not proportional to topographic elevation. Furthermore, we used a DEM calculated from optical, not radar, images and tested it against an interferogram without displacements.

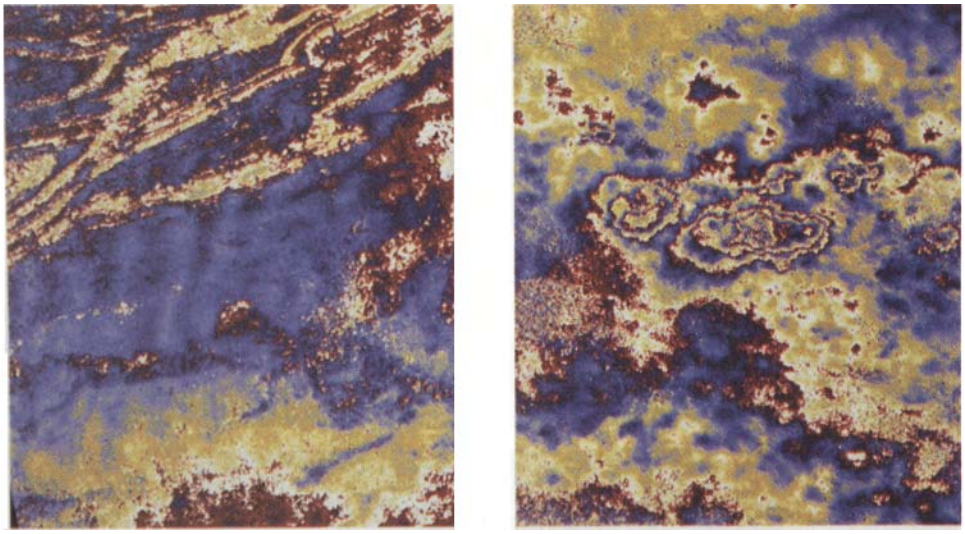

Plate 5. Two examples of contributions from the troposphere. (left) Pennsylvania weather front, consisting of (black and purple) waves traveling east-west with a wavelength of about 12 km in an interferogram made of two ERS-1 images acquired on January 12 and January 15, 1994. The wave measures only ~15% of a cycle (4 mm) from crest to trough. The most likely explanation is turbulence caused by relief associated with high winds. Owing to large h_a (>900 m), the topographic contribution is typically less than a fringe in the Blue Mountains, in the north part of the image, and was not subtracted from the interferogram. From *Tarayre and Massonnet* [1996]. (right) Landers, California, thunderstorm. The irregular circular patterns are 5–10 km wide and represent up to 3 fringes (84 mm) of atmospheric perturbation over the Mojave Desert in the August 3, 1992, image. From *Massonnet and Feigl* [1995a]. Examples of ionospheric contributions appear in Plates 12 and 31.

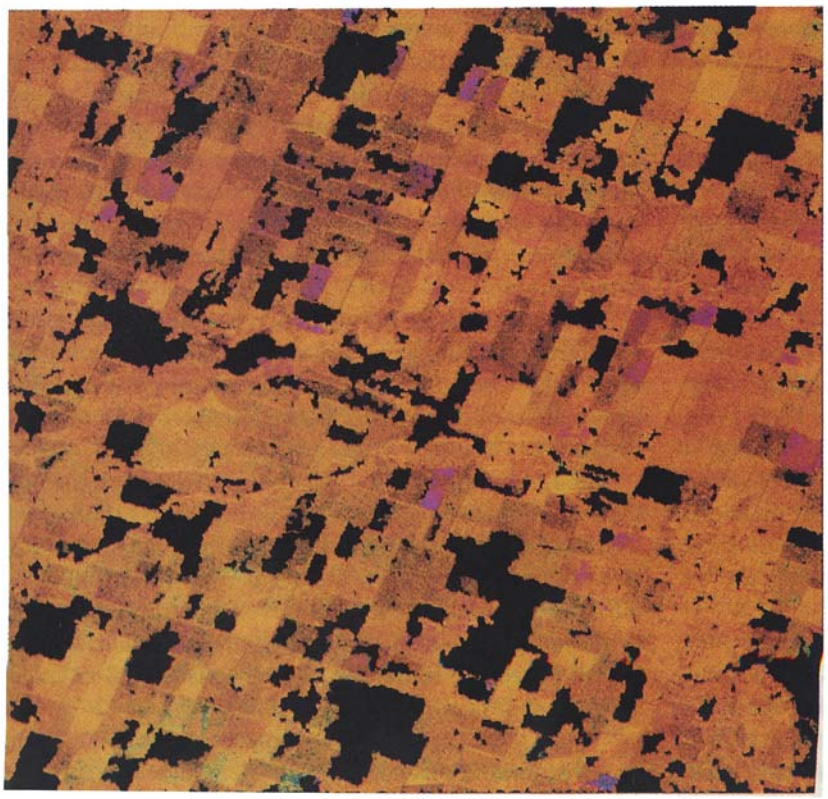

Plate 6. Interferogram of agricultural fields in the Imperial Valley, California. The interferogram uses the three-pass or "double difference" technique on 25-cm wavelength (L band) radar data acquired by Seasat on three separate dates spanning 12 days in 1978 [*Gabriel et al*., 1989]. The dominant yellow color represents zero phase change. Black areas represent the loss of phase coherence, where noisy phases of one of the interferometric pairs have been left out. The various colors, from blue to red to green, indicate small motions (2–3 cm) of the fields from changes in the soil associated with watering.

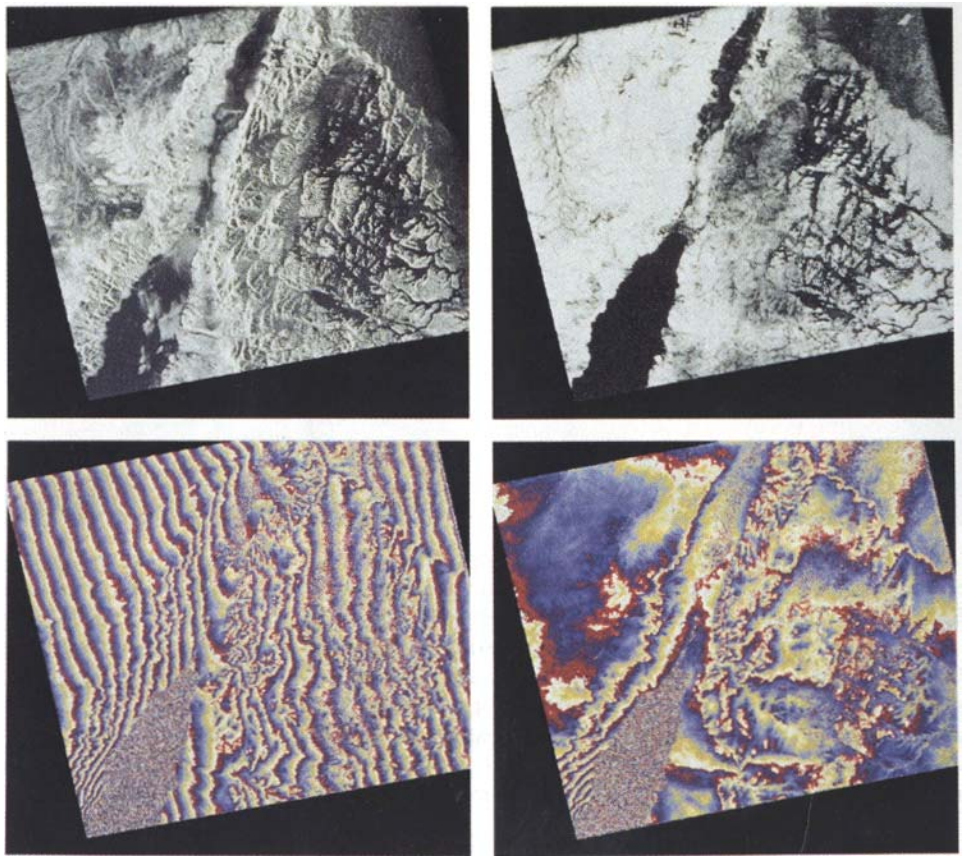

Plate 7. Example of incoherence. In a study intended to characterize the Nuweiba (November 22, 1995, M_w = 6.2) earthquake in Egypt, CNES combined two ERS-1 scenes acquired on March 23, 1995, and November 29, 1995. The brightness or amplitude image is shown at top left. The coherence map (top right) helps describe quantitatively fringe reliability. In particular, the water in the Gulf of Aqaba (dark area in SW corner) is incoherent because its surface changed between the two images. Once the raw interferogram is corrected using a priori knowledge of the orbits (bottom left), a few orbital fringes remain. Removing them leaves a mix (bottom right) of the coseismic deformation (tight fringes on the west coast of the Gulf of Aqaba) and a moderate topographic contribution governed by h_a = 480 m.

for ERS). In other words, the interferogram is intrinsically ambiguous because it gives only the fractional (noninteger) part of the phase change. To express this ambiguity, we say that an interferogram is "wrapped" (Figure 5).

It is possible to resolve this ambiguity and "unwrap" the interferogram. The simplest method is simply to count the fringes along a path, numbering each one in succession, but more sophisticated, automatic unwrapping algorithms exist (section 2.5.1). The final result should be an interferogram in which the integer part of the phase (in cycles) is correctly known at each point. Mathematically, all the pixels in a wrapped interferogram have a phase ϕ in the interval $0 \leq \phi < 1$ cycle, while the phase in an unwrapped interferogram can vary over hundreds of cycles.

The second type of ambiguity arises because interferograms record relative changes in phase, not absolute changes. In other words, we cannot identify the fringe corresponding to zero change in phase, i.e., the contour of null deformation. Mathematically, we are free to add a constant value (or "offset") to all the pixels in an interferogram. This ambiguity persists even if the interferogram has been unwrapped. Usually, we can determine this constant by assumption (e.g., null deformation at one point) or independent measurement (e.g., a GPS survey).

If we can resolve these two types of ambiguity, an interferogram changes from an ambiguous array of relative phase changes (expressed in fractions of a cycle) to a map of absolute changes in range (expressed in units of distance).

1.3.4. Other limits. Any interferogram is also intrinsically limited by the width of the swath (100 km for ERS) and by the length of time the radar operates (maximum of 12 min or 5000 km over the ground for ERS). The practical limit, however, is typically shorter, to remain on land or avoid clock artifacts. The longest image processed to date is more than 2000 km in length (Figure 4) [*Massonnet et al.*, 1995b].

The size of the pixel also imposes its own limit. The interferometric measurement is meaningless on a single

pixel because it can include noise in an unpredictable way. Successful interpretation thus depends on the structure of the image and the agreement of several neighboring pixels. A geophysical phenomenon is difficult or impossible to recognize unless it is at least 10 pixels wide. The corresponding width ranges from 200 m to 1000 m, depending on the complex averaging necessary to achieve a good ratio of signal to noise.

Assessing the displacement requires counting the fringes, so the interferogram must be continuous in space. This requirement has a few exceptions: crossing an (incoherent) river in an area with a low gradient may not cast doubt on the fringe count (Plate 3). Similarly, the offset across surface-rupturing faults can be measured by counting fringes on a path that goes around the end of the discontinuity in the fringe pattern.

Rough topographic relief in mountainous areas can limit the usefulness of an interferogram by producing incoherence there, as observed at Landers (Plate 20). The same phenomenon occurs at Northridge, where its effect appears to depend on the satellite used, ERS-1 or JERS-1 (Plate 19). The ERS-1 interferogram loses coherence in the mountains to the north of the epicenter while the JERS-1 fringes remain visible, but somewhat unclear, in this area. Both interferograms are equally sensitive to topography ($h_a \approx 50$ m) and equally far from the threshold value for successful interferometry over flat terrain. But the local slopes may push the ERS-1 data at 23° incidence beyond the interferometric limit much more easily than the J-ERS data at 35°.

1.3.5. Platform limitations. Interferometry is conceptually possible with radar sensors on board platforms other than satellites; however, the difficulty of repeating the trajectory to meet interferometric conditions and the difficulty of determining the trajectory to eliminate "orbital" contribution will require improvements in the navigation systems of airplanes or helicopters. A relatively inexpensive solution would be to carry a radar on a truck, which could monitor landslides, especially those that threaten roads, with a very flexible cadence.

A lot of interferometry has been done from airplanes, but with two antennae mounted on the same aircraft to measure static topography. These systems extend beyond the scope of this article [see *Graham*, 1974; *Curlander*, 1995; *Madsen et al*., 1995, 1996; *Orwig et al*., 1995; *Alberti and Ponte*, 1996]. The same principle drives the Shuttle Radar Topography Mission (*SRTM*), an 11-day mission of the space shuttle planned for 2000 intended to provide Earth's topography within ±60° of latitude, with a typical accuracy of 10 m, using a dual-antenna concept that reuses the SIR-C hardware. Although not capable of detecting displacements, this mission could offer a substantial improvement in interferometric technique, if the resulting DEM is made public, by allowing an easy and safe removal of the topographic contribution.

Several groups have attempted to monitor displacements by two-pass interferometry on airplanes as experimental test beds [*Massonnet*, 1990; *Gray and Farris-Manning*, 1993; *Stevens et al*., 1995]. Again, the technical difficulty is to fly along two paths that are not too different and then to eliminate the contribution due to the shifting trajectories. In addition, the lack of a tape recorder on board the ERS-1, ERS-2, and JERS satellites limits data acquisitions to study areas within 3400 km of a "download," or receiving, station (Figure 6).

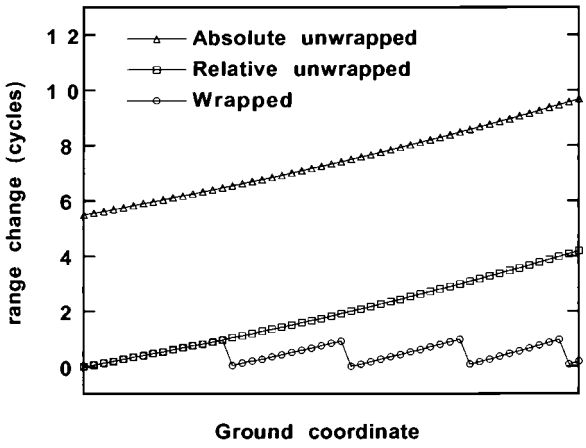

Figure 5. Cartoon showing profiles of range change for three types of phase measurements: absolute unwrapped (triangles), relative unwrapped (squares), and wrapped (circles). Absolute and relative unwrapped signals differ by a constant offset. The wrapped signal is the relative signal modulo 2π (1 cycle). The slopes of all three curves (range gradient) are identical at any given point, except at the discontinuities. Considering, for example, two distinct red areas in an interferogram, we know only that their phase values are the same up to an integer number of cycles. If the color red denotes a phase change of, say, 0.1 cycles, we do not know if one red spot has a value of 0.1 cycles and the other spot has a value of 1.1 cycles or if the values are 0.1 and 2.1 cycles, respectively. To resolve this ambiguity, we must visually count the number of fringes between the two spots. If only one fringe separates the two spots, then their phase difference is $1.1 - 0.1 = 1.0$ cycle. Such an ambiguous interferogram is "wrapped."

1.3.6. Cycle-slicing limit. At what point does cutting the phase into smaller pieces become meaningless? This "cycle-slicing limit" is not due to numerical discretization because the number of bits coding each raw data pixel is shuffled in SAR processing. The signal in each pixel is (1) the coherent addition of the elementary targets, which remain stable and in the same relative position within the pixel, and (2) the incoherent addition of the discretization noise, the thermal noise (generated by the radar instrument), targets present in one radar image but not the other (such as vehicles), and targets changing with time. The final measurement is the complex sum of the coherent vector (the ideal measurement) and the incoherent vector (the phase of which can point anywhere). The higher the ratio of their magnitude, the more accurate the measurement becomes. This is why summing on N neighboring pixels (as explained in sec-

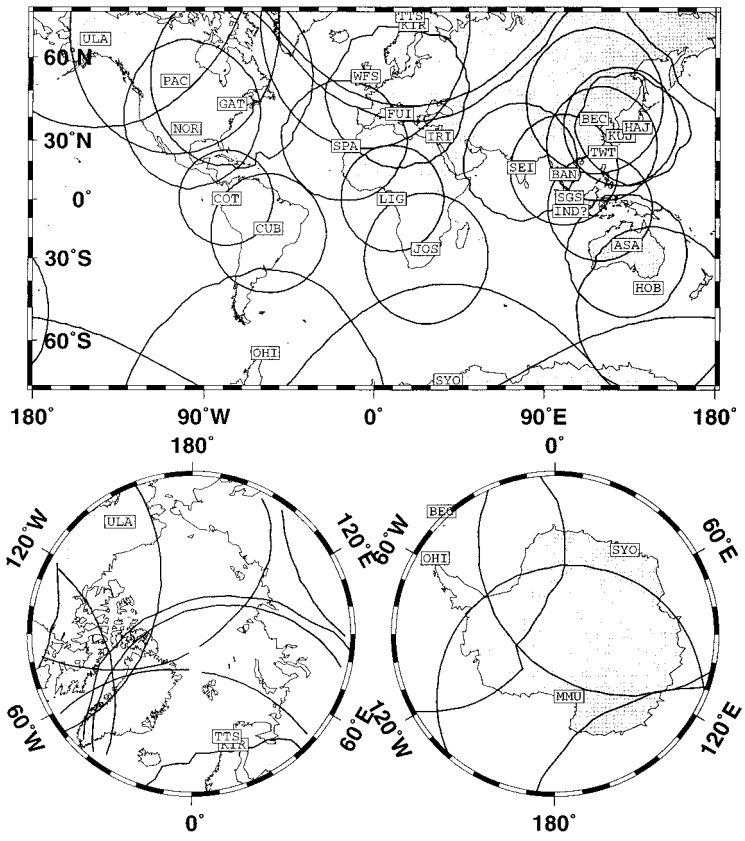

Figure 6. ERS download stations with visibility circles and dates of operation. In practice, only scenes within a 3400-km-radius circle of visibility around a ground station reach the archives. For example, geophysically interesting regions in central Asia and South America fall outside the areas covered early by ERS, particularly in 1992 and 1993. Nor does ERS cover the active volcanoes of Hawaii or La Réunion. Circles of visibility are approximate as given by the European Space Agency (ESA) display ERS SAR coverage (DESC) catalogue (available from ESA; ftp://earthnet.esrin.esa.it:FTP/software/descw) for all stations except IRI, SAU, and IND, where we trace a small circle of radius 3400 km. The actual radius of visibility may vary as function of obstacles at the download antenna. Station codes are ULA, Fairbanks, Alaska; ASA, Alice Springs, Australia; BEC, Beijing, China; COT, Cotopaxi, Ecuador; CUB, Cuiabá, Brazil; FUI, Fucino, Italy; GAT, Gatineau, Canada; HAJ, Hatoyama, Japan; HOB, Hobart, Australia; IND, Pari-Pari, Indonesia; IRI, Tel Aviv, Israel; JOS, Johannesburg, South Africa; KIR, Kiruna, Sweden; KUJ, Kumamoto, Japan; LIG, Libreville, Gabon; MMU, McMurdo, Antarctica (U.S.A.); SPA, Maspalomas, Canary Islands, Spain; NOR, Norman, Oklahoma, USA; PAC, Prince Albert, Saskatchewan, Canada; SEI, Hyderabad, India; SGS, Singapore; SYO, Syowa, Antarctica (Japan); OHI, O'Higgins, Antarctica (Germany); BAN, Bangkok, Thailand; TTS, Tromsø, Norway; TWT, Taiwan; WFS, West Freugh, United Kingdom. Two temporary stations are not shown: SAU, Riyadh, Saudi Arabia, and TOL, Toulouse, France.

tion 2.5.3) improves the accuracy. The coherent part grows as N, and the incoherent part as the square root of N. The visual appearance of interferometric fringes is highly nonlinear with the ratio of coherent to incoherent parts. Above 1, the fringes remain visually readable but disappear quickly as the phase of the incoherent part takes over.

It is difficult to give firm figures for the cycle-slicing limit because targets can vary between fully coherent and incoherent. In two-pass interferometry with ERS, we have observed a typical noise level of one sixtieth of a fringe with natural targets, after complex summation of 10 neighboring pixels and resulting 40-m-square pixels. This corresponds to about half a millimeter in range.

Measuring this limit would require a calibration site with no geophysical signal. In hundreds of scenes we have never seen such a site, probably because of the atmospheric contribution. However, because the atmosphere changes only smoothly over a scene, we can make a local estimate of accuracy from the local noise (such as the one sixtieth of a fringe mentioned above) on the interferogram or the statistics of a residual interferogram, after removing a local geophysical model (section 3.3). At first glance, using a satellite with a longer wavelength, for instance L band instead of C band, should degrade the geometric performances by a factor of 4. In contrast, the improvement could reach almost 2 if we substitute the shorter-wavelength X band for C band. However, these first-order estimations disregard other factors, such as a higher coherence expected with L band data in areas covered with dense vegetation. Such factors could partially compensate the intrinsically lower accuracy of longer wavelengths by allowing cutting cycles into smaller "slices."

2. CONSTRUCTING AND IMPROVING INTERFEROGRAMS

In contrast to the preceding section, this discussion provides technical and mathematical details. The uninterested reader may skip to section 3. For a mathematical presentation, see also the review by *Bamler and Hartl* [1998].

2.1. Where to Start?

Interferometric processing can start with complex, high-resolution images (called "single look complex," or *SLC*) or with raw data. The only drawback to starting from raw data is the processing time required. The parameters for focusing radar data are obtained from the permanent instrumental characteristics (e.g., wave-

length, sampling rate), from orbital data using auxiliary tools (e.g., "Doppler rate"), or from samples of the raw data (e.g., "Doppler centroid").

For proper interferometric combination, elementary targets must be weighted the same way in both images, which happens automatically if they are focused identically. For example, they must share the same Doppler centroid, which should be set to the average of the optimal value for each image, rather than the optimal value for each scene individually. Worse yet are SLC scenes from different processing centers, which may operate slightly different algorithms. Constructing complex radar images from raw data eliminates such problems by ensuring consistent focusing.

Another practical advantage of "do-it-yourself" focusing is the ability to handle long segments as single data streams. It is much more convenient to concatenate files of raw data than to paste images together, because of "dropouts" during the image formation and discontinuities created by changing parameters. Furthermore, raw data are generally less expensive than focused images. They also may be less bulky if only selected frequency bands are processed [*Massonnet et al*., 1994b].

2.2. How to Coregister the Images

Weighting elementary targets equally in both image requires coregistering them to within a small fraction of a pixel [*Massonnet*, 1993; *Just and Bamler*, 1994]. This operation requires large corrections, caused by different starting times of the images, different nearest distance of observation, and overall difference in viewpoint between the two images. Stereoscopic distortions are generally much smaller than the size of a pixel because of the orbital restriction for a successful interferogram. Three steps are required for proper coregistration:

1. The geometric differences between the two radar images must be evaluated. *Gabriel and Goldstein* [1988] superpose image patches in the complex domain. *Lin et al*. [1992] select the superposition that minimizes the phase variations between the images. Conventional correlation of amplitude image patches seems to be the best choice because its accuracy approaches 0.03 pixels [*Li and Goldstein*, 1990; *Massonnet*, 1994; *Kwoh et al*., 1994].

2. The geometric differences must be modeled. Several groups use a least squares adjustment to approximate the distortion with a low-order polynomial, but this neglects the residual stereoscopic effect. We calculate the theoretical distortion grid between the two images from the topographic and orbital data and compare it with the observations. The comparison yields only two constants, the start of acquisition time and the nearest distance, with the accuracy required to improve the model. The method is very robust and yields the same accuracy at all points of the radar image, even in places where the correlation fails locally.

3. One of the images (which we call the slave image) has to be made superposable to the other, while respecting the phase content. Some teams use bilinear [*Lin et al*., 1992] or bicubic [*Kwoh et al*., 1994] resampling. We resample the image in the complex domain by small blocks of a few pixels (typically 50 or fewer) according to the model grid. Each block is translated in azimuth and range by a fraction of a pixel using multiplication by phase ramps in the frequency domain.

2.3. How to Form the Interferogram

We assume that M is the current complex pixel with row and column coordinates in the master image, arbitrarily chosen as a geometric reference, and that S is the corresponding pixel in the coregistered slave image, i.e., the complex slave image mapped into the master image geometry. The phase difference at this point is the phase of MS^*, where the asterisk denotes complex conjugation. We can average over neighboring pixels to improve the signal-to-noise ratio, in a process called "complex multilooking." An additional advantage of this filtering step is to obtain a square shape for the final pixel, or "cell." For a typical pixel size of 4 m along the track and 20 m across, 2 looks in range and 10 looks in azimuth, for a total of 20 looks, is a reasonable choice.

Prior to complex summation, the Centre National d'Etudes Spatiales (*CNES*) procedure eliminates the predicted phase differences due to orbits and topography, which are summarized by the function G, expressed in units of wavelength in the same image coordinates. By removing the bulk of the phases, G allows a "safe" complex summation, without blurring because the remaining phase change gradient is low. It is caused by only the signal unknown prior to the interferometric measurement, whether caused by displacements or uncorrected topography. The general terms of the averaged amplitude image **A**, and the interferogram **I** are

$$A = \frac{\sqrt{\sum (\mathbf{M}^2 + \mathbf{S}^2)}}{\sqrt{2N}} \tag{4}$$

$$I = \frac{\sum f(\mathbf{M})\, f(\mathbf{S}^*)\, \exp(2\pi i \mathbf{G})}{\sqrt{\sum f(\mathbf{M})^2}\ \sqrt{\sum f(\mathbf{S})^2}} \tag{5}$$

where N is the number of points in the cells on which the summation applies. The terms **M**, **S**, **A**, **I**, and **G** are implicit functions of the image point coordinates. The filter f applied to both M and S images is described in the next paragraph. The phase of (5) is the interferogram per se. To code it as bytes, we multiply the phases by $256/(2\pi)$ to take advantage of the full digital range. The magnitude of (5) ranges from 0 to 1 and is called *coherence*. It measures the reliability of the measurement. A perfect coherence of 1 would mean that every pixel agreed with the phase within its cell, a very unlikely situation if the cell contains more than one pixel. A value close to zero indicates a meaningless phase measurement. Calculated this way, the coherence corresponds to the intrinsic coherence of the ground, a physical property. Although quantitative, the coherence depends on the number of pixels averaged in a cell.

The CNES procedure applies a filter f to up to five points in range, as indicated in (5). Although its derivation is beyond the scope of this paper, the filter f is designed to further reduce the difference in radar impulse response perceived by each satellite track from the same piece of ground. The radar group at Politecnico Milano advocates filtering in the frequency domain using a theory of "ground frequency shift" [*Prati et al.*, 1991; *Prati and Rocca*, 1993; *Gatelli et al.*, 1994]. The CNES filter improves the interferogram in areas of high relief with rapidly varying slopes. By working in a cartographic reference system, this approach can distinguish between two distinct areas of the landscape located at the same distance and azimuth to the radar, easing problems with the "layover."

2.4. Processing Algorithms

2.4.1. Geometric description. In this section we index master and slave images as m and s, respectively. If there is a third, complementary image, we use the index c. The letter i indexes the pixel (by distance) for the master image. According to the notation of Figure 3, where the trajectories are perpendicular to the drawing, we have from a straightforward development

$$\sin(g_i) = \frac{R_{si}^2 - \delta^2 - R_{mi}^2}{2\delta R_{mi}} \tag{6}$$

We express all lengths as multiples of the pixel size; $\Delta = \lambda Q/2$, where Q represents the number of half wavelengths per slant range pixel and has the value 279.4 in the case of ERS. The term λ is the radar wavelength, and δ is the distance between satellite tracks. Letting R_0 be the distance corresponding to the first column of the master image, we may then write

$$R_{mi} = R_0 + i\Delta \tag{7}$$

$$R_{si} = R_0 + i\Delta + p\Delta + n_i/Q \tag{8}$$

where i is set for the pixel number in the master scene; p is the difference in distance between the slave image and the master image at near range; and n_i is the number of cycles, or fringes, counted in the interferogram at pixel i, so that n_i/Q is the number of associated pixels. Thus n and g are functions of i, but p is not. Therefore, from (8),

$$\sin(g_i) = \frac{p\Delta + \lambda n_i/2}{\delta} + \frac{(p\Delta + \lambda n_i/2)^2}{2\delta(R_0 + i\Delta)} - \frac{\delta}{2(R_0 + i\Delta)} \tag{9}$$

In (9) the first term is dominant (generally close to 1), while the others are of the order of 10^{-4} to 10^{-5}. The n_i fringes counted at point i determine the elevation h_i [*Massonnet and Rabaute*, 1993]. Define the altitude of ambiguity h_a as the difference in altitude that generates one fringe; therefore

$$h_a = dh_i/dn \tag{10}$$

$$\frac{dh_i}{dn} = R_m \frac{dg_i}{dn} \sin(g_i - \theta) = R_m \frac{d(\sin(g_i))}{dn} \frac{\sin(g_i - \theta)}{\cos(g_i)} \tag{11}$$

This derivative can be written as the finite difference $\Delta h/\Delta n$ and therefore gives the altitude of ambiguity, if the number of fringes changes by 1:

$$\frac{d(\sin(g_i))}{dn} \approx \frac{\lambda}{2\delta} \tag{12}$$

which leads to the approximate expression, close to (2)

$$h_a \approx \frac{\lambda}{2} \frac{R_0 + i\Delta + p\Delta + \lambda n_i/2}{\delta} \cdot (\tan(g_i)\cos(\theta) - \sin(\theta)) \tag{13}$$

Supposing that the value of g_i is known, we can infer n_i from (9):

$$n_i/Q = \sqrt{(R_0 + i\Delta)^2 + \delta^2 + 2\delta(R_0 + i\Delta)\sin(g_i)} - (R_0 + i\Delta + p\Delta) \tag{14}$$

2.4.2. Two-pass interferometry. Two radar images suffice to calculate an interferogram. Called *two-pass interferometry*, this approach seeks to exploit all the external information available for a site, in particular, the topography through a digital elevation model. This philosophy comes into play at five key steps of the CNES processing:

1. The two radar images must be coregistered with a precision of a fraction of a pixel as described in section 2.2. The DEM and the orbits predict a deformation grid, which is compared with a sparse grid obtained from local correlations on actual images. The comparison of the two grids uses the observed radar data to improve the predicted distortion grid, which becomes accurate down to a few hundredths of a pixel, both locally and globally.
2. One of the radar images must be registered in absolute geographic coordinates. We simulate a radar image whose amplitude depends on the local topographic slope, which is then correlated with the observed image. The resulting precision is about half the size of a DEM pixel. It deteriorates in very flat terrain, where registration becomes less important.
3. We apply a filter based on the local topographic slope during the interferometric fusion of the two images. This filter improves the results, especially for the cases of steep relief (section 2.3).
4. We eliminate the topographic contribution by subtracting the fringe pattern calculated from the DEM. The advantage of this approach is that it removes many unwanted fringes, leaving only those related to the signal of interest and/or errors in the DEM (Plate 8).

5. We project the interferogram into an orthogonal cartographic or geographic coordinate system, so that users need not work in the distorted radar geometry.

The software developed according to these principles runs automatically in most cases, starting from the raw radar data and the DEM, and leading to a set of fringes free of orbital and topographic effects in a cartographic reference frame. The two other products described in section 2.3, amplitude and coherence, use the same geometry as the interferogram.

The final piece of information is the unit vector $\hat{\mathbf{s}}$, the projection of the mean viewing vector in local (east, north, up) coordinates. It provides the geometric sensitivity to ground displacements as described in section 1.2.4. Compared with most analytic radar data products, the interferometric product is remarkably simple because it is intrinsically expressed in units of length.

2.4.3. Three-pass interferometry. The method used by other research groups, Jet Propulsion Laboratory (*JPL*) in particular, is based on three radar images, as described by *Gabriel et al*. [1989] and *Zebker et al*. [1994a], and is called *three-pass interferometry*. This method has the advantage of not requiring any information other than the radar data. The formula (14) predicts the topographic fringe pattern of one interferogram from a second one, if the second is due only to relief. Using three images, we construct two interferograms with the same master. We index the two interferograms s or c for slave and complementary, respectively. First, we calculate $g_s(i)$ from p_s, $n_s(i)$ and δ_s, which are the values for the first interferogram (master minus slave). Next, we define the look angle $g_s(i) - \theta_s$, which is equal to $g_c(i) - \theta_c$ because the master ray is common to the two interferograms. In practice, only the difference $\theta_c - \theta_s$ is needed for this operation. Finally, we recalculate $\sin(g_c)$ by means of δ_c and p_c to calculate $n_c(i)/Q$ by (14), from which $n_c(i)$ follows.

We may subtract these calculated fringes from the second interferogram, eliminating topographic effects. This geometric procedure is very pleasing because only radar data are required. However, the method has several drawbacks, which limit its practical usefulness:

1. The quantity $n_s(i)$ must be the absolute number of fringes, meaning that the first interferogram must be unwrapped. Unwrapping is not an easy task and may lead to errors, particularly where the fringes become dense or incoherent (section 2.5.1). Any such errors are then recycled as incorrect topographic information in the final interferogram and are not easy to recognize, since they are no longer multiples of half the wavelength. To avoid misinterpreting such results, it seems advisable to mask difficult areas in the final interferogram.

2. The three-pass method assumes that the complementary image pair used to estimate the topography includes no deformation. This reasoning may not apply to gradual (temporally secular) movements. Moreover, an interferogram always contains contributions linked to the atmosphere. Manipulating these contributions with equations for the topography may lead to an inextricable mixture. The importance of the atmospheric contribution was not recognized when this method was proposed.

3. Since the three-pass method includes no knowledge of the topographic slopes, it cannot apply a pulse response filter during the interferometric fusion, diminishing the quality of the interferogram. For reliability, it seems advantageous to use the DEM as an intermediate step because it has physical meaning. This means that improvements may be made and corrections included. If only three images were available, we would first calculate a DEM with one radar pair. In this sense, the three-pass method is the worst case of the two-pass method.

4. The probability of finding three mutually coherent images is smaller than that of finding two such images. It is also smaller than the probability of finding two independent coherent pairs. In particular, if only radar data are available, the DEM can be calculated from a pair of images in another orbital track, or even another satellite. In contrast, the three-pass approach requires that all three images be acquired by the same satellite in the same orbital track. Conversely, a DEM on a given site can improve interferograms from image pairs from any satellite or orbital configuration.

2.4.4. Software packages. The various software packages have arisen from different conceptions of differential interferometry. Each team emphasized certain aspects of the problem and selected specific solutions. Now that the technical developments have reached a plateau, the geophysical user should learn how to take advantage of all of them as they become available. For example, one could compute an interferogram with the CNES *DIAPASON* software and unwrap the result with the POLIMI tools. Or one could build a DEM using the JPL package and one pair of radar images and then inject the result into the CNES software to eliminate the topographic contribution in another pair, possibly from another satellite. Such hybrid solutions are likely to become commonplace in the next few years [*Vincent and Rundle*, 1998]. Fortunately, they are unlikely to produce incorrect measurements because most mistakes in processing will destroy the fringes. More generally, it is difficult to bias the result, whatever processing or filtering is used.

In any case, the scientific user needs to understand and control three essential points:

2.4.4.1. Selecting the images: Selecting radar images to successfully calculate a useful interferogram involves a number of criteria, including the availability of images, their date, and orbits. For example, events occurring at a specific time require an image both before and after the event. The choice of scenes also calls for some knowledge of local conditions in the study area. Similarly, seasonal effects can influence the choice of dates. We avoid acquiring scenes when there is snow on the ground. If deciduous trees are present, it is preferable to use scenes acquired at the same time of year.

Early spring and late autumn are good choices because of the (usual) absence of both leaves on the trees and snow on the ground. For regions with thick vegetation, coherence falls off rapidly with increasing time between scenes, particularly at shorter radar wavelengths.

The choice of radar images depends crucially on the relative positions of the orbital trajectories and, of course, on the scenes available. As the number of possible interferometric pairs becomes large quickly when several scenes are available for the same site, CNES has developed software to help select useful pairs by considering computed orbits and catalogues of existing scenes. In practice, only the European Space Agency (*ESA*) has made such information public, and the selection program ORBISCAN currently only handles data from ERS-1 and ERS-2. The program calculates which orbital tracks can see a given site, determines if radar images are available there, and computes the altitude of ambiguity h_a for each potential pair. The final list of image pairs can be conditioned by logical criteria. Among these, one can exclude pairs with h_a lower than a specified value, pairs that do not span a specified date, etc.

2.4.4.2. Creating the interferogram: Ideally, the DIAPASON software runs automatically. The future will tell if it is sufficiently robust to handle all cases without intervention. The processing consists of installing the useful images and data on a disk or magnetic tape, providing the space needed for storing the intermediate and final images, preparing a control file with all the required parameters, running the software, and checking the results. For simplicity the user sets up a control file by copying and modifying a template with the file names and parameter values.

2.4.4.3. Interpreting the results: The various discrimination techniques are explained in section 3. This skill can be acquired in a few days or, we hope, by reading section 4.

2.5. Auxiliary Algorithms and Tricks

Interferograms are a new kind of image and, as such, require a number of specific algorithmic tools to filter and display the results. We list these here, as well as the tricks used routinely at CNES.

2.5.1. Phase-unwrapping algorithms. An interferogram is intrinsically ambiguous because the phase is defined modulo 2π, as is described in section 1.3.3. Resolving this ambiguity is called "unwrapping" the phase. The problem is not specific to radar interferometry and can be found in optics as well as in nuclear magnetic resonance imagery. Since we have no prior information on the integer part of the phase, we can use only the hypothesis of continuity to reconstruct it from place to place. The absolute phase difference between two points in the image is the integral sum along any path and should be independent of the path followed.

The most straightforward procedure is step-by-step unwrapping. Its most naive implementation integrates the phase between two successive pixels, assuming that the difference is less than π. In this assumption, errors propagate through the whole interferogram and yield different results depending on the path followed. Several solutions have been proposed to avoid integrating errors [*Ghiglia et al*., 1987], such as detecting residuals where the integral along a closed path is not zero and avoiding them [*Goldstein et al*., 1988]. Such residues may be found along crests where the phase pattern is discontinuous ("ghost lines") [*Prati et al*., 1990]. Local optimization techniques fit a surface to several neighboring phase values while introducing some constraints. Fringes can also be detected as contours, for instance by aggregation of points not separated by a transition [*Lin et al*., 1992].

One can identify suspicious areas in the interferogram with the conventional amplitude image or the coherence image, to minimize the area where problems may arise. Very dark surfaces will be considered as lakes, bright crests are suspected of creating ghost lines, etc. Phase unwrapping is a very active field, as measured by the number of recent publications [*Ghiglia et al*., 1987; *Goldstein et al*., 1988; *Ghiglia and Romero*, 1994; *Griffiths and Wilkinson*, 1994; *Lin et al*., 1994; *Pandit et al*., 1994; *Tarayre*, 1994; *Zebker et al*., 1994b; *Marroquin and Rivera*, 1995; *Song et al*., 1995; *Fornaro et al*., 1996; *Pritt*, 1996; *Ghiglia and Pritt*, 1998].

Despite its popularity, phase unwrapping is a burden and cannot be performed in a totally automatic way. Furthermore, it can lead to errors that can be misinterpreted as displacements. For these reasons, any way to reduce the need for phase unwrapping is welcome. Using any kind of topographic information or any a priori modeling of geophysical event is a step in this direction. The trick is that any likely model, once subtracted from the interferogram, will decrease the integer rank of the fringes in the interferogram or even, ideally, bring all the fringes to the same rank. This can happen if the DEM accuracy ε is better than h_a and the geophysical displacement model is accurate to one fringe.

2.5.2. Fine orbital tuning. To eliminate the residual orbital contribution in an interferogram, we count the residual fringes on the interferogram and attribute them to an error in the slave orbit (Plate 1). This approximation is acceptable because the phenomenon depends mainly on the relative, rather than absolute, positions of the orbits. We seek two corrections to the slave orbit, a vertical and a lateral deviation, both of which change linearly with time along track as $a + bt$ and $c + dt$. To determine the four coefficients a, b, c, and d, we choose four points as far apart as possible in the final image, typically at the corners. We then count the residual fringes between them. The four coefficients are the solution of a linear system of four equations involving the positions of the four points and the number of cycles at each of them. The orbit can then be corrected for any epoch in time, and the interferogram can be adequately corrected everywhere. Usually, we apply the correction to the final product, because the error

committed on the slave orbit is too small to alter the previous processing steps. If necessary, we could completely reiterate the processing with the corrected slave orbit, but a single correction is sufficient in practice.

In a slightly different approach, *Murakami et al*. [1996] use GPS measurements of surface displacement at seven bench marks within about 15 km of the Northridge earthquake epicenter to adjust the orbital parameters. They obtain residual differences (GPS minus JERS-1 radar) of less than 3 cm in range, smaller than the 3.5-cm uncertainty of the GPS measurements. More widely separated control points (e.g., the four corners of the ~100 by 100 km image) provide a better estimate of the orbital separation, which varies mostly over long wavelengths [*Massonnet et al*., 1996a].

2.5.3. Complex multilooking. To reduce the noise level in an interferogram, one thinks immediately of averaging neighboring pixels. However, since each pixel is generally coded as a single byte, a discontinuity occurs between 255 and 0, due to the cyclic (wrapped) nature of the phase. To average properly, we first transform each byte into the phase of a complex number. The modulus of this complex number can be uniformly chosen as 1 or determined from the corresponding amplitude image. We then apply a procedure similar to the one described in section 2.3.

2.5.4. Integer interferogram combination. It is possible to "stack" several interferograms of the same site to increase their clarity or reduce the number of fringes, thus creating an integer interferogram combination (*IIC*). The trick is that the combined interferogram can have a better altitude of ambiguity h_a than any of the source interferograms. The derivation is straightforward for the case of integer coefficients [*Massonnet et al*., 1996c] or phase gradients [*Sandwell and Price*, 1998]. After correction for topographic and orbital contributions, the interferogram contains three kinds of information: (1) the number of fringes ν representing noise, due to thermal noise or to partial incoherence; (2) The number of fringes ε/h_a due to the errors ε in the DEM, where h_a is the altitude of ambiguity (there is no need to distinguish an absolute vertical error of the DEM pixel from a horizontal error in its position, since all the radar images on a given site are coregistered with a sub-pixel accuracy); and (3) the number of fringes μ caused by any differential effects, including local variations in the atmospheric thickness, as well as local ground motion between the acquisition times.

All three quantities (ν, ε, and μ) vary greatly across the image. In contrast, h_a is stable and generally varies gently with range and azimuth. This is not the case when the orbital trajectories cross. However, in this case, h_a is very high and does not need to be increased further. The interferogram where the topographic and orbital fringes have been subtracted gives us the fractional part of

$$\nu + \mu + \varepsilon/h_a$$

It cannot be mathematically manipulated unless it has been unwrapped. However, we can manipulate the interferogram while preserving its integer and fractional parts. If we multiply the interferogram by an integer q_1, we will likewise multiply the number of phase transitions and the initial integer values. Note that the integer values remain unknown unless unwrapping has been performed. We obtain the fractional part of

$$q_1\nu + q_1\mu + q_1\varepsilon/h_a$$

If we combine the first interferogram with a second, which we multiply by q_2, that contains an independent noise, another altitude of ambiguity, and other differential effects but the same local DEM error ε, we obtain the fractional part of

$$(q_1\nu_1 + q_2\nu_2) + (q_1\mu_1 + q_2\mu_2) + \varepsilon\left(\frac{q_1}{h_{a1}} + \frac{q_2}{h_{a2}}\right)$$

where the subscripts 1 and 2 refer to the first and second interferograms, respectively.

The rms amplitude of the noise becomes

$$\sqrt{q_1^2\nu_1^2 + q_2^2\nu_2^2}$$

which always represents an increase, practically limiting the absolute value of q_1 or q_2 to less than 3. Otherwise, the noise distribution could easily exceed one cycle, and the result would be useless. Noise is usually responsible for a phase uncertainty of only a few percent of a cycle, but atmospheric artifacts are also multiplied by q_1 and q_2.

The interferogram resulting from this kind of combination exhibits an equivalent altitude of ambiguity, h_{ae}, written as

$$\frac{1}{h_{ae}} = \frac{q_1}{h_{a1}} + \frac{q_2}{h_{a2}} \tag{15}$$

Phase unwrapping applies to altitudes of ambiguity lower than 100–200 m (the accuracy of the worst available DEM), and greater than 10 m in interferometric conditions [*Massonnet and Rabaute*, 1993]. Even choosing q_1 and q_2 to be ± 1, ± 2, or ± 3 allows us to reach an equivalent altitude of ambiguity of more than 100 m most of the time [*Massonnet et al*., 1996c]. Using this method, we create more interferometric combinations with a high altitude of ambiguity, as if we had a small orbital separation (Plate 9). Moreover, if the resulting interferograms are displayed in a cartographic representation rather than the radar image geometry, we can combine interferograms from different sources, such as a descending orbital pair with an ascending one, or interferograms obtained with different satellites, such as ERS and JERS-1.

Of course, integer combination has other uses than increasing h_a between interferograms. For example, consider a geophysical event observed by interferograms produced by two satellites, with 24- and 6-cm wave-

lengths and with incidence angles such that the upward vertical components of the line of sight are 0.72 and 0.9. The vertical component of the event is eliminated by a (5, −1) integer combination of the two interferograms, without any need for unwrapping. The sensitivity of the combination to east and north components can be similarly computed. Preliminary unwrapping of interferograms of various wavelengths acquired under the same conditions (a typical situation in the Shuttle Imaging Radar missions) can also benefit by the technique.

2.5.5. Displaying and filtering tricks. A visualization trick often brings out structures on the interferogram that the eye might not otherwise detect. It suffices to rotate the fringes by translating the color lookup table cyclically with selectable speed, a feature easy to implement on most color displays.

We can use a median filter to remove errant pixels in interferograms provided that it is adapted to the cyclic character of the phase and bypasses the artificial discontinuity between 255 and 0. A solution is to first rotate the histogram to reset the minimum to zero, then estimate the median value, and finally compensate for the initial shift. This filter is a nonlinear counterpart of complex averaging (section 2.5.3).

To visualize all three channels of the interferometric product in a single color image, we may assign the intensity to the amplitude, the hue to the interferometric phase, and the saturation to the coherence, as in Plate 10.

2.5.6. Future improvements. Even if the range gradient caused by deformation on the ground exceeds the limit of one fringe per pixel, a judicious choice of image pairs may yield a usable interferogram. For example, a large orbital separation can create a fringe gradient that just compensates that of the ground deformation, bringing the geometric configuration back within the interferometric limits. Similarly, a difference in the mean Doppler between two images could compensate for rotation on the ground. In this way it should be possible to calculate useful fringes in parts of a high-gradient deformation field using an otherwise unusable image pair. However, the topographic sensitivity associated with a larger orbital separation would prevent the use of this technique in hilly terrain because it would require removing topographic effects with a proportionally accurate DEM.

3. HOW TO INTERPRET AN INTERFEROGRAM AS A GEOPHYSICAL MEASUREMENT

3.1. The Logic of Discrimination

We classify geophysical phenomena by their different temporal signatures. If its timescale is shorter than the interval between the acquisition times of the two radar images, then an event appears as instantaneous in the interferogram. We call such rapid changes "single-epoch" changes, to distinguish them from "gradual" changes.

A second criterion distinguishes permanent changes from reversible ones. A "permanent" offset appears in any interferogram spanning the date of the change. In contrast, a "reversible" phenomenon will be invisible if it produces no net change during the interval spanned by the interferogram.

These two criteria form four categories: (1) single-epoch reversible, (2) single-epoch permanent, (3) gradual reversible, and (4) gradual permanent. By considering one interferogram as the phase difference of two radar images acquired at different times, we develop a pairwise logic useful for discriminating signal from artifact [*Massonnet and Feigl*, 1995a].

A single-epoch reversible change produces a sharp spike in range as a function of time. If the spike occurs while the radar instrument "takes the picture," that image will contaminate (with constant magnitude) every interferometric pair to which it contributes (Plate 11). By comparing several interferograms, we can distinguish a single-epoch reversible signature from a permanent offset in range. After identifying the contaminated image, we can determine the sign of the perturbation: lengthening or shortening.

Such a single-epoch reversible range change appears as a single closed fringe (28 mm) shaped like a kidney some 25 by 20 km in Plates 12a, 12b, and 12c. Each of these interferograms involves the image acquired on July 3, 1992. Yet the kidney-shaped feature does not appear in Plate 12d, which spans a longer time interval than the other three pairs. Hence we can exclude deformation on the ground as the explanation. Furthermore, the number of fringes does not depend on h_a, excluding topographic effects. Since the feature corresponds to a range shortening (decrease in travel time), we interpret it as "hole" in the ionosphere. Such an area of locally decreased electron density decreases the refractive index for the radar signal. Another example of an ionospheric signature appears as singular triangular fringe (3 cm) over Mount Etna (Plate 31d). The causal mechanism appears to be local neutralization of the ionosphere, on the basis of theoretical estimates [*Tarayre and Massonnet*, 1996]. As a result, ionospheric perturbations are likely to be more severe near the geomagnetic equator and poles than at intermediate latitudes.

To remove such an ionospheric signature, we could exploit the dispersive nature of the ionosphere. Since the propagation delay through the ionosphere is inversely proportional to the square of the radar frequency in the microwave part of the spectrum, a judicious combination of phase measurements at two different frequencies eliminates the ionospheric contribution. Although this trick is routine in processing phase data from GPS satellites, it requires two images acquired simultaneously at different frequencies to work for radar interferometry, as planned for the *ECHO Elsie* mission under consideration by *NASA* and CNES.

A second type of atmospheric perturbation involves water vapor or turbulence in the troposphere. In the

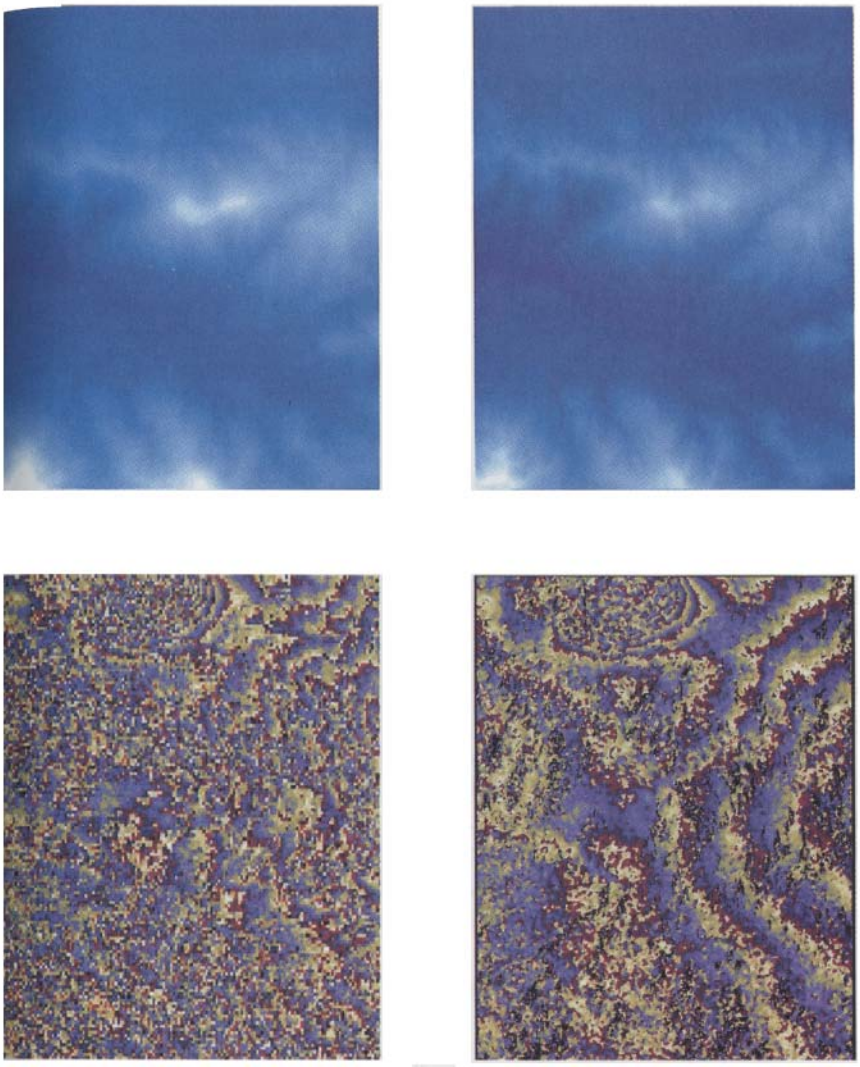

Plate 8. Two interferograms (bottom row) calculated with the same pair of ERS-1 radar images but using two DEMs that differ in resolution and precision (top row). (left) A DEM with 1200 points per degree of latitude or longitude, and a published uncertainty of 30 m [*USGS*, 1993]. (right) A DEM with 3600 points per degree and an uncertainty of better than 10 m [*USGS*, 1993]. Using the high-resolution DEM (left) produces a clearer interferogram. The improvement is sufficient to identify coseismic fringes displacement produced by a $M_w = 5.3$ earthquake located in the San Bernardino Mountains (July 12, 1992). The deformation caused by the small earthquake appears at the top of the interferogram. The wider fringes are part of the deformation field of the Big Bear earthquake of June 28, 1992. See also Plate 15.

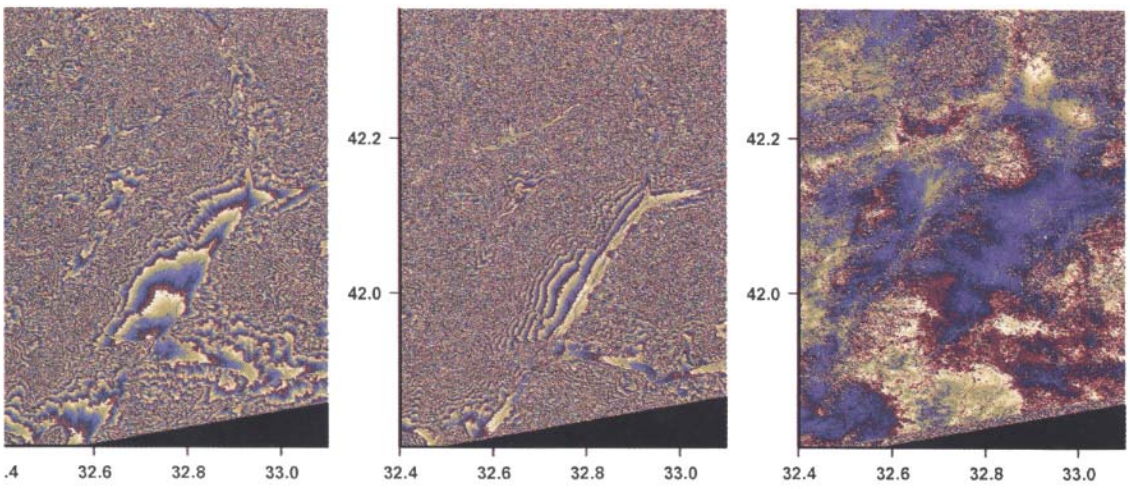

Plate 9. Integer interferometric combination in Anatolia, Turkey. Since we could not find a DEM, we produced two uncorrected interferograms (left and middle panels) with very dense fringes from four ERS-1 radar images. At some places in the interferograms, it is difficult to decide whether coherence has been lost or the fringe pattern is too dense. The interferograms have h_a values of 59 m and 29.4 m, respectively. We apply the integer interferometric combination $(2, -1)$ described in section 2.5.4, leading to a combined interferogram (right panel) with an equivalent h_a of over 4000 m, almost eliminating topographic fringes. The result shows that the noisy-looking areas in both initial interferograms actually contain signal. Axes are labeled in degrees of latitude and longitude.

worst case observed so far, we count as many as three closed fringes (9 cm) in several irregular patterns each 5–10 km wide (Plate 5, right). The same patterns appear in two interferometric pairs, both of which involve the image acquired on August 27, 1993 [see *Massonnet and Feigl*, 1995a; Figure 5]. However, the patterns do not appear in an interferogram spanning that date [*Massonnet et al*., 1994a; Figure 2a]. By pairwise logic we infer that the patterns are due to variations in the atmosphere and not to motion on the ground. Water vapor retards the radar signal as it propagates through the troposphere. In this case the signal passes through a thunderstorm, as is confirmed by towering cumulonimbus clouds observed from the ground as well as in an optical satellite image taken within an hour of the radar image [*Massonnet and Feigl*, 1995a]. Other such tropospheric artifacts appear in interferograms as crenulated fringes in several roughly round patches. Although such features tend to resemble clouds, water vapor does not need to be visible to perturb the microwave radar signal. Tropospheric perturbations are a consequence of turbulence, due either to convection or to wind interacting with topographic relief [*Goldstein*, 1995; *Tarayre and Massonnet*, 1996; *Zebker et al*., 1997]. Their magnitude is smaller in radar images acquired at night than in images obtained during the day, on the basis of our experience with many interferograms.

Although the pairwise logic can identify atmospheric signatures, it cannot remove them from interferograms. Correcting tropospheric artifacts with a horizontal resolution of ~100 m would require meteorological information at the same scale, a level of detail well beyond currently available models and observation techniques. Consequently, tropospheric effects are likely to remain the limiting source of error in the interferometric measurement. Other studies also describe atmospheric effects in radar interferograms [*Rosen et al*., 1996; *Zebker et al*., 1997; *Delacourt et al*., 1998].

Yet another type of single-epoch reversible effect involves variations in the frequency standard of the satellite oscillator (Figure 4, section 1.2.6).

The simplest example of a single-epoch permanent signal is the coseismic deformation produced by an earthquake (Plates 18–20, section 4.2). Its temporal signature is a Heaviside step function, which produces an essentially instantaneous movement.

One intuitive example of a gradual reversible change is the response of the continental crust to periodic loading by ocean tides (Plate 37, section 4.8.3). Depletion and replenishment of groundwater aquifers can also create seasonal cycles of subsidence and uplift (section 4.4). Volcanic and faulting processes might also reverse the sign of their deformation signatures. If the reversal produces no net change during the sampling time between two radar images, then it will not appear in the resulting interferogram. Avoiding such temporal aliasing requires a sampling time shorter than the reversal time.

Seasonal changes in the atmosphere might also create a gradual reversible change in radar travel time. Such a change will not appear in an interferogram unless it varies over the image area, a case we consider in sections 1.2.5 and 3.2.

Gradual permanent phenomena include ground subsidence (section 4.4), glacier flow (section 4.5), landslide movement (section 4.6), volcanic deformation (section 4.7), and postseismic fault activity (section 4.8.1).

3.2. Artifacts Related to Topography

If the DEM used to eliminate the topographic contribution is in error, the interferogram will contain artifactual fringes. They appear in the same location in every interferogram produced using that DEM. The number of fringes is inversely proportional to h_a. As an extreme (and rare) example, Plate 13 reveals a topographic error $\varepsilon \approx 250$ m, roughly 8 times larger than the published precision for the DEM. This artifact resembles the fringe pattern produced by a small earthquake (Plate 20).

It is possible to misinterpret such artifactual fringes as deformation if the deformation field resembles the topographic surface. This case occurs where a topographic structure represents the accumulated effect of many repeated deformation events, as for upwelling volcanoes, uplifting folds, and subsiding grabens. For example, a vertical normal fault scarp growing at ~5 mm yr^{-1} would produce about a third of an ERS fringe in an interferogram spanning 2 years. With $h_a \approx 30$ m, one third of a fringe would also occur if the DEM contained an error $\varepsilon \approx 10$ m at the fault. In this case, one might confuse 2 years of incremental fault movement with 2000 years of accumulated growth. Avoiding such confusion requires looking at several interferograms with different time spans and values of h_a. For an earthquake the number of coseismic fringes does not depend on h_a.

Another artifact can also potentially confuse a topographic signature with a displacement. Consider the troposphere in hydrostatic equilibrium above a rigid mountain (Figure 7). The radar delay is proportional to the total amount of water vapor between the ground and the satellite and thus is (roughly) inversely proportional to the topographic elevation of the ground point. If the scale factor changes from one satellite pass to the next, the radar delay will differ between the two radar images, producing fringes that "hug" the topography like contour lines but that measure the change in tropospheric delay. This effect appears to be responsible for the fringes in interferogram of Mount Etna in Plate 14. The fringes do not represent volcanic deformation, because the two images are only 1 day apart. One can recognize this subtle effect by pairwise logic and can model it using the DEM and local meteorological observations [*Delacourt et al*., 1998].

3.3. Evaluating the Measurement Uncertainty

A topographic error of ε meters in the DEM will produce a phase error of ε/h_a cycles in the resulting interferogram. To obtain an error estimate in millime-

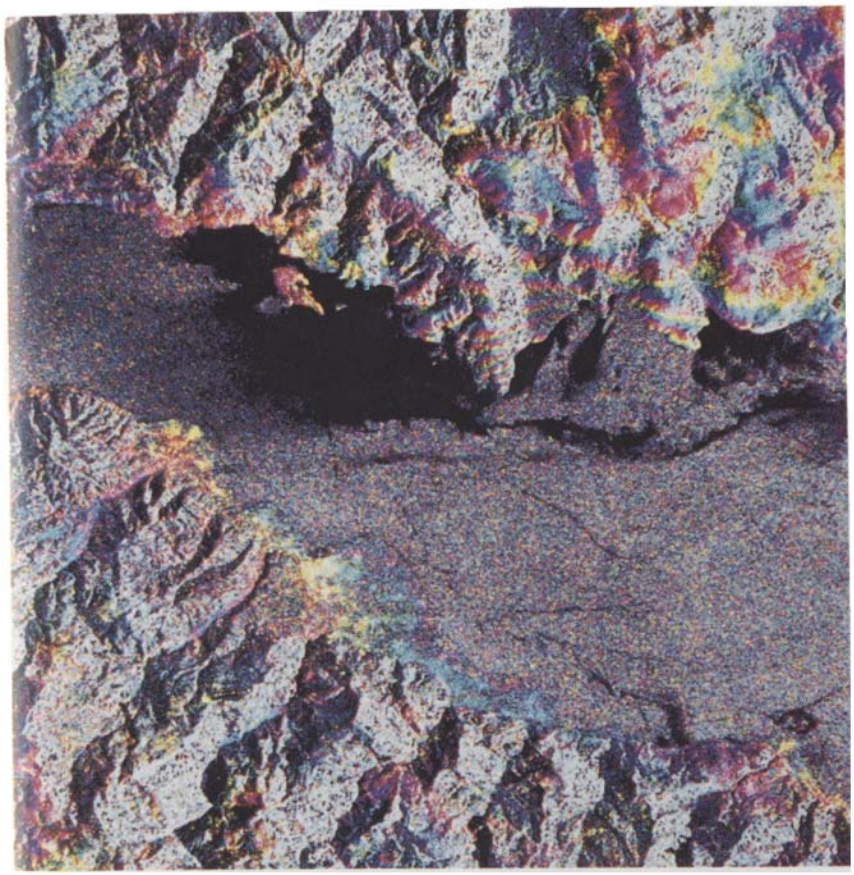

Plate 10. Interferogram of Gulf of Corinth (Greece) by ERS-1 displayed with intensity-hue-saturation (IHS) inverse transform. The figure is made by first assigning the amplitude of the radar image to the intensity channel, the phase of the interferogram to hue, and the associated coherence to saturation, and then performing an inverse IHS transform to reconstruct the conventional red, green, and blue channels. The image is colored only where the fringes are coherent (i.e., where we have a high saturation). Incoherent areas appear in black and white, thus erasing meaningless phases. Further attenuation occurs in part of the Gulf of Corinth where the water is very dark, leading to low intensity and low coherence. The coseismic deformation from the Aigion earthquake appears as several fringes on the northern coast of the gulf [*Bernard et al*., 1996].

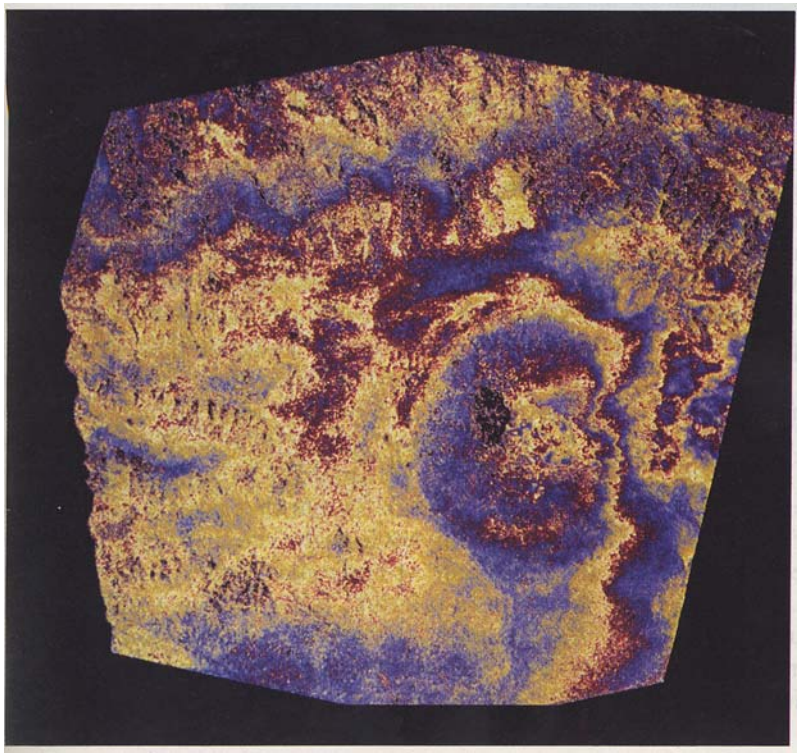

Plate 11. Interferogram of Mount Etna using ERS-1 and ERS-2 data acquired during the tandem mission on June 27 and 28, 1995. The objective of this mission is to provide interferometric pairs of images separated by only 1 day and hence of high coherence. Having two satellites in operation increases the number of orbital opportunities with good values for the altitude of ambiguity. However, images 1 day apart are useful only for measuring rapid geophysical phenomena, such as glacier movements. Opportunities for such measurements are still separated by 35 days. Finally, tandem data do not correct the main problem in differential interferometry: the atmospheric contribution, as illustrated by this differential interferogram. Orbital and topographic contributions have been eliminated using the same techniques as for Plate 31. We do not expect much volcanic deformation during the 1-day interval between data acquisitions. The observed signal must therefore correspond to an atmospheric heterogeneity during the acquisition of one or both images. Indeed, atmospheric situations 1 day apart may differ as much as atmospheric situations 35 days apart. The area covers the entire mountain.

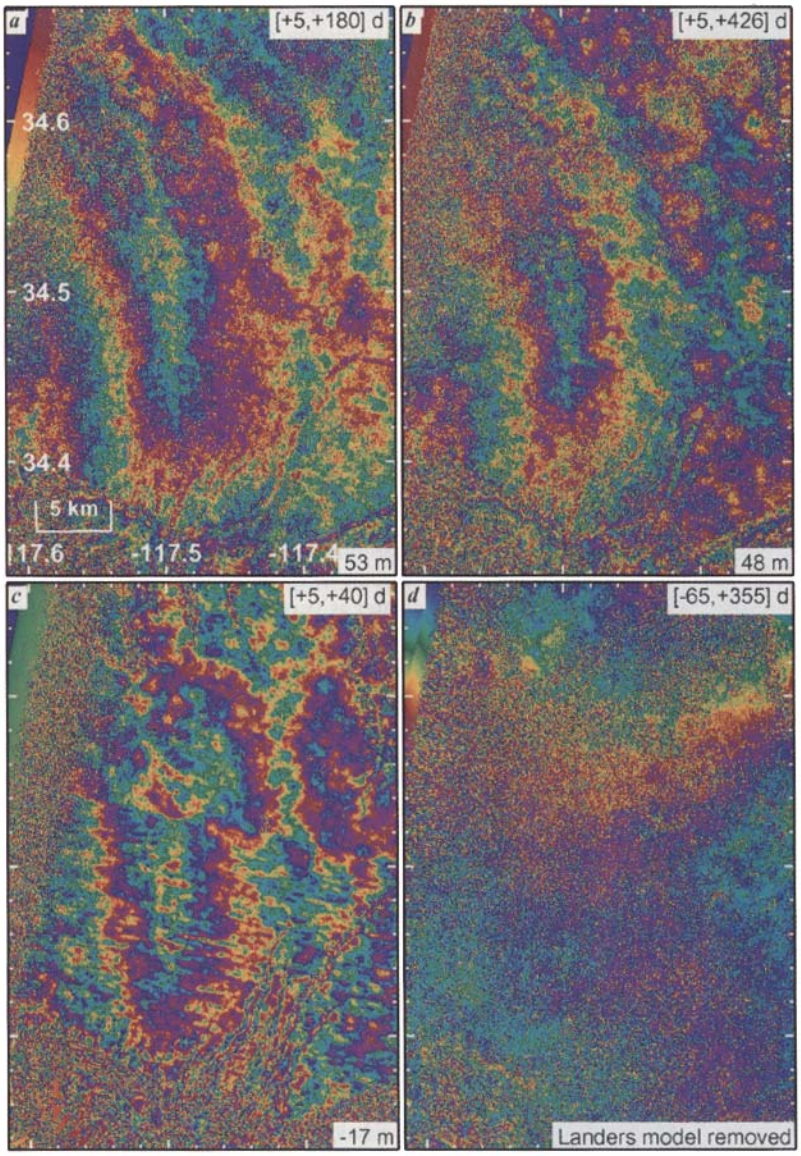

Plate 12. Kidney-shaped feature apparently produced by an ionospheric perturbation in the radar image acquired on July 3, 1992 (5 days after the Landers mainshock). This feature appears in the interferometric pairs spanning the intervals (a) [+5, +180], (b) [+5, +426], and (c) [+5, +40] days relative to the mainshock, but not in the pair spanning (d) [−65, +355] days. The fringes caused by the Landers mainshock in Plate 12d have been removed by subtraction of the range changes predicted by a fault-slip model [*Hudnut et al*., 1994] and a planar fringe ramp. In each panel the altitude of ambiguity h_a is at bottom right, and tick marks are every 0.02° in latitude and longitude. The kidney appears each time the +5 day image contributes to the interferogram. From *Massonnet and Feigl* [1995a].

ters, we multiply ε/h_a by half the radar wavelength. Errors in typical DEMs range from 10 to 30 m [*Wolf and Wingham*, 1992], implying that choosing a pair of images with h_a between 20 and 60 m will yield an interferometric measurement with an error better than $\varepsilon/h_a = \pm 1/2$ cycle, or ±14 mm for ERS. Small values of h_a can mask even large signals with artifactual topographic fringes (Plate 15).

Displacements measured both by radar interferometry and GPS surveying have been compared only for the two California earthquakes at Landers and Northridge. At Landers we project the GPS estimates of vector displacement [*Hudnut et al*., 1994] onto the radar line of sight to calculate the scalar change in range. We retain only those bench marks measured by the U.S. Geological Survey (USGS) with identical GPS instruments both before and after the earthquake. To measure the absolute range change, we count the fringes in the early coseismic interferogram [*Massonnet et al*., 1993b]. For Northridge, *Murakami et al*. [1996] use the GPS measurements of *Hudnut et al*. [1995] to adjust the orbital parameters for their JERS-1 interferogram. We plot the final radar estimate of range change against the GPS-derived estimate in Figure 8. The root-mean-square (rms) scatter is 35 mm for the ERS-1 interferogram and nine GPS sites at Landers, and 16 mm for the JERS-1 interferogram and seven GPS sites at Northridge. Note, however, that the vertical component of displacement, the least reliable part of the GPS estimate, is the one that contributes most heavily to the range, because of the steep radar incidence angle. Also note that the rms difference in range of 35 mm we calculate at Landers is not directly comparable to the rms difference of 189 mm in the magnitude of horizontal displacement calculated by *Zebker et al*. [1994a].

We can assess the precision of the range measurements in a radar interferogram by using a physical model to fit them. Using a simple elastic dislocation model, we can find the rms scatter of the residual (observed minus calculated) range changes to be 5 mm, 6 mm, and 37 mm

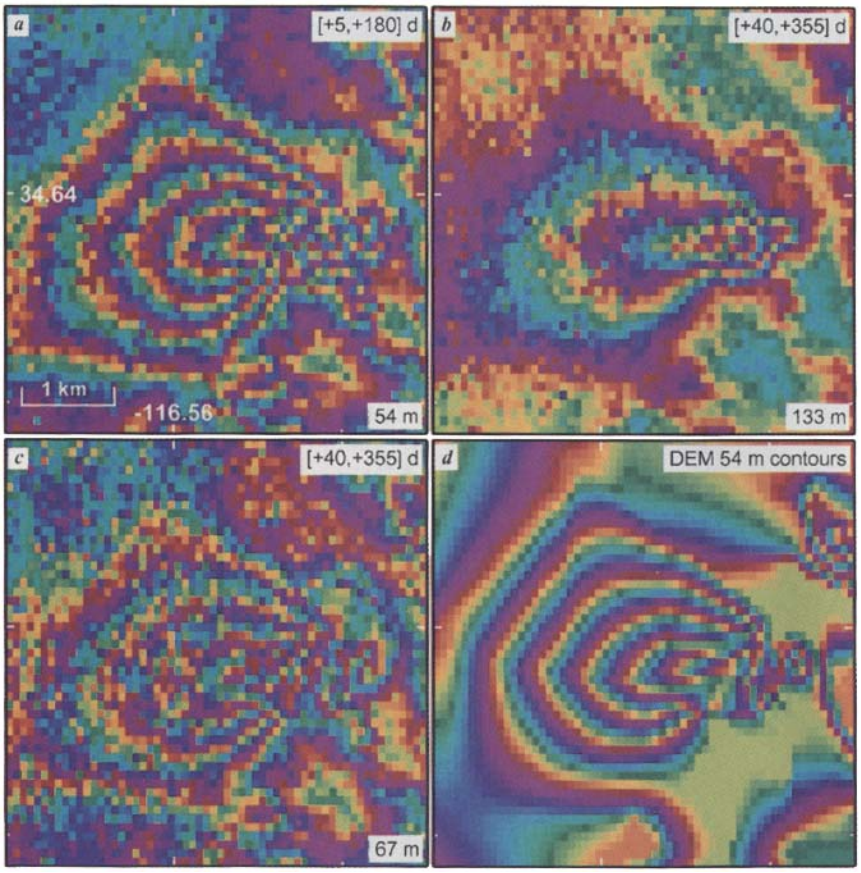

Plate 13. Anomalous rhomboid feature produced by a DEM error in several interferograms near Landers, California [*Massonnet and Feigl*, 1995a]. (a) Interferogram spanning the interval [+5, +180] days (relative to the Landers mainshock) with altitude of ambiguity h_a = 54 m. One complete cycle of color corresponds to one cycle (28 mm) of change in range. Time intervals are at upper right, h_a is at bottom right, and tick marks are every 0.02° in latitude and longitude. (b) Interferogram spanning the interval [+40, +355] days, with h_a = 133 m. (c) Same interferogram as in Plate 1b, but multiplied by an integer factor of 2 to simulate h_a = 67 m, similar to Plate 13a. (d) Corresponding section of the DEM with a contour interval equal to the 54-m value of h_a for Plate 13a. Plate 13a exhibits a rhomboid feature with four fringes (12 cm) [*Massonnet and Feigl*, 1995a]. The feature also appears, but as only two fringes, in Plate 13b, where h_a = 133 m. Multiplying the interferogram in Plate 13b by an integer factor of 2 produces Plate 13c, which, with an effective h_a of 66 m, resembles Plate 13a. Therefore the rhomboid feature results from an error of ~250 m in the DEM, roughly 8 times larger than the published precision [*U.S. Geological Survey* (*USGS*), 1993]. The contoured DEM (Plate 13d) reveals a hill that is not present in the 1:62,500 USGS topographic map [*USGS*, 1955]. The shape of the fictitious peak in the DEM is reproduced in the interferograms.

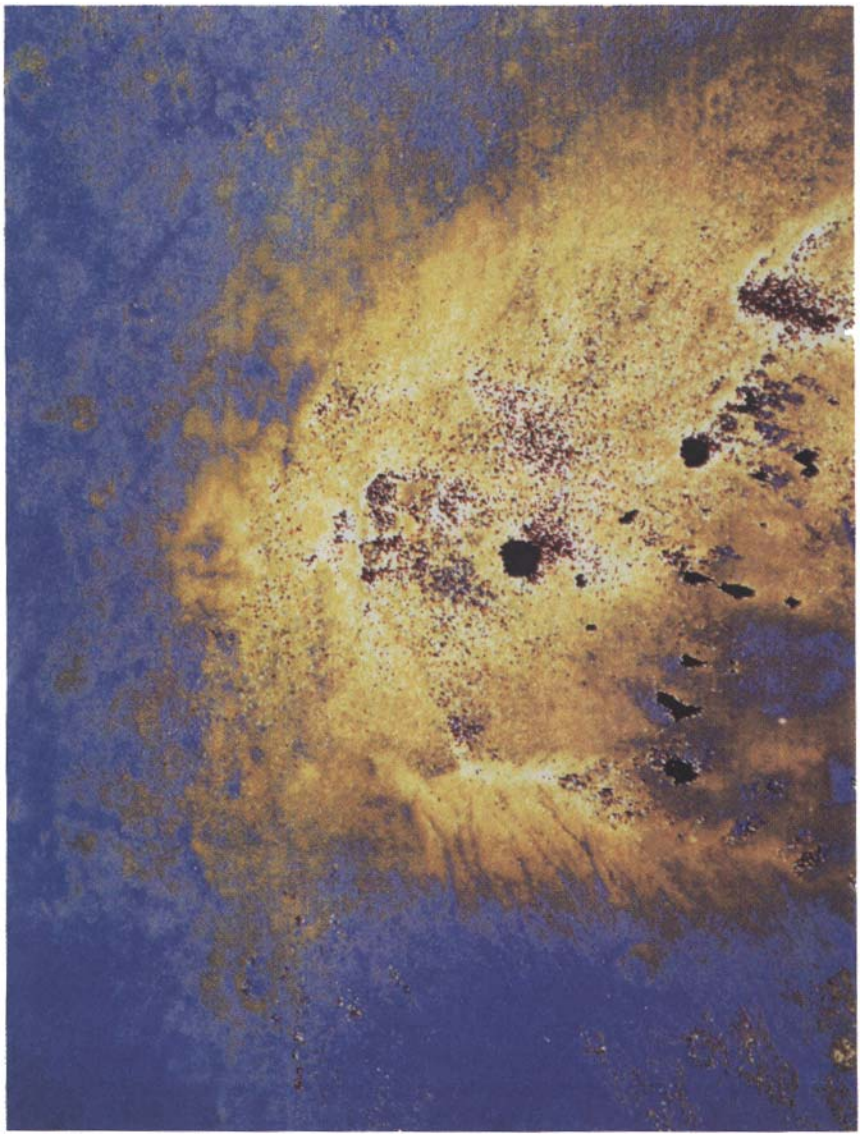

Plate 14. An example of the static-tropospheric effect over Mount Etna described in Figure 7. The interferogram produced from two C band images acquired 1 day apart by the space shuttle (SIR-C mission) has been corrected for topographic and orbital contributions. The remaining phase pattern of as much as half a cycle mimics the topography of the volcano. As for Plate 11, we do not expect such phase changes to be due to ground displacements taking place in only 1 day. First-order assessment of the meteorological parameters at the time of the acquisitions reproduces the order of magnitude of the observed effect. However, the simple model we used cannot completely eliminate the artifact. The area covers the entire mountain. Raw data from SIR-C have been graciously provided by NASA JPL.

for the Fawnskin, Eureka Valley, and Landers earthquake interferograms, respectively (Figure 9). These values are larger than the uncertainty expected from propagation of topographic errors: 4 mm, 3 mm, and 9 mm, respectively [*Massonnet et al.*, 1993b; *Feigl et al.*, 1995; *Massonnet and Feigl*, 1995b].

Similarly, we can estimate the accuracy at short wavelengths by subtracting a smoothed version of the interferogram from the unfiltered one. The resulting residual consistently shows an rms scatter of 0.08 C band fringes (2 mm) over a flat area without agriculture in the Imperial Valley (Plate 25, section 4.4) [*Massonnet et al.*, 1997].

To determine the absolute accuracy of interferometric measurements of displacements, *Gray and Farris-Manning* [1993] devised a clever experiment using airborne radar. They placed five corner reflectors in the image scene and displaced one of them on a precision micrometer stage by 25, 15, and 10 mm between successive passes of the airplane carrying the radar instrument. The phase difference of the displaced reflector relative to the stationary background yields the range change caused by the translation, and by geometry (equation (3)), the displacement. The authors correctly estimated the displacements as 26.1, 16.9, and 8.9 mm using the C band radar and 25.4, 16.3, and 9.3 mm using X band, each with an uncertainty of ± 1.5 mm, on the basis of the phase noise. The mean difference between the radar and micrometer measurements is 1.1 mm. Although this experiment attains an accuracy of a single millimeter in displacement, the results may not apply directly to natural targets observed by satellite.

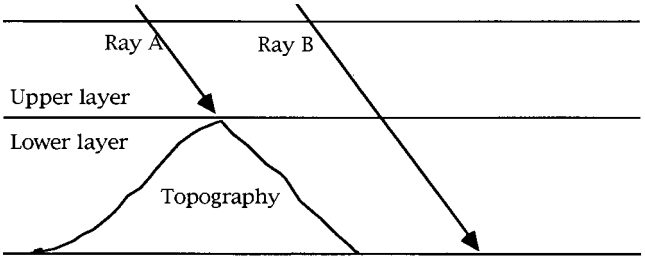

Figure 7. Sketch of hydrostatic troposphere effect. Topography can reveal homogenous changes in the atmosphere. Drawing an imaginary line at the elevation of the highest topography helps explain the phenomenon. Rays A and B will cross the layer above this line at acquisition times 1 and 2. The change in apparent atmospheric thickness (assumed homogenous in space) between times 1 and 2 will create a constant path difference in the interferogram. Such a difference is not observable by interferometry because the technique does not provide an absolute measurement of phase. The situation is different in the lower layer, which will not be crossed by ray A. Any homogenous change in the lower layer will cause an additional change in the path length between the two rays. This effect creates a topography-like atmospheric signal, in the sense that topography is required to reveal the phenomena. However, the signal is not related to the altitude of ambiguity of the pair. Unlike heterogeneous effects, there is some hope that we can correct these effects, using our knowledge of the topography, if they are linked to a limited number of atmospheric parameters. If the atmosphere is really homogenous, these parameters could be obtained from weather stations far from the study area. We could also estimate their values by minimizing the residual fringes through trial and error.

4. GEOPHYSICAL APPLICATIONS

We can classify the different phenomena of crustal deformation by rate and duration (Plate 16). Earthquakes, for example, displace the crust with high rate (~ 1 m s^{-1}) but short duration (~ 10 s). At the other extreme, postseismic relaxation and postglacial rebound of the lithosphere are slow in rate (~ 1 mm yr^{-1}) but long in duration (10^1–10^3 yr). Between these two extremes lie 10 orders of magnitude in rate and 6 in duration. In this section we catalogue successful interferograms according to these two scales, proceeding from short and fast to long and slow. Note, however, that it is the product of rate and duration that gives the magnitude of the deformation, the quantity actually measured by interferograms. To be detectable, the movement should fall to the right of the red lines in Plate 16.

Since the ocean surface can move at rates as high as ~ 1 m s^{-1}, the two-pass satellite technique will not work. Instead, an airplane with two antennas mounted fore and aft takes both radar images within about a tenth of a second, as was proposed by *Goldstein and Zebker* [1987], extending *Raney*'s [1971] two-antenna, stationary target-canceling scheme. It is thus possible to observe a Doppler shift related to the phase velocity of the water waves. Since this oceanographic measurement differs from the solid Earth focus of this paper, we refer the interested reader to the relevant articles [*Goldstein et al.*, 1989; *Marom et al.*, 1990, 1991; *Shemer and Kit*, 1991; *Shemer et al.*, 1993; *Thompson and Jensen*, 1993; *Shemer*, 1995; *Ainsworth et al.*, 1995].

4.1. Detectability: Restrictions on Magnitude and Spatial Extent

To decide whether a crustal signal is measurable by radar interferometry, we consider two other parameters, the magnitude of the crustal movement and the spatial scale over which it occurs (Plate 17). Both have units of distance. At one extreme we have the fundamental mode of the Earth's free oscillation, which produces small movements ($\sim 10^{-6}$ m) over long wavelengths (10^7 m). At the other extreme, faults typically produce offsets that are large in magnitude ($\sim 10^1$ m) over very short distances ($\sim 10^1$ m). Yet interferometry cannot measure these extreme cases directly because they are beyond the interferometric limits described in section 1.3. On a logarithmic plot of magnitude versus width, the limits appear as five lines, forming a truncated parallelogram that bounds the area of detectable signals. None of these

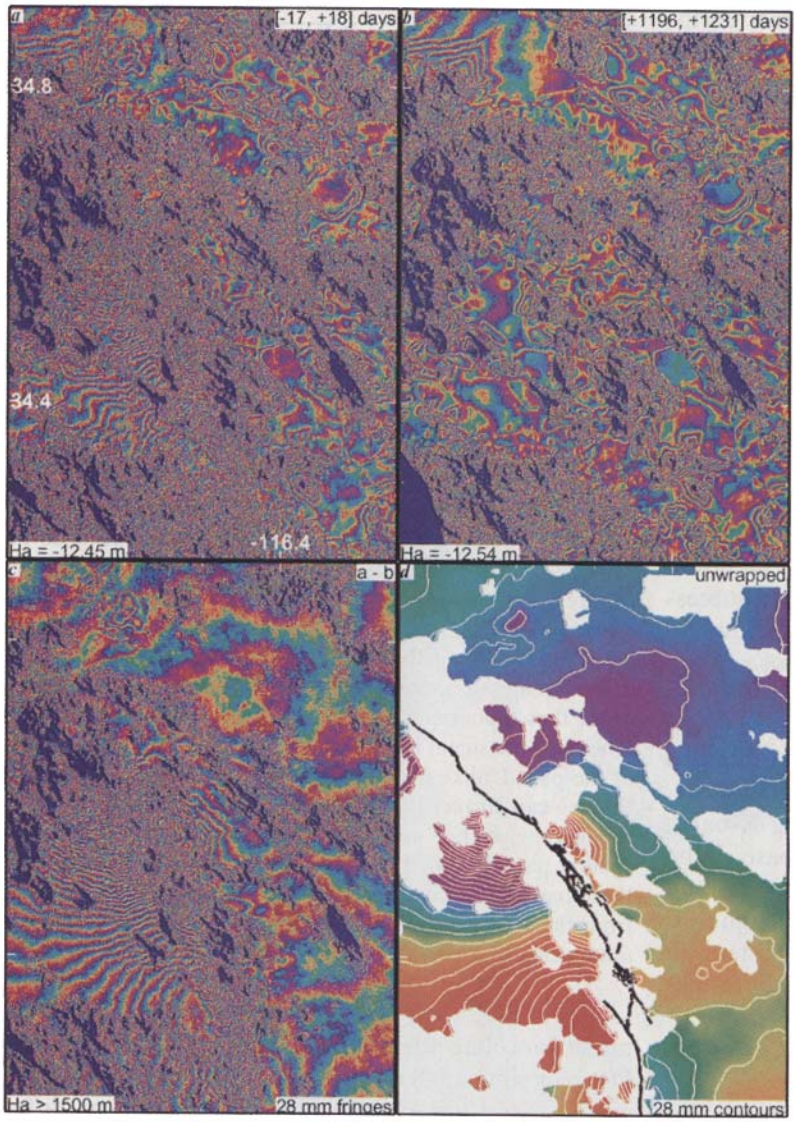

Plate 15. Landers earthquake interferograms calculated from "ascending" orbital pairs. (a) Images acquired on June 21 and July 26, 1992, spanning the interval [−17, +18] days relative to the mainshock. At 34.0°N, 116.0°W, we have $h_a = -12.45$ m, close to the lower interferometric limit (relation (1)). Although the coseismic deformation pattern appears vaguely in the northern part of the interoferogram, it is difficult to separate from residual topographic fringes because the DEM's rms error of 30 m is larger than h_a. Dark areas show where the local topographic slope exceeds the interferometric limit (1). One fringe represents 28 mm of range change. (b) Images acquired on October 7 and November 11, 1995, spanning the interval [+1196, +1231] days relative to the mainshock. Here $h_a = -12.54$ m. (c) Integer combination of the previous two interferograms. Here the effective altitude of ambiguity over 1500 m, essentially eliminating the topographic contribution. One fringe represents 28 mm if all the deformation is coseismic in Plate 15a. (d) Unwrapped, filtered and contoured version of the combined interferogram in Plate 15c [*Trouvé*, 1996]. The full range of color spans −558 mm to +994 mm. Black lines show surface rupture as mapped in the field [*Sieh et al.*, 1993]. In all four panels the axis of the radar antenna is oriented parallel to the local unit vector $\hat{\mathbf{s}} = [-0.399, -0.081, +0.913]$ in east, north, and upward directions, providing a different perspective from the "descending" interferograms in Plate 20.

boundaries are truly "hard" limits because processing tricks exist for overcoming them all. For this reason, we plot them as gradational boundaries in Plate 17.

The "pixel size limit" restricts the spatial extent of an observable movement to values much larger than the dimension of a focused radar pixel. Deformation at smaller spatial scales, such as spalling in sidewalk pavement, does not appear in interferograms.

Similarly, the deformation is easiest to interpret if it fits within the ~100-km width of the radar swath. This "swath width limit" is discussed in section 1.3.4. It is possible to study broad signals by abutting successive radar images along the swath (parallel to the satellite ground track), but it is not straightforward to join two adjacent swaths (across track) because they do not start and end at exactly the same times. Nor is the radar incidence angle the same at the abutting edges, slightly changing the orientation of the radar antenna "look" vector $\hat{\mathbf{s}}$.

The fringe pattern becomes incoherent if the spatial gradient of the range measurement exceeds some fraction of a fringe within the confines of a single pixel, as is discussed in section 1.3.2. In practice, this condition restricts interferometric measurement to strains smaller than about 10^{-3}. Abrupt changes in topography, such as volcanic eruptions, can exceed this limit. Discontinuities such as surface rupture also exceed this limit because they produce an infinite gradient. In this case, however, we can still measure the relative motion on opposite sides of a fault by counting fringes along a path which runs around the end of the fault [*Massonnet et al.*, 1993b, Figure 3b].

The deformation is significant only if it produces a range change larger than the measurement uncertainty. This "small-gradient limit" restricts interpretation to signals with magnitude of the better part of a fringe (~1 cm) over a scene (~100 km), or strains larger than 10^{-7}. Tidal loading of the continents produces deformation close to this limit (Plate 37, section 4.8.3). Smaller signals are detectable if they are strongly structured like the atmospheric waves in the left panel of Plate 5. Below this limit, we encounter residual orbital fringes (section 1.2.2), gentle ramps of atmospheric changes across the

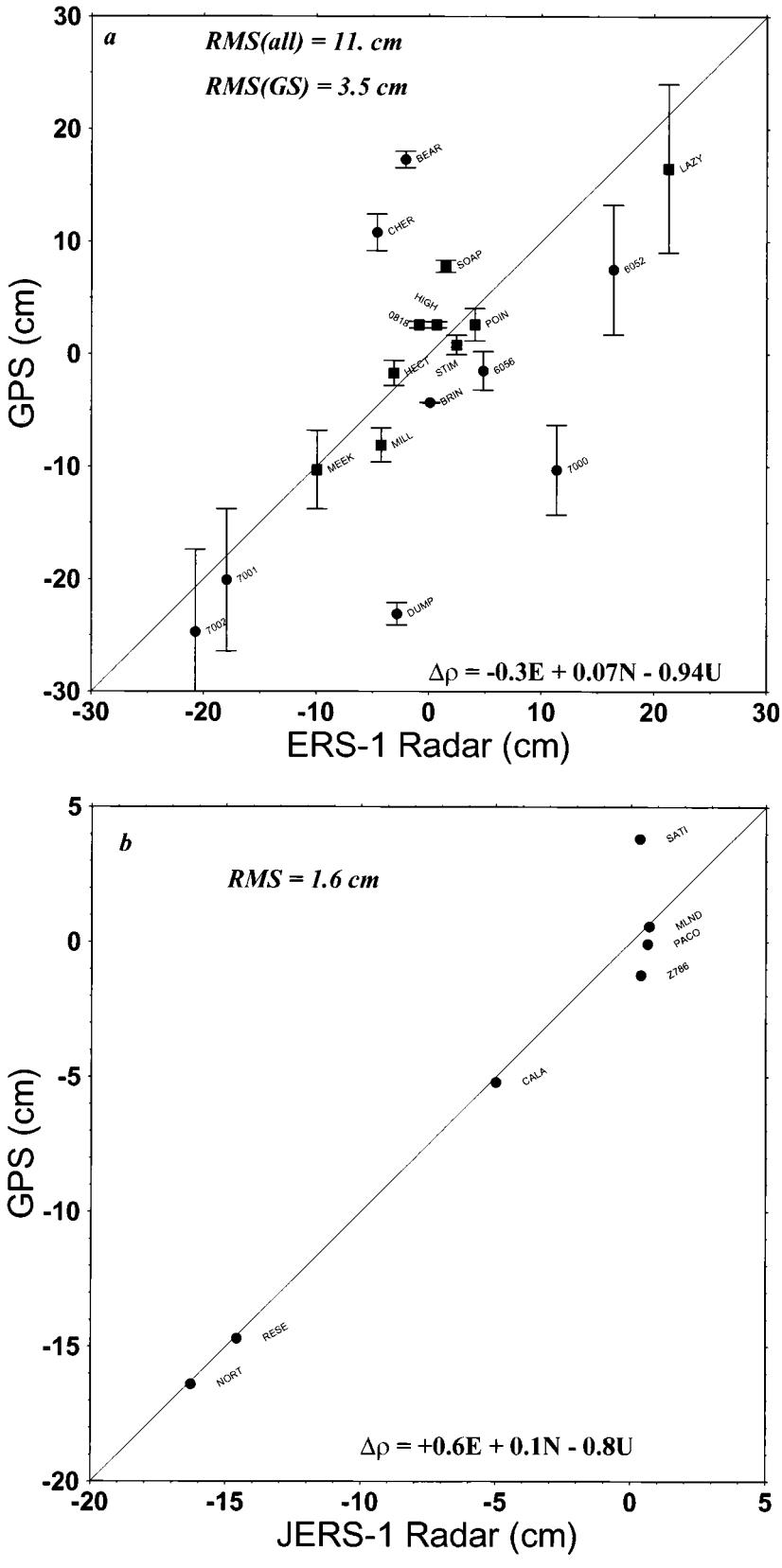

Figure 8. Comparison of GPS and radar measurements of coseismic range change for the (a) Landers and (b) Northridge earthquakes. For Landers the two measurements are the number of fringes counted in the ERS-1 interferogram [*Massonnet et al.*, 1993b] and the GPS estimates of vector displacement [*Hudnut et al.*, 1994] projected onto the radar line of sight. Squares denote the nine GPS sites measured by the U.S. Geological Survey with identical instruments both before and after the earthquake. Circles denote other GPS measurements. The standard deviation of the GPS-radar difference is 3.5 cm for the nine USGS sites (squares) and 11 cm for all 19 sites. The four-letter code denotes the bench mark as assigned by *Hudnut et al.* [1994, Table 1]. For Northridge the plot compares the radar JERS-1 interferogram calculated by *Murakami et al.* [1996] and the GPS displacement measurements from *Hudnut et al.* [1995]. The standard deviation of the residual difference is 16 mm, after the orbital adjustment.

image (section 1.2.5), or moderate clock artifacts (section 1.2.6).

Resolving phase differences smaller than about one tenth of a cycle is difficult (section 1.3.6). For a C band radar such as ERS, this cycle-slicing limit restricts detection to signals larger than several millimeters. For L band instruments such as JERS-1, the equivalent threshold is 4 times larger.

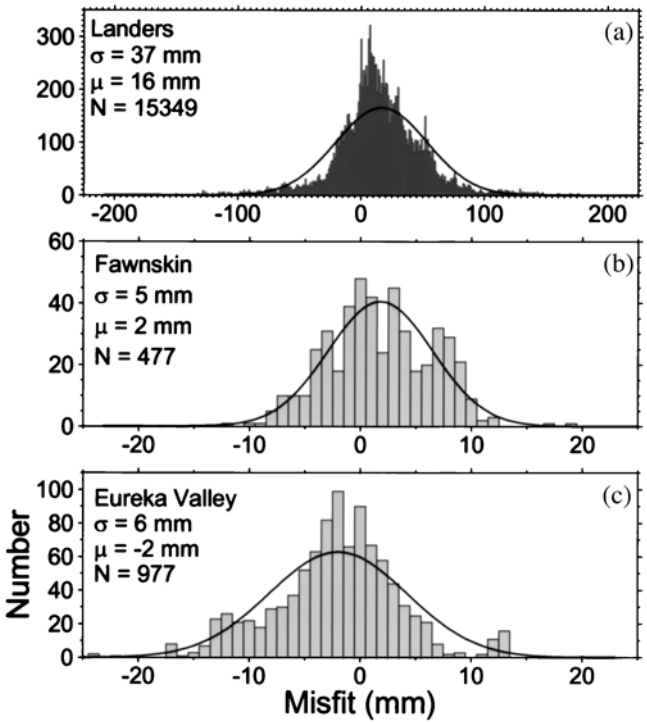

Figure 9. Histograms for residual (observed minus modeled) range change for three earthquakes using simple elastic dislocation models. Standard deviation σ, mean μ, and number of data points *N* apply to each distribution. (a). Landers using the interferogram of *Massonnet et al*. [1993b] and the multiple-patch, variable slip model of *Feigl and Peltzer* [1993] and *Feigl and Massonnet* [1995], shown in Plate 21. The skewness of the distribution corresponds to data points on the "wrong" side of the modeled fault segment. (b) Fawnskin using the interferogram of *Massonnet et al*. [1994a] and the single-patch focal mechanism estimated by inverting it [*Feigl et al*., 1995]. (c) Eureka Valley [*Massonnet and Feigl*, 1995b].

4.2. Earthquakes

To capture an earthquake, a satellite must acquire one radar image before the earthquake and one after the earthquake. In addition, these two images (together with a DEM or a third image) must satisfy all the interferometric requirements described in section 1.3. Yet even under these conditions, not all earthquakes create interferometric fringes. To appear in an interferogram, the vector displacements in a coseismic deformation field must have sufficient magnitude and proper orientation. In practice, moderate ($M > 5$) earthquakes at shallow depth (<10 km) with dip-slip mechanisms (and thus predominantly vertical surface displacements) can generate clear fringe patterns.

4.2.1. A moderate thrust mechanism. As a pedagogic example we present a small $M_w = 5.1$ earthquake near Fawnskin, California, on December 4, 1992. This aftershock in the Landers sequence produced a coseismic bulge that appears as four concentric fringes (12 cm) in Plate 18a. These fringes center on a point less than 2 km from the epicenter estimated from regional seismograms [*Hauksson et al*., 1993].

The concentric fringes are clearest in the interferogram spanning the interval [−65, +355] days relative to the date of the main Landers shock on June 28, 1992. They also appear in the interferograms for the intervals [+5, +180] days (not shown) and [+40, +355] days (Plate 18b) but not in the interval [−65, +40] days (Plate 18c). By elimination, the event that produced these fringes must have occurred in the interval [+40, +180] days, that is, between August 7 and December 25, 1992. The number of fringes does not change with time, as can be expected for permanent coseismic deformation.

Unlike most of the other Landers aftershocks with magnitude greater than 5, the event at 0208 UT on December 4 has a thrusting *focal mechanism* [*Hauksson et al*., 1993; *Jones and Hough*, 1994]. Such a mechanism displaces the ground surface mostly in the upward direction, the component best resolved by the ERS geometry. The shallow hypocentral depth of 2 km [*Hauksson et al*., 1993] creates larger displacements at the surface than do deeper events of the same magnitude.

The concentric fringes are not an artifact caused by a DEM error because the number of fringes remains the same in Plates 18a and 18b despite a twofold change in h_a. Indeed, the difference of these two interferograms does not show the concentric fringes, indicating that the feature has constant shape, position, and magnitude.

From these arguments we conclude that the December 4 aftershock generated the observed fringes because it is the only thrusting aftershock in the catalog with $M_L > 5$ and depth < 5 km to occur at the right place and the right time [*Hauksson et al*., 1993].

To explain the observed fringes, we use a dislocation model to simulate the coseismic interferogram (Plate 18d). It predicts a fringe pattern that mimics the observed interferogram. The residual interferogram (Plate 18e), calculated by subtracting the simulated fringes from the observed fringes, shows little unexplained signal, 0.4 cycles rms, or 12 mm in range. The residuals calculated from the subset of the data used in the inversion have an rms scatter of 5 mm in range (Figure 9b).

4.2.2. A complex thrusting event. The Northridge earthquake released some 3 m of slip along a 15-km-long thrust fault under suburban Los Angeles, California, on January 17, 1994 [*USGS and Southern California Earthquake Center*, 1994]. In the process, the magnitude 6.7 event displaced the Earth's surface by as much as 43 cm vertically and 20 cm horizontally, creating four fringes in the first earthquake interferogram calculated using SAR data from the L band Japanese JERS-1 satellite [*Murakami et al*., 1996].

Northridge provides an interesting case study because two different interferograms record its effects on an urban area [*Massonnet et al*., 1996a]. The first (Plate 19a) uses radar echoes in L band (235-mm wavelength) acquired by JERS-1, the second (Plate 19b) uses C band (56-mm wavelength) data acquired by ERS-1. The ERS-1 geometry is almost two times more sensitive to

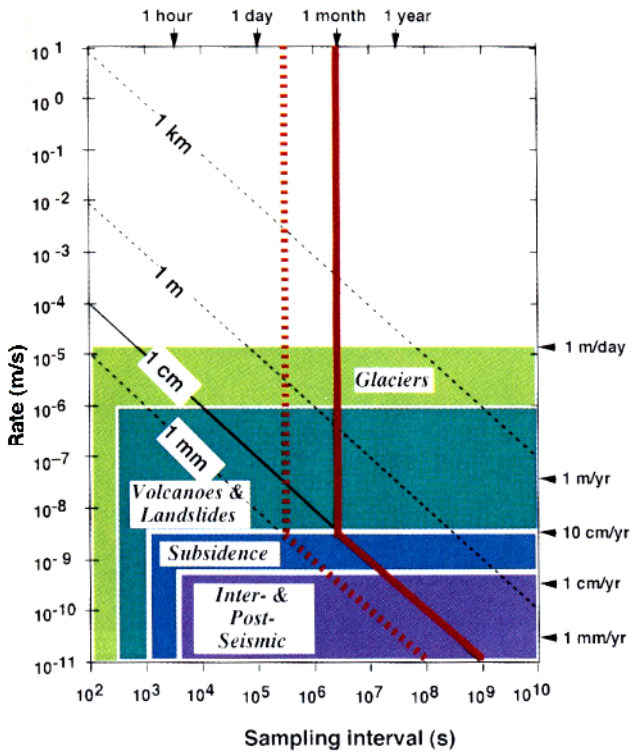

Plate 16. Classification of crustal deformation signals by rate and duration. The product of these two quantities gives the total amount of deformation in a given interval of time, shown as dashed black lines. This total in turn determines the number of fringes recorded in an interferogram composed of two radar images acquired at different times. To be detectable, a deformation signature must fall to the right of the red lines. The dashed red line shows the best case, where a satellite passes over the site every 3 days and can measure a 1-mm precision in range. The solid red line shows the typical case of a pass every 35 days and a 1-cm precision. The top right corner is restricted by the steep gradient limit, as described in section 4 and shown in Plate 17.

the vertical (relative to the horizontal) component of displacement than the JERS-1 geometry.

To remove the orbital effects, *Murakami et al*. [1996] adjust their JERS-1 fringes to fit the displacements observed by GPS at seven geodetic bench marks. This approach contrasts with that of *Massonnet et al*. [1996a], which assumes zero displacement far from the epicenter. The fringe counts between pairs of points differ by less than half a cycle between the two analyses of the same JERS-1 data.

Most of the fringes are caused by the Northridge earthquake. Near the epicenter, we count 18 fringes in Plate 19b to the SE of (360, 3790) km, but only 1 fringe in Plate 19a, implying 512 and 118 mm of range shortening observed by ERS-1 and JERS-1, respectively. The difference is a consequence of the different orientations of the two radar antennas, as described by the unit vectors $\hat{\mathbf{s}}$ parallel to their axes.

The simplest elastic dislocation model involves a single fault patch estimated by inversion of coseismic displacement vectors measured with GPS [*Hudnut et al*., 1995]. This model predicts at least one fringe (12 cm) more range change than observed by JERS-1 in the center of the uplifted lobe near the epicenter, but not

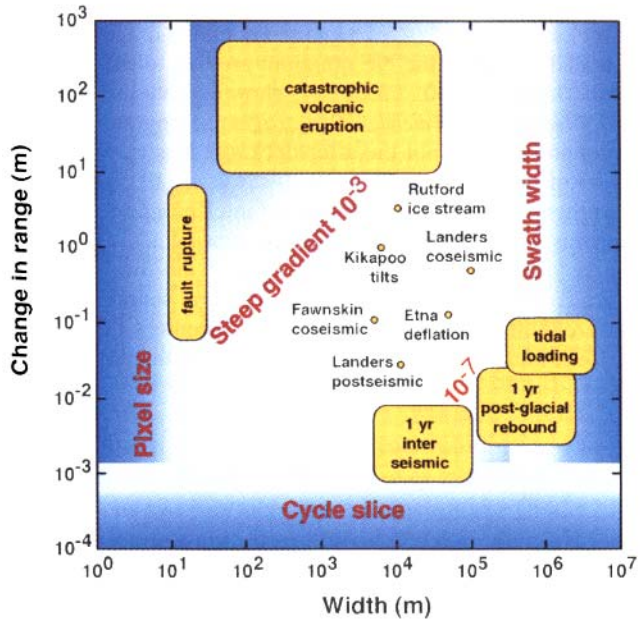

Plate 17. Classification of crustal deformation signals by width and range change. To be detected by interferometry, a signal must fall within the white irregular pentagon. Each of its sides indicates a different physical limit, as described in section 4.1.

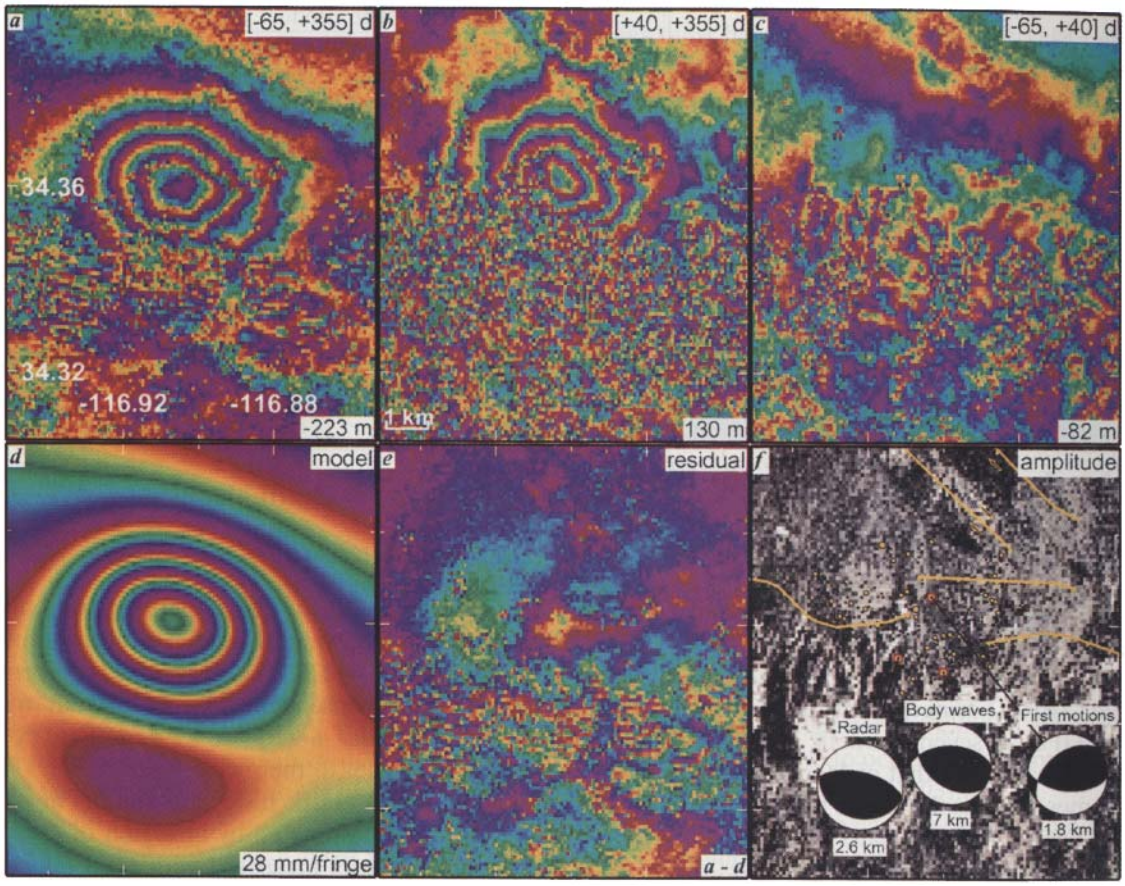

Plate 18. A magnitude 5 earthquake near Fawnskin, California, on December 4, 1992 (an aftershock following the Landers event). Temporal intervals in square brackets denote days relative to the date of the main Landers shock on June 28, 1992. The altitude of ambiguity, h_a, appears in the bottom right corner of each panel. One cycle of color denotes 28 mm of change in range. (a) Interferogram composed of images acquired by the ERS-1 satellite on April 24, 1992, and June 18, 1993, i.e., spanning the interval [−65, +355] days [*Massonnet et al*., 1994a]. The four concentric fringes in the center indicate 4×28 mm = 112 mm of range shortening due to the Fawnskin aftershock. The straight, parallel fringes in the NE quadrant are due to the Landers and Big Bear earthquakes. (b) Interferogram for the interval [+40, +355] days showing only the signature produced by the Fawnskin aftershock on day +159 [*Massonnet and Feigl*, 1995a]. (c) Interferogram for the interval [−65, +40] days showing fringes due to the mainshock but not the aftershock. (d) Modeled fringes with focal mechanism estimated by nonlinear inversion of the fringes in Plate 18a [*Feigl et al*., 1995]. (e) Residual interference pattern generated by subtracting synthetic fringes from the observed interferogram. Less than one cycle (28 mm) of unmodeled deformation remains. (f) Radar amplitude image showing active faults [*California Division of Mines and Geology*, 1992]. Three different estimates were made of the focal mechanism, epicenter, and depth: first arrivals [*Hauksson et al*., 1993], body wave inversion by grid search [*Jones and Hough*, 1994], and inversion of the radar interferogram [*Feigl et al*., 1995]. The epicenters of aftershocks recorded between June 27 and December 31, 1992, are shown with yellow dots with diameter proportional to magnitude [*Hauksson et al*., 1993].

enough range change to the northwest. To correct this shortcoming, we modify the mainshock fault parameters and add two more fault patches (Plate 19c) [*Massonnet et al*., 1996a]. The complex shapes of the fringes remaining in the residual interferograms (Plates 19e and 19f) indicate that the unmodeled coseismic slip on the fault is not a simple point source. To improve this fit further, we would have to introduce a more complicated, nonplanar fault geometry. Merely varying the distribution of slip on a single fault plane [e.g., *Wald et al*., 1996] does not suffice. Such geometric complexity, divined from attempts to fit the GPS data [*Hudnut et al*., 1995; *Shen et al*., 1996; *Wald et al*., 1996], is clear in the densely sampled map provided by interferometry. The Northridge earthquake and its aftershocks ruptured more than just the fault plane of the mainshock mechanism.

4.2.3. An extensive, shallow strike-slip mechanism. The sequence of earthquakes beginning with the magnitude 7.3 event near Landers, California, on June 28, 1992, provided an ideal test case for radar interferometry. The shallow depth of the Landers event produced spectacular surface rupture in an arid area less than 3 months after the ERS-1 satellite began acquiring radar images in a 35-day orbital cycle. With 20 fringes in the shape of a crushed butterfly, the first earthquake interferogram illustrated the coseismic deformation field with over a million pixels (Plate 20a) [*Massonnet et al*., 1993b].

The ERS-1 imaged the Landers area only once, on April 24, prior to the mainshock on June 28, 1992. Afterward, images are available for July 3 and August 7. *Massonnet et al*. [1993b] used the two-pass technique with a DEM to form two interferometric pairs: one coseismic and one postseismic. *Zebker et al*. [1994a] employed the three-pass technique.

Although the two-pass and three-pass coseismic interferograms are qualitatively similar, they are not identical. Errors in the DEM will create artifacts of ε/h_a = 30 m/90 m $\approx$ 0.3 cycles or 9 mm in range in the two-pass interferogram. For example, the east-west discontinuity at 35°N latitude in the Landers interoferogram comes from a step-like offset between two adjacent 1° by 1° quadrangles in the DEM [*Massonnet et al*., 1993b]. The three-pass interferogram, on the other hand, shows dendritic discontinuities, which *Zebker et al*. [1994a] interpret as fissuring of the ground surface. Such features do not appear in the two-pass interferogram or in the field observations. We believe they are misclosure errors where the unwrapping algorithm counts fringes incorrectly, as in the rough topography of the San Bernardino Mountains, an area where the two-pass interferogram also fails to provide a clear measurement.

Both interferograms record over 20 fringes (50 cm) of range change produced by the earthquake (Plate 20). To estimate the right-lateral offset, we count fringes along a path connecting two adjacent points on opposite sides of the fault trace. To convert the scalar change in range to the magnitude of the vector displacement, we assume that the displacement vector is horizontal and parallel to the fault. The fault offset estimated in this way agrees to within about 1 m with the field observations [*Massonnet et al*., 1993b].

We can explain the observed interferogram (Plate 20a) with an elastic model using many rectangular dislocations on a vertical fault. The modeled interference pattern (Plate 20b) closely resembles the observed pattern. The residual interferogram (Plate 20c) shows fewer than 2 fringes in most places, indicating that the model fits the data to within a few centimeters in range. The residual interferogram emphasizes any misfit in the fringe spacing or range gradient, a dimensionless quantity that measures strain. It is particularly sensitive to the distribution of slip on the fault plane at depth.

The slip distribution estimated from the radar data (Plate 21) agrees qualitatively with those estimated from GPS survey measurements of coseismic displacements [*Murray et al*., 1993; *Freymueller et al*., 1994; *Hudnut et al*., 1995], strong motion accelerations recorded in the near field [*Wolf and Wingham*, 1992; *Cohee and Beroza*, 1994; *Wald and Heaton*, 1994], seismograms in the far field [*Wald and Heaton*, 1994], and a joint inversion of all three data types [*Wald and Heaton*, 1994]. All these inversions find relatively little slip (2–3 m) below the epicenter where rupture began, but a maximum of 8–12 m of slip located at 5- to 10-km depth in the Homestead and Emerson fault segments 30–40 km north of the epicenter. The depth and magnitude of the slip maximum seems to depend on the prior information in the various inversions. All the estimates agree on the seismic moment, in accord with the centroid moment tensor and the bounds estimated from the geodetic data [*Johnson et al*., 1994].

Since seismologic data yield good estimates of the slip distribution, why estimate it from a radar interferogram? In remote areas, strong-motion seismological instruments may not exist, while the interferogram can provide true remote sensing. Second, the radar interferogram records deformation over a much longer period (several months), than the seismological record, revealing any slip that occurred before or after the mainshock rupture. Third, the interferogram records aseismic slip. Finally, accurate descriptions of the total slip distribution are useful for calculations of coseismic stress changes [*Harris and Simpson*, 1992; *Jaumé and Sykes*, 1992; *Stein et al*., 1992].

4.2.4. A normal-faulting mechanism. The Eureka Valley earthquake occurred on May 17, 1993, in a remote area of the Mojave Desert at the edge of the Basin and Range Province. The normal-faulting M_w = 6.1 mainshock and subsequent aftershocks deepened the graben in an oval-shaped coseismic deformation field of which ERS-1 radar images are the only available geodetic measurements (Plate 22). *Massonnet and Feigl* [1995b] calculate this interferogram by stacking two two-pass interferograms in a combination of three radar images (section 2.5.4). *Peltzer and Rosen* [1995] analyze

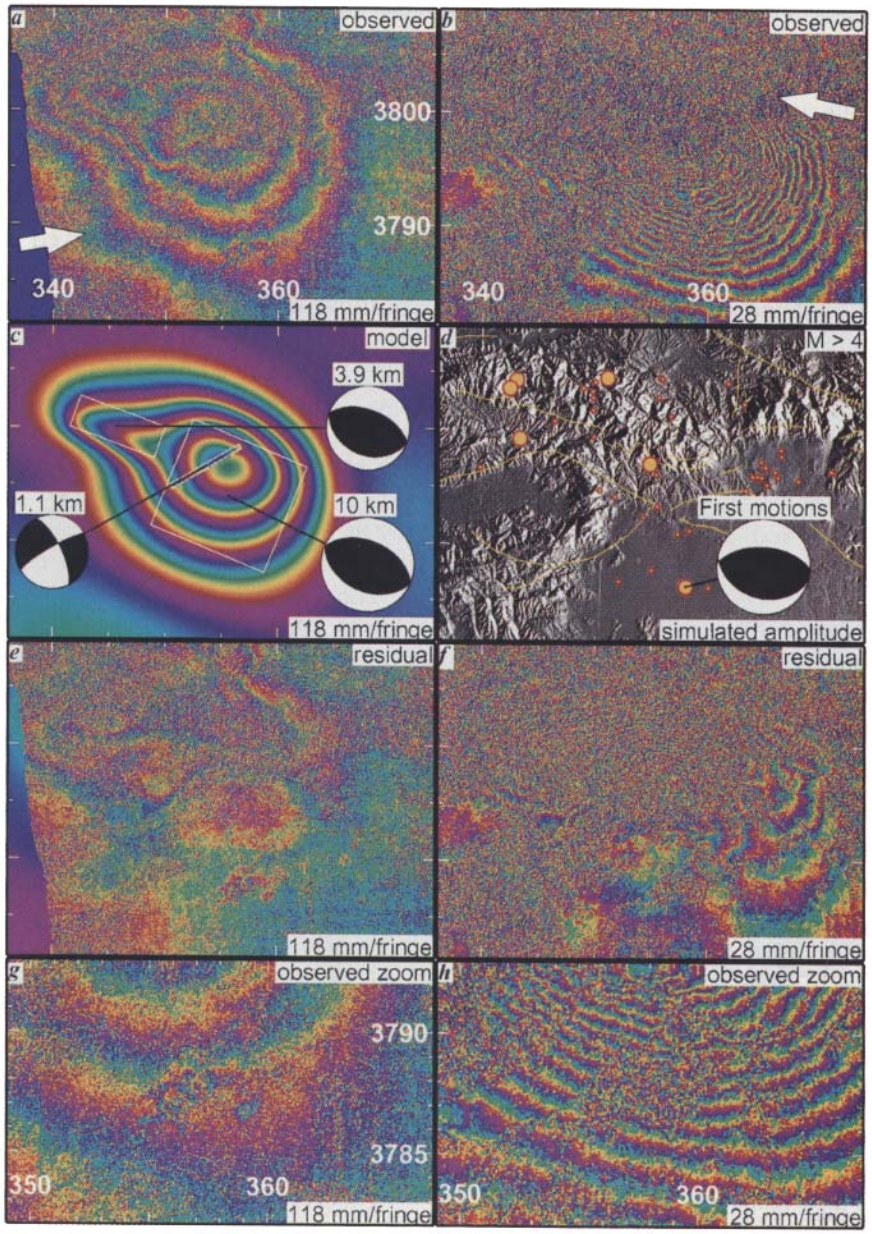

Plate 19. Northridge earthquake [*Massonnet et al*., 1996a]. Coordinates are easting and northing in kilometers in the conventional universal transverse Mercator projection [*Snyder*, 1982]. (a) Coseismic fringes observed by interferometric combination of JERS-1 images acquired April 30, 1993, and July 14, 1995. Here h_a = 52 m. JERS-1 imaged Northridge looking east with azimuth N80.2°E at an incidence angle of 38.1° from vertical as shown by the white arrow. The (east, north, up) components of the unit vector $\hat{\mathbf{s}}$ from ground to satellite are [−0.60, −0.10, +0.79]. (b) Coseismic fringes observed by interferometric combination of ERS-1 images acquired October 4, 1992, and April 5, 1995. Here h_a = 45 m. ERS-1 looked west at azimuth 281.5° at an incidence angle of 23.5° from vertical as shown by the white arrow. The (east, north, up) components of the unit vector $\hat{\mathbf{s}}$ from ground to satellite are [0.38, −0.08, 0.92]. (c) Modeled fringes calculated assuming three rectangular dislocations in an elastic half-space as well as the JERS-1 radar wavelength and geometry. White boxes indicate the surface projection of modeled faults with associated focal mechanisms and centroid depths. (d) Simulated amplitude calculated from the DEM. Mainshock focal mechanism and epicenter are shown [*Hauksson et al*., 1995]. Yellow lines are mapped Quaternary faults [*California Division of Mines and Geology*, 1992]. (e) Residual fringes showing the difference of the observed (Plate 19a) and modeled (Plate 19c) interferograms for the JERS-1 case. Several fringes remain. (f) Residual fringes showing the difference of the observed (Plate 19b) and modeled (not shown) interferograms for the ERS-1 case. The modeled fault parameters are the same as those in Plate 19c. The differences in coherence over mountainous areas may result from several phenomena. About the same amount of time elapsed between the ERS-1 and JERS-1 acquisitions; erosion may have altered the ground at C band scale but not at L band scale. ERS-1 data may also be more sensitive to changes in vegetation, which C band does not penetrate as well as L band. The most likely explanation may be the steep slopes in the mountains, to which JERS-1 is less sensitive because of its larger incidence angle. (g) Enlargment of observed JERS-1 interferogram (as in Plate 19a), where we infer compaction of the ground surface. Centered ~5 km west of the Northridge epicenter, this signature consists of two circles, each exhibiting a full closed fringe corresponding to almost 12 cm of range lengthening, as first noticed by *Murakami et al*. [1996]. The observations are compatible with subsidence caused by soil liquefaction [*Massonnet et al*., 1997]. (h) Enlargement of observed ERS-1 interferogram (as in Plate 19b) in the same area as Plate 19g.

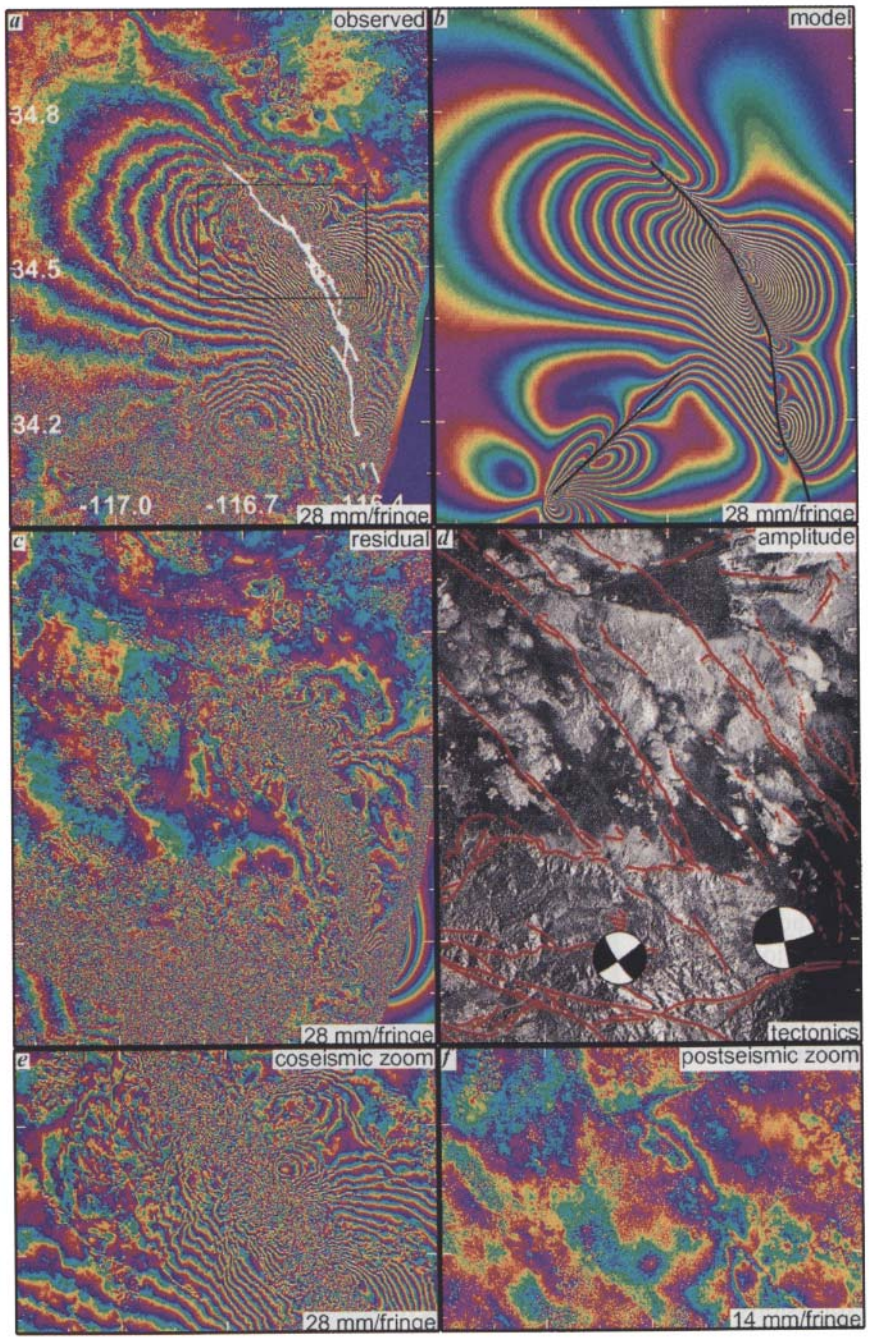

Plate 20. Landers earthquake. (a) Observed interferogram calculated from ERS-1 SAR images taken before (April 24, 1992) and after (June 18, 1993) the earthquake [*Massonnet et al*., 1994a]. Each fringe in Plates 22a, 22b, and 22c denotes 28 mm of change in range. Here, h_a is 220 m. White lines indicate coseismic surface rupture mapped in the field [*Sieh et al*., 1993]. (b) Modeled interferogram with black lines denoting fault patches included in the elastic dislocation model [*Feigl and Peltzer*, 1993; *Feigl and Massonnet*, 1995]. (c) Residual (observed minus modeled) interferogram. (d) Radar brightness (amplitude) image. The river bed near 34.9°N, 116.7°W, creates a ribbon of incoherence. In the triangular region at the junction of the Johnson Valley fault and the Kickapoo segment, the fringes are parallel and very dense, indicating a high displacement gradient. *Peltzer et al*. [1994] measured the gradient here and interpreted it as approximately 0.01° of tilt across the block caught in the stepover. (e) Enlargement of the near-fault area shown by the black box in Plate 20a. We see no organized fringes in a band within 5–10 km of the northern half of the fault trace where the gradient of deformation exceeded the interferometric limit. (f) Postearthquake interferogram (enlarged from Plate 35). The band of incoherence is not observed, and the displacement gradients are smaller.

the same three images with the three-pass technique (Plate 24). Both studies find approximately 10 cm of range increase.

To explain the observed fringe pattern, we use an elastic dislocation model to estimate the earthquake focal mechanism. The best fitting focal mechanism is a normal fault dipping 54° ± 2° to the west and striking S7°W ± 2° (Plate 22d). The 16 by 7-km rectangular fault patch centered at 9-km depth does not cut the surface. The estimated geodetic moment magnitude of 6.1 agrees with seismological estimates. The residual interferogram (Plate 22c) shows less than one 14-mm cycle in the difference between the observed (Plate 22a) and modeled (Plate 22b) fringes.

The location of the centroid estimated from the radar data is less than 6 km horizontally and 2 km vertically from the hypocenter estimated from *P* wave travel times. The modeled fault patch, however, strikes more westerly than the mapped Quaternary fault or the fault plane estimated from first motions. Indeed, *Peltzer and Rosen* [1995] find that a fault plane striking N7°E, dipping 50° west, but cutting the surface, provides a good fit to their radar interferogram on the basis of forward modeling. The fault patch estimated by *Massonnet and Feigl* [1995b] resembles the locus of aftershocks in dip, length, width, and horizontal location, but not depth.

4.2.5. How to analyze a coseismic signature in an interferogram. To clarify the preceding case studies of earthquakes captured by radar, we summarize the assumptions underlying the fault models and the procedures used to estimate their parameters. The standard model assumes a dislocation in an elastic half space bounded by the Earth's surface. By convention, we assume a Poisson rheology, such that the two Lamé moduli, λ and μ, are equal, leading to a Poisson's ratio of 1/4. Buried within this medium is a fault, which we discretize as one or more rectangular patches. To specify one such fault patch requires 10 parameters: centroid latitude ϕ, longitude λ, depth d, strike α, dip δ, along-strike length L, downdip width W, left-lateral slip U_1, updip slip U_2, and tensile slip U_3. Given the values of these parameters, we calculate the vector displacement **u** at the surface using analytic expressions [*Okada*, 1985]. Next the scalar range change follows by equation (3). A public domain computer program performs these calculations [*Feigl and Dupré*, 1998].

These assumptions define the relation between the earthquake source parameters and the data consisting of range changes measured in the radar interferogram. The goal is to find the values of parameters that best fit the data.

The simplest procedure is trial and error, usually called "forward modeling." We use our best guess for the value of each parameter to calculate a synthetic fringe pattern. With some clues about the location, geometry and magnitude of the earthquake, it is not difficult to make a simulated interferogram that looks like the observed one. By repeatedly tuning the parameters, we can usually find a model that fits the data better than our first guess. This procedure provided the first approximation to the coseismic fringes observed at Landers [*Massonnet et al*., 1993b], Eureka Valley [*Peltzer and Rosen*, 1995], Northridge [*Massonnet et al*., 1996a; *Murakami et al*., 1996], Grevena [*Meyer et al*., 1996], Aigion [*Bernard et al*., 1996], and Kobe [*Ozawa et al*., 1997].

To optimize the fit of modeled fringes to the observed ones, we can estimate the fault parameters directly from the data in an inverse problem. If we choose to estimate all 10 parameters for a single fault patch, the problem is nonlinear because the surface deformation depends strongly on the fault geometry. We use an iterative linearized least squares procedure for the Fawnskin (Plate 18) [*Feigl et al*., 1995] and Eureka Valley (Plate 22) earthquakes [*Massonnet and Feigl*, 1995b].

The second inverse problem involves estimating only the slip vector **U** on a single fault plane whose geometry is known and held fixed. This problem is simpler because it is linear. The components of the surface displacement **u** are proportional to the components of the slip vector **U**. Thus it is simple to divide the modeled fault plane into many discrete patches, as we show for Landers (Plate 21) [*Feigl and Peltzer*, 1993; *Feigl and Massonnet*, 1995]. By varying only the amount of slip on each patch but not its geometry, one can estimate the distribution of slip on the fault plane, a useful contribution to understanding of fault dynamics [*Hernandez et al*., 1997].

To use the radar interferograms as data for both types of inverse problems requires an unambiguous measurement of the range change (Figure 5, section 1.3.3) which implies unwrapping the interferogram (section 2.5.1). For Plates 18 and 21, we simply count and digitize the fringe pattern. Although tedious, this technique avoids errors because the human eye is very good at following colored fringes, even where they become noisy. It also recognizes areas where the fringes are too noisy to count. For Plate 22, a straightforward algorithm [*Tarayre*, 1994] performed well because the fringes were clear and simple.

Even unwrapped, radar range changes are still only relative measurements. To make them absolute, we must identify the fringe corresponding to zero deformation. We do this by trial and error, choosing the additive constant that produces the smallest misfit to the observed interferogram. Usually, the null fringe intersects the fault plane.

4.3. Surface Rupture by Earthquake Faulting

By definition, a mapped fault is a discontinuity separating two blocks in the Earth's topographic surface. If the fault is active, it creates a discontinuity in the differential surface, that is, the displacement field. Relative motion (slip) between the two blocks offsets the interferometric fringe pattern, except in the degenerate case where the slip vector **u** is orthogonal to the radar look vector. Surface rupture $\hat{\mathbf{s}}$ appears as a discontinuity in an interferogram just as a fault scarp appears as a discontinuity in a topographic map. Moreover, the two discon-

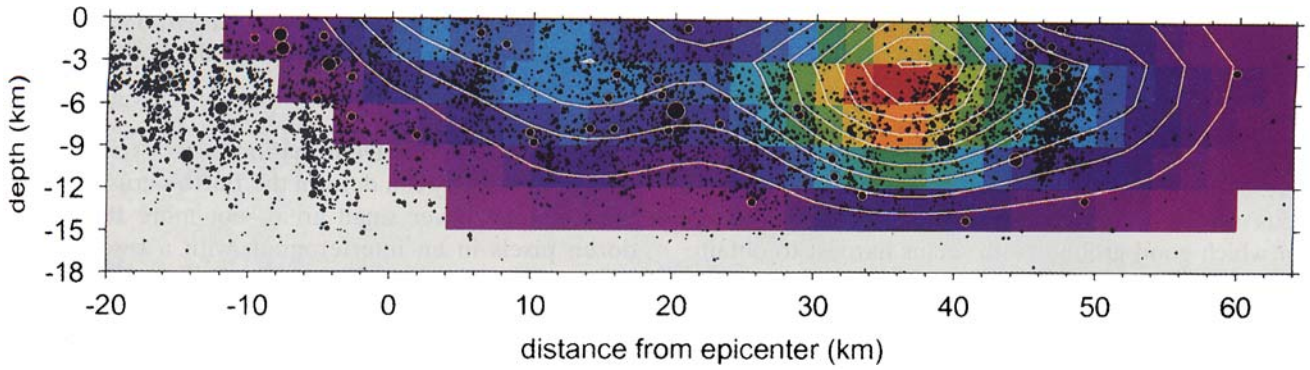

Plate 21. Estimated slip distribution for Landers in a vertical cross section with axes in kilometers northwest of the epicenter along the fault (horizontal axis) and relative to the surface (vertical axis). Warm colors denote slip up to a maximum of approximately 9 m [*Feigl and Peltzer*, 1993; *Feigl and Massonnet*, 1995]. Contour interval is 1 m. Black dots indicate aftershock hypocenters [*Hauksson et al*., 1993]. The aftershocks tend to occur outside of the areas of maximum slip, an observation with consequences for the mechanics of the earthquake source [*Scholz*, 1990; *Cohee and Beroza*, 1994].

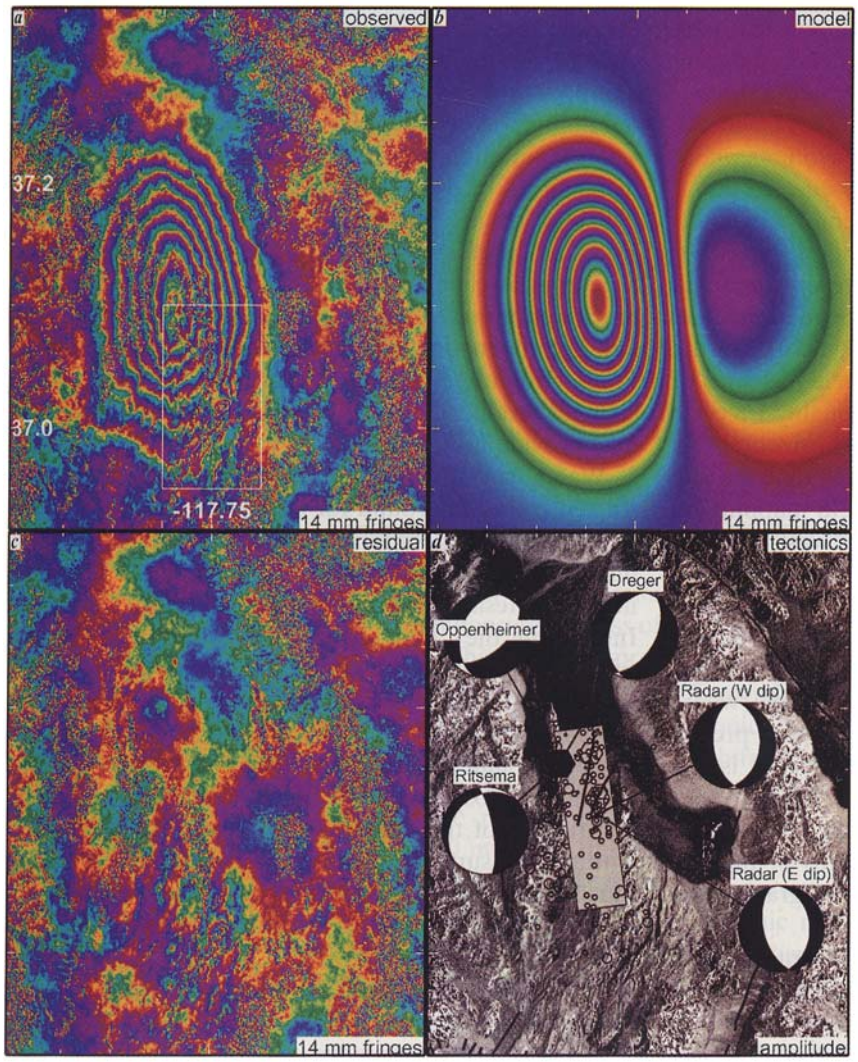

Plate 22. Interferograms showing fringes due to the Eureka Valley earthquake [*Massonnet and Feigl*, 1995b]. (a) Sum of two interferograms: one spanning the interval [−350, +175] days relative to the earthquake with h_a = 71 m and the other spanning [−175, +175] days with h_a = −98 m. Each cycle of color indicates 14 mm of coseismic range change because both intervals include the date of the earthquake. The white rectangle delimits the area enlarged in Plate 24b. (b) Modeled interferogram showing fringes calculated from the west dipping focal mechanism. (c) Residual interferogram representing the difference between the observed fringes (Figure 22a) and the model (Plate 22b). Less than one fringe (14 mm) of unmodeled range change remains. (d) Radar amplitude and tectonic map of the area covered by the interferograms, showing epicenters for reliably located earthquakes from May 17 to 31, 1993. Magnitudes range from 0 to 6.1, with hexagons marking epicenters of events with $M > 4$; the solid black hexagon marks the mainshock. Also shown are the focal mechanisms estimated from the radar data for the west dipping and east dipping planes of the May 17 mainshock, as well as a seismological estimate from first motions ("Oppenheimer"), and two different waveform inversions, with and without the records from station ANMO ("Ritsema" and "Dreger," respectively). The shaded rectangle represents the surface projection of the west dipping fault model, and black lines are Quaternary faults [*California Division of Mines and Geology*, 1992].

tinuities occur in the same location in maps of the displacement and topographic fields. Although is possible to confuse the two discontinuities if the DEM incorrectly describes the topographic expression of a fault, pairwise logic suffices to avoid misinterpretation (section 3.1). Nonetheless, small-scale disturbances or discontinuous offsets in the fringe pattern are the type of feature for which good ground truth seems hardest to obtain.

The sequence of interferograms at Landers shows that a 20-km-long segment of the Garlock fault slipped within a few weeks of the Landers main shock [*Massonnet et al*., 1994a]. The surface rupture appears as a distinct discontinuity in the coseismic interferograms spanning the date of the mainshock (Figure 10). These features are not artifacts. They are common to both coseismic interferograms. Their location and magnitude are identical, as is evidenced by their absence from the difference. These features are absent from the early postseismic interferogram.

To measure the offset, we count 1/4 ± 1/8 cycle (7 ± 4 mm) of change in range in the interferogram. Assuming horizontal slip parallel to the mapped trace of the fault, we find 19 ± 10 mm of slip, which has not yet been confirmed in the field. Triggered slip on the Garlock fault is, however, predicted by models of loading during the Landers earthquake sequence [*Harris and Simpson*, 1992; *Jaumé and Sykes*, 1992; *Stein et al*., 1992]. Indeed, we could refine such models by locating the points where the surface rupture begins and ends in the interferogram.

Plate 23 also shows several linear discontinuities offsetting the fringes in the coseismic Landers interferogram, which *Massonnet et al*. [1994a] interpret as small offsets on secondary faults like those mapped in the field [*USGS Staff*, 1992; *Padgett and Rockwell*, 1993]. On the Lenwood fault, we estimate about 1/2 cycle (14 mm) of change in range with an uncertainty of roughly 1/8 cycle (4 mm). Assuming the slip to be purely horizontal and parallel to the trace of the fault, we infer that the slip reaches a maximum of 51 ± 13 mm. Field mapping on July 1 showed a separation of 45–50 mm west of Soggy Lake (G. Fuis, USGS, unpublished map, 1992). Although the field and radar observations agree on the maximum offset on this fault segment, they do not agree exactly on where it occurred. The interferogram shows most of the slip some 10 km north of Soggy Lake, where Fuis did not map. Although this is the most precise ground truth we have for ruptured fringes, it is not entirely satisfactory.

The date of faulting observed in Figure 10 and Plate 23 must fall between the acquisition dates of the two images used for the first coseismic interferogram: April 24 and August 7, 1992.

Price and Sandwell [1998] take the gradient of Landers interferograms to reveal other small-scale features. The difficulty of interpreting torn fringes as surface rupture also appears for the Eureka Valley earthquake. Here the two radar interferometric studies disagree on whether coseismic rupture reached the surface [*Massonnet and Feigl*, 1995b; *Peltzer and Rosen*, 1995], but a small, shallow aftershock can explain all the observations (Plate 24).

4.4. Anthropogenic Deformation

Human activity can deform the Earth's crust. Most of the examples cover small areas, not more than a few dozen pixels in an interferogram with a resolution of ~20 m. They can produce range changes of a few centimeters in less than a year.

An interesting checkerboard pattern appears in Plate 6. The phase changed by up to 0.3 cycles (3 cm in range) on agricultural fields watered by irrigation canals in the time between the radar images [*Gabriel et al*., 1989]. Natural watering by rainfall can also produce the same checkerboard pattern, as seen elsewhere in the Imperial Valley (Plate 25) and in the Ukraine [*Massonnet,* 1993].

The watering caused the phase change, but by what mechanism? One possibility is that the water modified the dielectric characteristics of the soil to raise the reflective centroid ("phase center") of the radar pixel, shortening the range without actually moving the dirt. The second possibility, favored by *Gabriel et al*. [1989], is that the clay in the soil absorbed the irrigation water, increasing its volume like a sponge and physically raising its upper surface. This ambiguity will continue to limit our ability to interpret radar interferograms, particularly when the motion is small. We could distinguish the two mechanisms by using two different radar wavelengths. A dielectric change would change the phase by the same fraction of a cycle regardless of the wavelength, whereas a geometric change would not. Otherwise, we need a much better understanding of radar scattering by rough and heterogeneous geological surfaces [*Beaudoin et al*., 1990]. Empirical measurements of microwave phase changes produced by wetting soils in anechoic chambers may provide useful clues.

Water can also produce subsidence where it is extracted from the ground for agricultural irrigation, civil engineering, or geothermal energy. Plate 25 shows as much as 90 mm of subsidence during a period of 2 years near the Mesa geothermal plant in southern California. Integrating the range change over the area of the oval fringes, *Massonnet et al*. [1997] estimate net total volume loss to be roughly 4.0×10^6 m^3 in good agreement with the value of 5.0×10^6 m^3 recorded in the pump log. Since the plant reinjects the water into the ground after cooling, the loss of volume might also be due to thermal contraction of the soil. The radar measurements agree with ground surveys to within about 2 mm but provide a much better overall map of the ground deformation. *Amelung et al*. [1998] also observe subsidence near Las Vegas.

Subsidence as a result of mining can also produce fringes in an interferogram, as *Carnec et al*. [1996] show in a study of the Gardanne mine in southeast France. Here, noticeable subsidence has occurred since the 1960s, when mechanical coal extraction began. As the

Figure 10. An interferogram showing surface rupture on the Garlock fault in California, as well as some artifactual residuals. The surface rupture appears in all the coseismic interferograms of Landers. It represents 7 ± 4 mm of range change, projected as 19 ± 10 mm on the ground, assuming pure horizontal displacement. Data from *Massonnet et al*. [1994a] as described in the caption for Plate 20a. One complete cycle of shading (from solid black to solid white) corresponds to 28 mm of range change.

cavities collapse, the ground surface some 1000 m above subsides gradually without apparent rupture. The mostly vertical displacement is amplified by the structure of the sedimentary basin and can be triggered by local seismicity. Waste rock is used to partially compensate the loss of volume behind the extraction front. This does not prevent subsidence, which reaches a maximum of 42 mm as observed in an interferogram spanning 35 days. The deformation was also recorded by two separate leveling lines covering the same period of time. The rms scatter in vertical displacement between the radar measurements and the two leveling lines is 10 mm and 16 mm. The interferometric study adds to existing surveys by precisely mapping the spatial extent of the subsidence. These demonstrations open wide prospects for industrial and environmental applications with both economic and legal consequences.

4.5 Glaciers

Flowing ice creates spectacular fringe patterns in interferograms because its movement can be quite rapid, sometimes reaching velocities of the order of 1 m d^{-1}. Capturing such rapid motion by satellite radar interferometry requires short orbital and temporal separations between successive passes. The ERS-1 satellite met both requirements in its "commissioning" and two "ice" phases, December 28, 1991, through March 3, 1992, and December 24, 1993, through April 10, 1994, when it would pass over a given area every 3 days. Since its orbital trajectories tend to cross near the poles, ERS-1 produced many pairs of images with small orbital separations of ice-covered areas at high latitudes. These favorable conditions led to a number of studies using interferometric maps of ice flow to refine quantitative dynamic models [*Goldstein et al*., 1993; *Joughin et al*., 1996; *Rignot*, 1998; *Showstack*, 1997; *Jonsson et al*., 1998; *Kwok et al*., 1998]. For a review, see *Bindschadler* [1998].

4.5.1. An ice stream. As it flows out to sea, the Antarctic ice sheet shown in Plate 26, produces over a hundred interferometric fringes, indicating several meters of differential range change [*Goldstein et al*.,

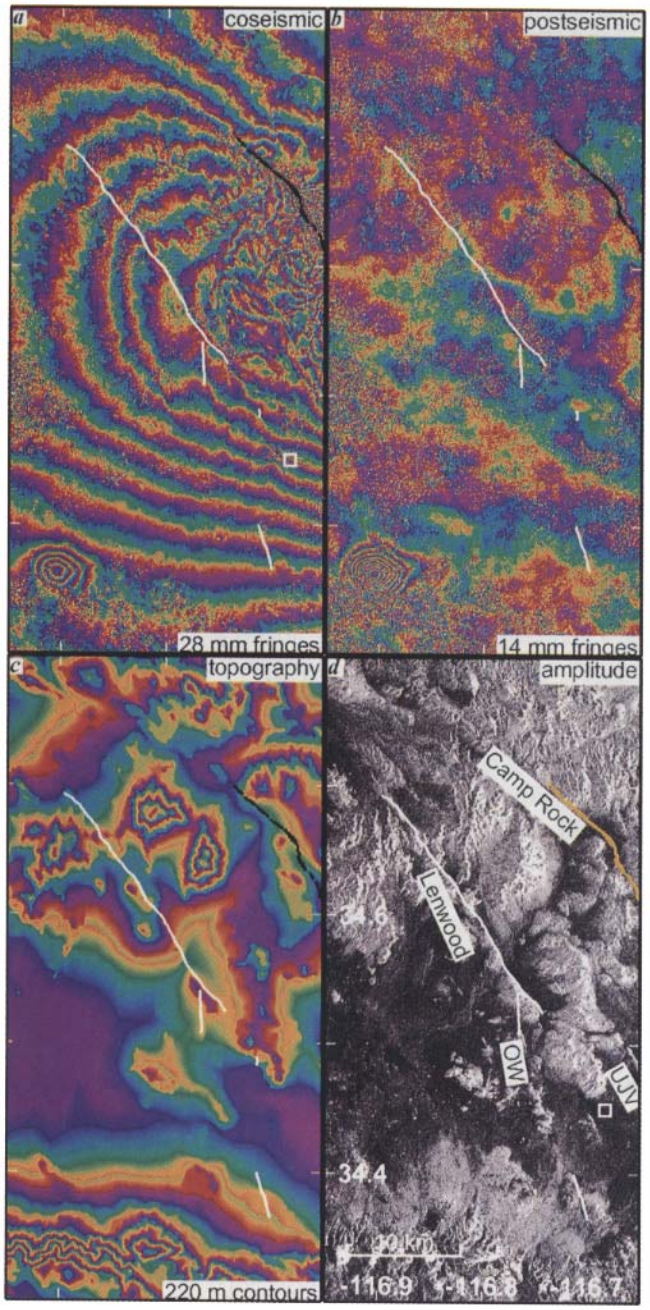

Plate 23. Detail of area where several faults ruptured sympathetically with the Landers earthquake. The white line segments denote discontinuities in the fringe pattern, which we interpret as surface rupture on the Lenwood, Old Woman (OW), and possibly Upper Johnson Valley (UJV) faults. Black segments denote surface rupture as mapped in the field [*Sieh et al*., 1993]. (a) Coseismic interferogram from ERS-1 images acquired April 24, 1992, and June 18, 1993, which thus records deformation in the interval [−65, +355] days relative to the Landers mainshock of June 28, 1992 [*Massonnet et al*., 1994a]. One fringe represents 28 mm of change in range. The offset in the magnitude of the displacement vector $\Delta|\mathbf{u}|$ is estimated by assuming purely horizontal, right-lateral strike-slip displacement on the local trend of the fault. It reaches a maximum of about 51 ± 13 mm near the center of the figure. The value of h_a is 220 m. The square shows the location of Soggy Lake. (b) Postseismic interferogram as spanning the interval [+5, +1008] days after the mainshock [*Massonnet et al*., 1996b]. No offsets in the fringe pattern are visible across the fault traces identified in Plate 23a, indicating that the sympathetic slip was coseismic, that is, within 5 days after the June 28 mainshock. Each fringe represents 14 mm of range change because this interferogram is the combination of two others, as described in the caption for Plate 37. The altitude of ambiguity h_a is over 16,000 m. (c) Topography shown as the DEM with a 220-m contour interval, chosen to equal h_a for Plate 23a. This display demonstrates that the discontinuities in the coseismic interferogram (Plate 23a) are not due to errors in the DEM. (d) Amplitude image. The closed fringes in the lower left corner of Plates 23a and 23b are due to a magnitude 5 aftershock, as described in section 4.2.1 and shown in Plate 18.

1993]. The spectacularly clear pattern in the Rutford Ice Stream is straightforward to interpret for two reasons. First, the short time (6 days) between the two radar images minimizes any phase changes due to alteration of the reflective ice surface by freeze, thaw, or precipitation. Second, the exceptionally high value of h_a eliminates the need for a topographic correction.

The interpretation, sketched in Plate 26b, is simple and clear [*Goldstein et al*., 1993, pp. 1525–1526]:

> "The fringe pattern contains the combined effects of ice flow motion and tidal action. . . . In the ice stream north of the grounding line, the ice is grounded and tidal action is absent. . . . The velocity north of the grounding line is high and only slightly varying over a 22-km wide central band of broad fringes, dropping off abruptly and rapidly into the marginal shear zones, where the fringes become very narrow and in large part unresolved. The steep velocity gradient ends rather abruptly at the outer edge of the marginal shear zones, where the fringes become broad again. This flow pattern agrees with that found by ground-based measurements. . . ."

To obtain quantitative results, *Goldstein et al*. [1993] count a net total of 94 fringes between a reference point at on bedrock in the Flowers Hills, outside the ice stream, and a second point in the middle of the grounded part of the ice stream. To convert this relative (scalar) range change into a (vector) velocity, they assume that the ice velocity vector is horizontal and that its azimuth is parallel to the margins of the stream. The usual formula (3) implies that each fringe represents a displacement of 68 mm over the 6 days between images, or an average velocity of 11 mm d^{-1}. The grounded ice in the middle of the ice stream is thus flowing at 1.1 m d^{-1}, corresponding to an annual rate of 390 m yr^{-1}. Counting fringes along a profile in the middle of the ice

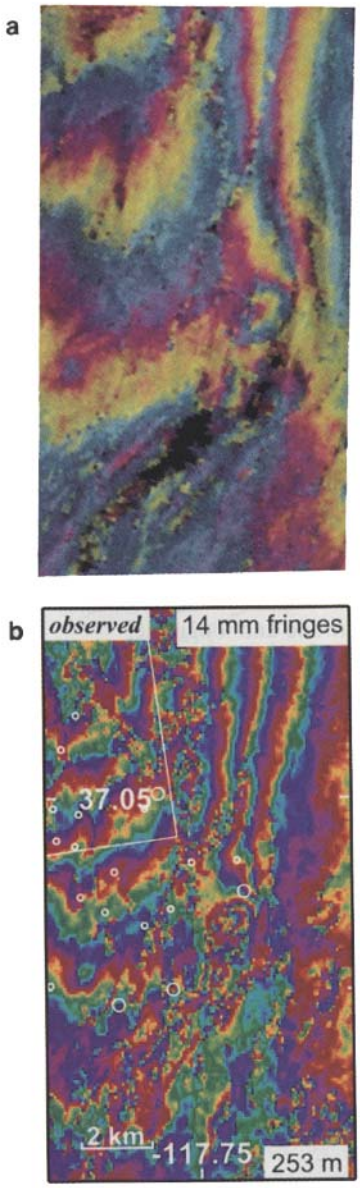

Plate 24. Comparison of two interferograms for the Eureka Valley earthquake. *Peltzer and Rosen* [1995] observe surface rupture in their three-pass interferogram (Plate 24a), in which one fringe denotes 28 mm of range change. *Massonnet and Feigl* [1995b] stacked two interferograms, each calculated with the two-pass DEM elimination technique without unwrapping (Plate 24b), so that each fringe represents 14 mm of range change, as in Plate 22a. The circles in Plate 24b mark the epicenters of all earthquakes in the area with magnitude of >3 and depth of <5 km (D. Oppenheimer, personal communication, 1994). The white angle in the upper left corner of Plate 24b denotes the surface projection of the one-patch fault model, as in Plate 22. The areas covered by Plates 24a and 24b are only approximately equivalent, because their geometric representations are different. *Peltzer and Rosen* [1995] observe an offset of ~3 cm in their interferogram, while we see no such discontinuity longer than 1 km in ours [*Massonnet and Feigl*, 1995b]. The fault models also disagree. Peltzer and Rosen favor a variable slip (multipatch) fault model in which the uppermost fault patches cut the surface, while our optimized one-patch model stops some 6 km short of the surface. Furthermore, they observed a fault scarp with 1–3 cm of vertical displacement which they could follow in the field for a few tens of meters. Any surface rupture would have to be small, both in magnitude and spatial extent, to avoid cutting the fringes observed in our interferogram. A small, shallow aftershock can explain all the observations and resolve the controversy. Some 3 cm of slip on a 1-km^2 fault represents an earthquake of magnitude 4. An earthquake of approximately this magnitude (M_L = 3.5) occurred at 0.02-km depth in this area. This location is also <1 km from the offset observed by Peltzer and Rosen, well within the uncertainties of the seismological estimates. Such an earthquake could have produced the short scarp they observed in the field. It could also produce concentric fringes 1–2 km in diameter in the interferogram. Two such fringes (28 mm of range) are barely discernible in a magnified view of our interferogram (Plate 24b). Plate 24b was provided courtesy of JPL.

stream (long-dashed line in Plate 26b), the authors find velocities that agree with measurements made on the ground a decade earlier to within 10 m yr^{-1}. The interferogram also locates the grounding line, where the ice loses contact with its rocky bed and begins to float and accelerate. Downstream of the grounding line, the fringe count indicates that about 2 m of vertical displacement occurred in the 6 days between the two radar images, in good agreement with the tidal rise of 2.1 ± 0.2 m calculated from empirical Fourier components. The shape of the tidal uplift profile measured by the interferogram indicates that the ice shelf flexes upward as it floats.

4.5.2. Greenland ice sheet. *Rignot et al*. [1995] and *Joughin et al*. [1995] observe ice flowing in Greenland using ERS-1 radar images acquired at 3-day intervals in 1991 and 1992, highlighting the complex coupling between the flow and topographic fields. These studies interpret interferometric fringe patterns and calibrate radar measurements of ice velocity. *Kwok and Fahnestock* [1996] present the details of the radar techniques used on ice sheets. Plate 27 presents a spectacular example [*Dammert and Hagberg*, 1994].

The first two studies confirm *Goldstein*'s [1993] observation that ice can remain sufficiently coherent over 3 or 6 days to produce clear fringes. Furthermore, *Rignot et al*. [1995] review the scattering characteristics of percolation facies, dry snow, and soaked snow to argue that the interferometric fringe patterns are more related to the volume properties of the firn than the ice sheet surface. By comparing two separate interferograms taken 22 months apart, *Joughin et al*. [1995] demonstrate the temporal and spatial stability of the fringe patterns on the Greenland ice sheet. Both studies use a DEM derived from radar altimetry which is sufficiently precise ($\varepsilon/h_a \sim 1/2$) but quite coarse (2 km between samples). As a result, some of the short-scale fringes represent topography, not flow.

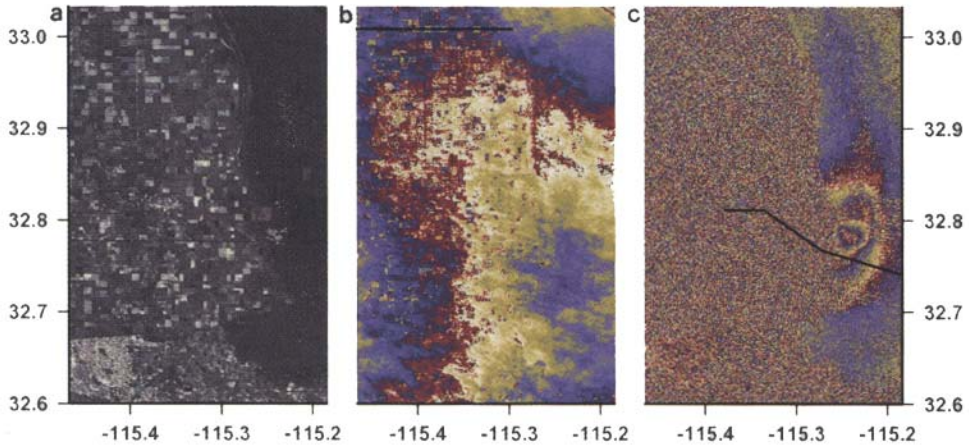

Plate 25. Interferogram subsidence created by groundwater pumping in the Imperial Valley, California. (a) ERS-1 amplitude image of the area, near the U.S.-Mexican border and the city of Mexicali. The area is half covered by agricultural field. (b) An interferogram spanning 6 days and showing coherent fields with surface phase changes, similar to Plate 6, but in C band. (c) An interferogram spanning 2 years, showing incoherent plowed fields. Three fringes, or 9 cm of subsidence, are caused by the activity of the Mesa geothermal plant located here [*Massonnet et al*., 1997]. Axes are labeled in degrees of latitude and longitude.

Concentric fringes in the interferogram, called "bull's eyes" by *Joughin et al*. [1995], are typically a few kilometers in diameter and usually appear in pairs. They form as ice flows up and over a bump in the bed, according to a simple model proposed by *Rignot et al*. [1995]. By assuming that the displacement vector remains parallel to the ice surface, this model produces a fringe pattern similar to the observed interferogram (Plate 28). The line connecting the centers of the concentric circular fringes gives the flow direction, and the distance between the centers is approximately equal to half the width of the bump. Finally, the phase difference between the center of a circle and the average phase in the surrounding area is related to the height of the bump. Using this model, the two Greenland studies infer the azimuth of the ice flow vector, one of the two angles needed to convert the scalar change in distance to vector velocity by equation (3). The second angle is the difference in elevation (above local horizontal) between the ice flow and the satellite radar antenna axis. To determine it, both *Rignot et al*. [1995] and *Joughin et al*. [1995] assume that ice flows downhill parallel to its surface.

Rignot et al. [1995] compare their velocity estimates to stake surveys along a 40-km profile during a 300-day period in 1991–1992 including the 3-day interval spanned by the interferogram. The two techniques both give values of approximately 25 cm d^{-1} for the horizontal component of ice velocity. The discrepancies between the two profiles are generally smaller than the uncertainties of 2.5 cm d^{-1} for the radar estimates and 2 cm d^{-1} for the stake survey. The former includes a $\pm 4°$ uncertainty in the flow azimuth. Although the radar estimates are within 6% of the survey values for the profile as a whole, the difference reaches 15% in the southern part of the profile. Arguing that such a discrepancy is too large to explain by orientation alone, *Rignot et al*. [1995] suggest the possibility of a ~10-cm change in snow thickness between the two radar images. To be perceptible to the radar, such a change in thickness implies a change in the snow's refractive index without a corresponding change in its microwave-scattering properties. If the latter had changed substantially, the interferogram would lose coherence.

Joughin et al. [1995] also estimate an ice velocity profile by counting fringes along a path parallel to the ice flow. Then they compare their values to a model calculation. The model imposes continuous flow by assuming constant flux at all points along the profile and in the plane of the profile. Furthermore, it assumes a horizontal bed at sea level and all of the ice motion at the bed. Then the flux Q per unit width at a point is the product of the velocity V and the surface elevation H, such that $Q = VH$. They measured the topographic profile H with an airborne laser altimeter. Using all these assumptions, *Joughin et al*. [1995] calculate range changes that fit the radar observations to within a cycle (28 mm in range) along the profile, thereby estimating ice flux Q and velocity V.

4.5.3. Spitsbergen. We have applied radar interferometry to 12 scenes acquired by ERS-1 over western Spitsbergen during summer and autumn 1991. Few of the summer scenes form useful interferometric pairs because the surface of the glaciers is very dark, owing possibly to surface melting. The early autumn ice, on the other hand, is highly reflective, allowing a good signal-to-noise ratio over the glaciers. Among the scenes acquired in this period, several pairs possess suitable orbital trajectories, leading to good interferometric fringe patterns. The comparison between these fringe patterns and a previous DEM provides a map of the ice motion in the 9 days between the images with an accuracy of ~1 cm (Plate 29). It is therefore possible to map the displacement over the entire glacier network if coherence lasts 24 days (RADARSAT) or 35 days (ERS).

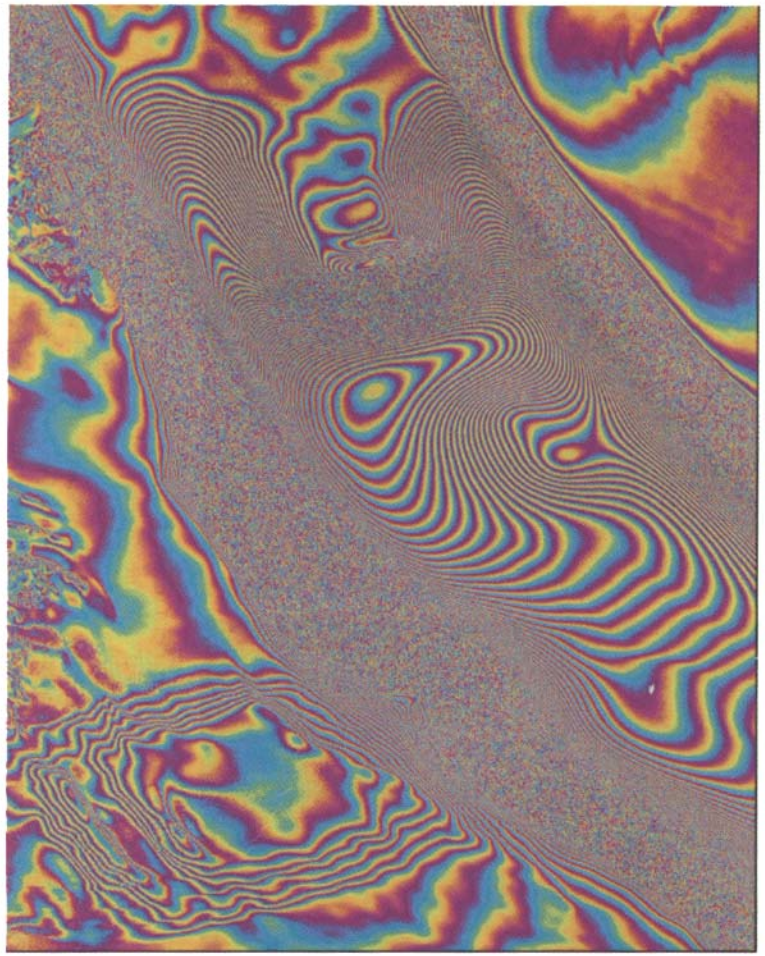

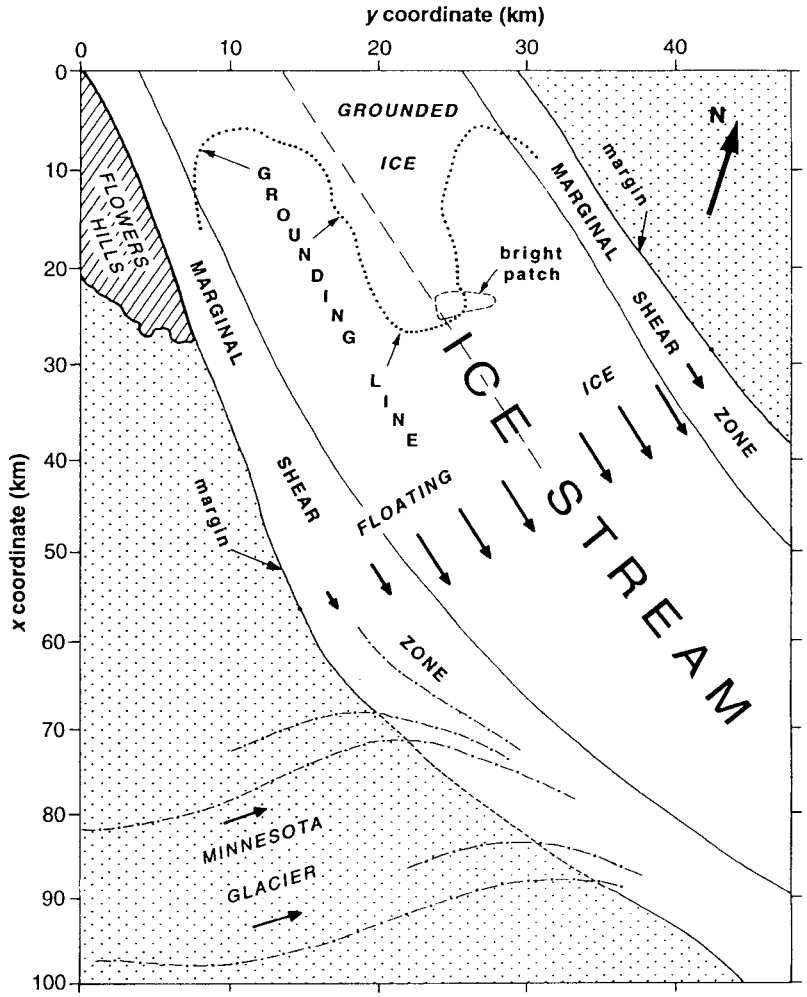

Plate 26. (left) Interferogram showing glacier ice flowing at ~1 m d^{-1} in Rutford Ice Stream, Antarctica, from *Goldstein et al.* [1993]. The center of the image is at 78°43′S, 83°0′W. The radar line-of-sight azimuth (350.8°T) is up. Each cycle of color represents 28 mm of range change. (right) Location map for features in the interferogram at left. Ice flow is indicated schematically by arrows. The grounding line is shown dotted. Upstream from this line, the ice is grounded; downstream, it is afloat. Dash-dot lines show flow traces, faintly visible in the interferogram. The accelerating zone appears as dense fringes south of "bright patch." Goldstein et al. attribute the high velocities to the ocean tides acting on the floating ice. The fringe count indicates that about 2 m of vertical displacement occurred in the 6 days between the two radar images, assuming that the horizontal contribution is given by the ground-based velocity measurements. A tidal rise of 2.1 ± 0.2 m is calculated from empirical Fourier components of the tide observed near Rutford Ice Stream. The shape of the tidal uplift profile measured by the interferogram indicates that the ice shelf flexes upward as it floats. A model describing the flexure as a bending elastic beam provides a good fit to the radar data along the 10 km where the uplift profile is steepest. Reprinted with permission from *Goldstein et al.* [1993]. Copyright 1993 American Association for the Advancement of Science.

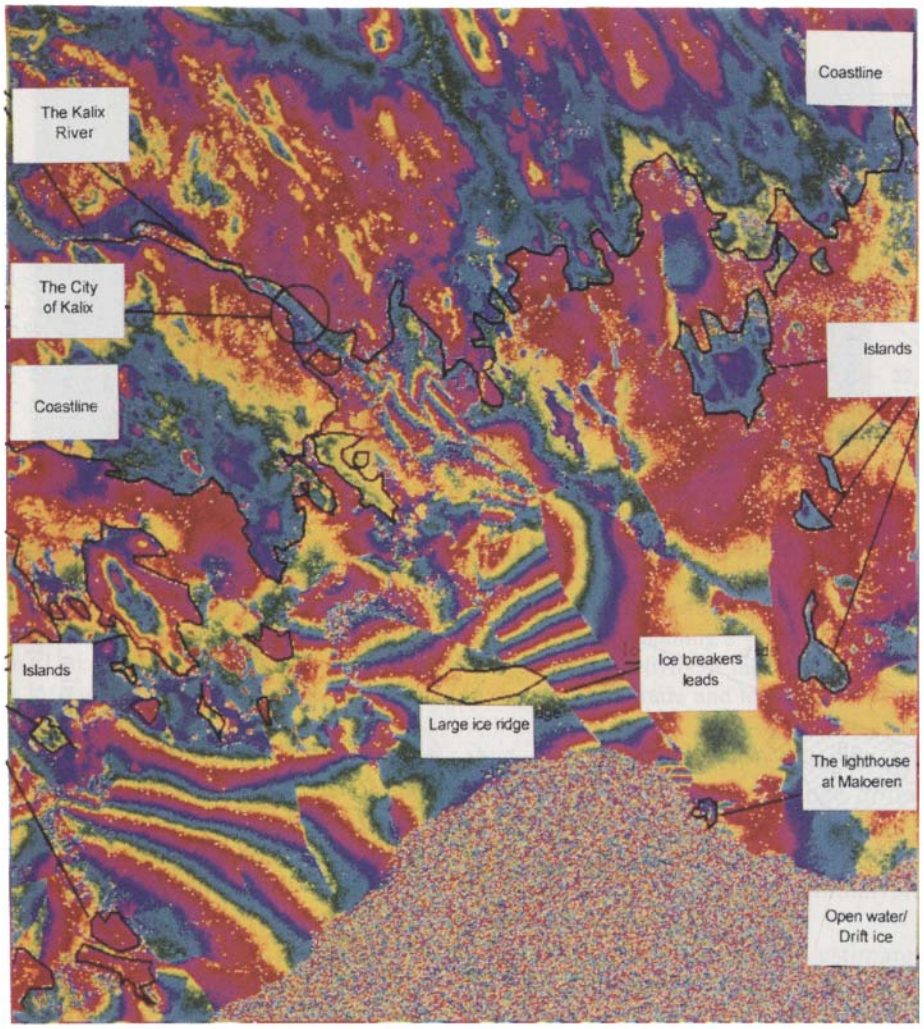

Plate 27. An ice sheet floating in the Baltic sea (Gulf of Bothnia), showing complex offsets related to breaks [*Dammert and Hagberg*, 1994] (ERS-1 data). The incoherent area corresponding to open water has not been masked. Each fringe represents 28 mm of range change.

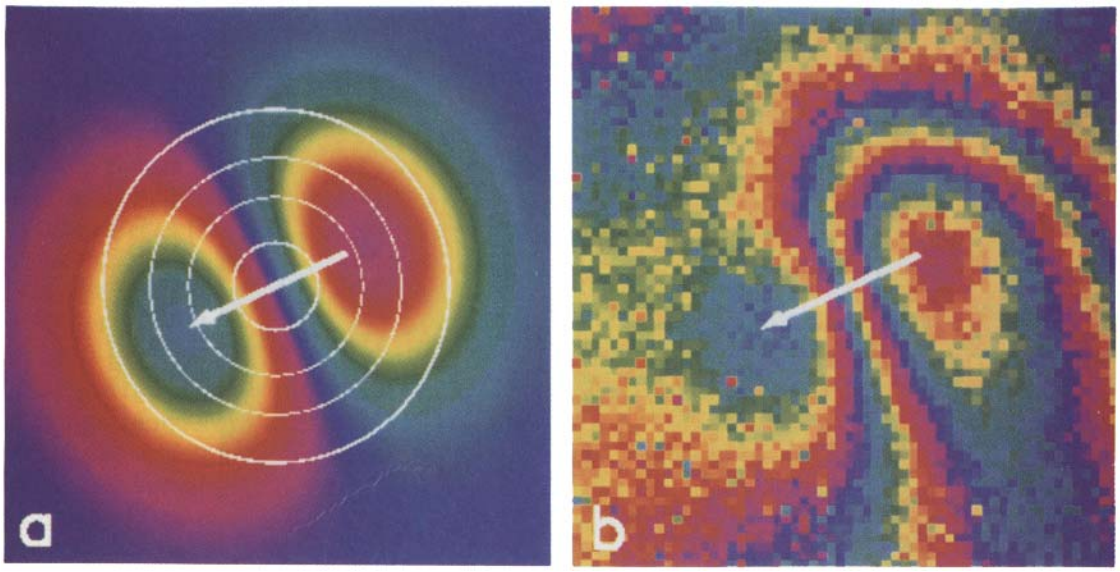

Plate 28. (a) Modeled interferometric fringe pattern for ice flowing over a bump. Contour lines (20 m) are shown as white lines. The flow velocity is 30 cm d^{-1} in the direction of the arrow. The bump is of Gaussian shape, and the ice flow is assumed parallel to the surface. (b) Fringe patterns in a square 4.8 km on a side observed in an interferogram calculated from ERS-1 images of ice flowing over a bump, acquired over the Greenland ice sheet on November 25 and 28, 1991. One cycle of color indicates 28 mm in range change. From *Rignot et al*. [1995].

Plate 29. (left) Complex flow of several glaciers in Spitsbergen as observed by ERS-1 in interferometric phase change over 3 days. One cycle of color represents 28 mm in range change. (right) Amplitude image of same area.

4.6. Landslides

A landslide in the southern French Alps provides a test case for radar interferometry during the 3-day orbital cycle of ERS-1 in August 1991. Using many different pairs, several groups find NW-SE trending fringes, indicating a downhill movement with a gradient (Plate 30). The motion decreases towards the bottom of the slide, in agreement with ground-based measurements [*Folacci et al*., 1988]. *Fruneau et al*. [1996] develop a model of translational sliding that includes a change in velocity gradient from 5×10^{-5} d^{-1} in the upper (NW) part of the slide to 1.6×10^{-5} d^{-1} in the SE.

Scaling this model for the different time intervals accounts for all the observed interferograms, suggesting that the motion is steady. Furthermore, the preferred model includes structural discontinuities, suggesting that such features play an important role in the mechanics of the landslide. *Carnec et al*. [1996] find an rms difference of 10 mm between profiles obtained from interferometry and from ground surveys.

Other landslides may be more difficult to study by radar than this example. Landslides require an accurate DEM because they occur in areas of rough topography. Unless they slide as a single slab, landslides usually degrade the ground surface quickly, eliminating interferometric coherence. Finally, landslides can deform the ground in excess of the high gradient limit.

4.7. Volcanoes

The interferometric technique is well suited for surveying active volcanoes using existing satellites. The typical deformation rate of several centimeters per month is easy to measure with monthly passes. Over such short times, temporal decorrelation by vegetative or climatic changes is not a major concern. For example, several ERS-1 and JERS-1 radar images of Merapi in Indonesia remain coherent over a month despite heavy vegetation in a humid tropical region. On the other hand, interferograms over Kilauea in Hawaii seem to show an atmospheric signature larger than the deformation signal over a 6-month period [*Rosen et al*., 1996] despite GPS survey measurements of rapid movement in the preceding years [*Owen et al*., 1995]. Coherence also lasts over 3 years at La Palma, another tropical volcano [*Klees and Massonnet*, 1998]. In Arctic regions, preliminary interferograms in Katmai show acceptable coherence from one summer to the next but break down on freshly erupted lava [*Lu et al*., 1997]. Near Yellowstone, *Wicks et al*. also found good coherence. In this section, we show examples for Mount Etna and Long Valley.

4.7.1. Deflation of Mount Etna. The volcano at Mount Etna in Italy is one of the most active in the world, and the first to be studied by radar interferometry [*Massonnet et al*., 1995a; *Briole et al*., 1997; *Lanari et al*., 1998; *Williams and Wadge*, 1998]. The most recent eruption began in late 1991 in the Valle del Bove, a large collapse amphitheater on the eastern flank, following a fracture system that opened in 1989. The lava covered most of the southern part of Valle del Bove. The eruption stopped on March 31, 1993, after 473 days. The production of lava remained stable during most of the eruption, and the total volume was about 0.3 km^3 [*Villari*, 1994].

Since the ERS-1 satellite began acquiring radar images during the eruption, it captured all but the initial 5 months of the eruption in a series of revealing interfero-

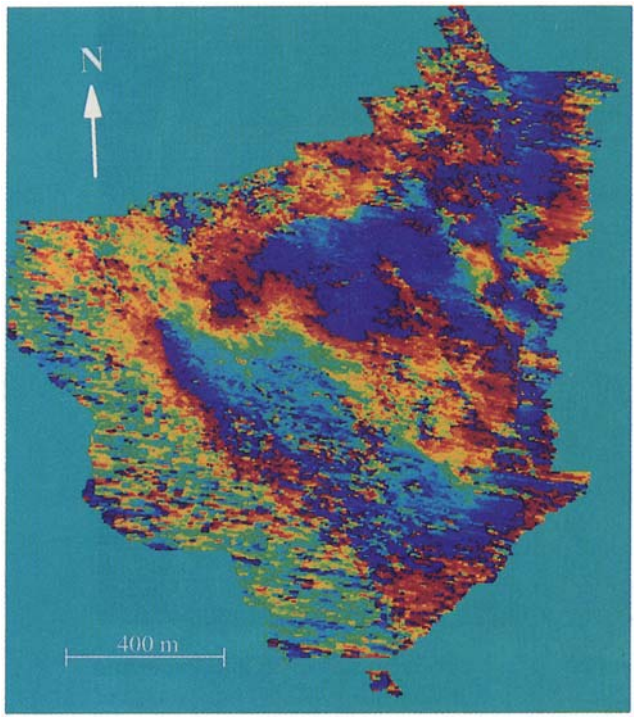

Plate 30. Interferogram of the La Clapière landslide spanning August 23–26, 1991. One fringe denotes 28 mm of change in range. Reprinted from *Fruneau et al*. [1996] with permission of Elsevier Science.

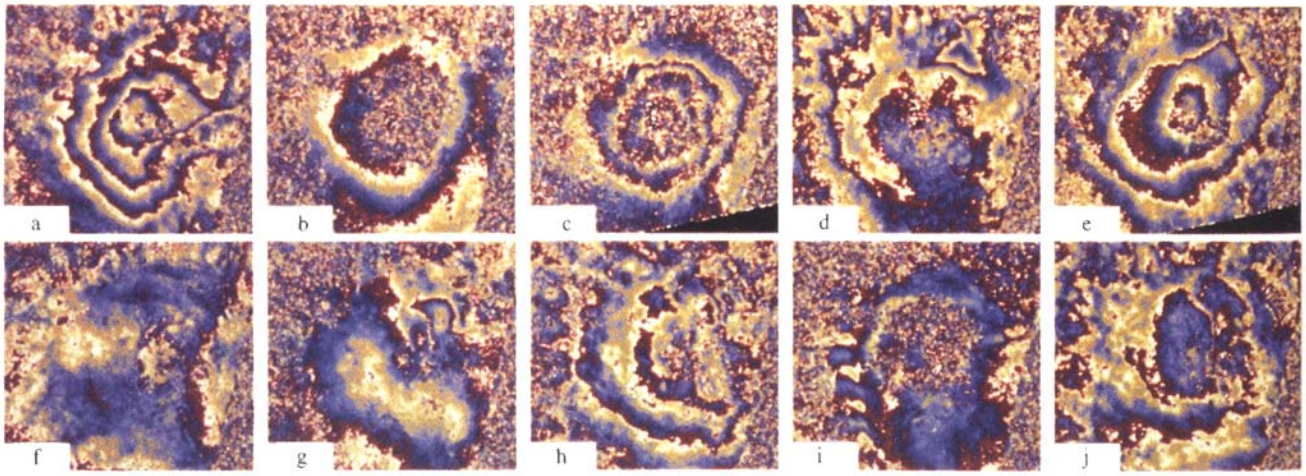

Plate 31. Various Etna fringes. The top row of interferograms are from ascending orbits, and the bottom row are from descending orbits. Plates 31a to 31c show the subsidence of the volcano at different stages. Plate 31f (35 days separation, starting 3 months after the end of the eruption) shows good coherence and not a single fringe despite a relatively small altitude of ambiguity (51 m). It was used to assess the quality of the digital elevation model and thus to calibrate the maximum expected topographic residual on the other interferograms. The triangular feature in Plates 31d and 31e is related to the ascending orbit of November 1, 1992, and is equivalent to a positive displacement of 3 cm. It does not appear in Plate 31c and is thus produced by a reversible source. Nor does it appear in Plate 31j, composed of images taken on October 4 and November 8, 1992. The most likely cause is thus an ionospheric propagation heterogeneity. Examples of tropospheric heterogeneities appear in Plates 31h (semicircular feature different from a closed fringe) and 31i (chained clouds on the left side).

grams (Plates 31–33). The best ascending interferogram (Plate 33a) shows four concentric fringes suggesting ~11 cm of deflation across the whole volcano in 385 days. The same amount of subsidence appears in the descending interferogram for essentially the same time interval but from a geometrically different point of view (Plate 33c). The fringes cannot be artifacts from atmospheric heterogeneities because the ascending and descending interferograms involve two completely independent image pairs.

Different amounts of subsidence appear for different time intervals (Plates 31a, 31e, and 31h). However, deflation does not appear in the interferograms composed of images acquired after the end of the eruption, such as Plate 31. Here the range change is essentially constant over the area that remains coherent. The coherence is poor in some vegetation-covered areas and on the summit, which freezes at times.

We use a simple model to describe the volcano-wide deflation observed in the interferograms. It assumes a change of pressure in a sphere buried in an elastic half-space [*Mogi*, 1958]. The four parameters in the model are the three-dimensional coordinates of the center of the sphere and the maximum displacement above the sphere's center. The model also calculates the total change in volume. Using the best ascending and descending interferograms (Plates 33a and 33c), we find the two horizontal coordinates for the model sphere. The best fit places the sphere 2 ± 0.5 km east of the central cone of Etna. Next, we estimate the remaining two parameters by trial and error to find a source at 16 ± 3 km depth with a maximum subsidence of 12 ± 1 cm. The fringe patterns are sensitive to the "strength" of the source but relatively insensitive to its depth (Plates 33b and 33d).

We then apply the same procedure to the other interferograms, but varying only the maximum displacement from 0 to 19 cm by steps of 1 cm. The best-fitting model is unambiguous for 12 interferograms to within ± 1 cm for the estimates shown as a function of time in Figure 11. The horizontal position of the spherical source does not vary as a function of time in the model, confirming that the fringes are indeed due to deflation of the volcano. For a given time interval, the amplitude values estimated from ascending interferograms agree with those from descending interferograms, despite their very different geometric sensitivities to east-west displacements.

The subsidence varies as a linear function of time at 21 mm month^{-1} during the last 7 months of the eruption sampled by radar. From GPS measurements, the subsidence of the volcano for the first 5 months of the eruption (inferred from surveys in July 1990 and June 1992), is 19 cm at the summit and 6–8 cm at points located 6–10 km from the top [*Nunnari and Puglisi*, 1994]. If all the observed displacement occurred during the 5 months of eruption, the rate would be 31 mm month^{-1}. The maximum horizontal strain rate predicted by the model is -0.9×10^{-6} month^{-1} for points located on opposite sides of the cone 11 km from the top, a value close to the -0.75×10^{-6} month^{-1} obtained earlier in the eruption [*Bonaccorso et al*., 1994].

The constant subsidence rate estimated by radar is consistent with the stable rate of lava production measured in the field, as shown in Figure 11 [*Smithsonian Institution*, 1991–1993]. The rate of volume decrease at the surface of the volcano deduced from our observation is 34×10^6 m^3 month^{-1}. This rate is not balanced by the production of lava (19×10^6 m^3 month^{-1}). More recent studies of the same data set propose more complete models that include the effects of topographic relief [*Cayol and Cornet*, 1998] and the static troposphere [*Delacourt et al*., 1998].

4.7.2. Long Valley. Radar images acquired in C band over Long Valley caldera in eastern California remain coherent over almost 4 years (Plate 34). The 4-year interferogram is noisier than the 2-year one, indicating that the radar reflective properties of the ground change with time. Both interferograms show a pattern of surface deformation, which *Thatcher and Massonnet* [1997] interpret as uplift centered on the caldera, as expected from ground-based geodetic data [*Langbein et al*., 1995; *Marshall et al*., 1997]. Interferograms spanning 2 and 4 years are consistent with a uniform vertical uplift rate of 30 mm yr^{-1} as determined from leveling surveys. Furthermore, the interferograms reveal the details of localized uplift near the caldera center as well as subsidence coincident with the Casa Diablo geothermal field. They also suggest that the deforming area extends to the southwest of the caldera and the deforming area identified previously.

To explain the observed interferograms, *Thatcher and Massonnet* [1997] use an elastic model that includes ellipsoidal sources [*Davis*, 1986] with parameters estimated from the ground-based surveys [*Langbein et al*., 1995]. They find a better fit than was found with the spherical source model [*Mogi*, 1958].

In addition, the interferograms indicate deformation continues to the southwest beyond the caldera boundary. Such deformation is not revealed by ground survey measurements, which are sparse in this region of high relief. However, seismicity in this region is substantial, supporting the existence of the inflation source at depth that is required to match the interferometric data.

4.8. Subtle Deformation

4.8.1. Landers postseismic. Three studies push satellite radar interferometry close to its typical artifact level to map the postseismic deformation following the Landers, California, earthquake on June 28, 1992 [*Massonnet et al*., 1994a; *Massonnet et al*., 1996b; *Peltzer et al*., 1996]. An interferogram spanning 3 years shows up to 2 fringes (56 mm) of deformation near the fault trace which ruptured the surface during the mainshock (Plate 35). Using pairwise discriminatory logic (section 3.1) and

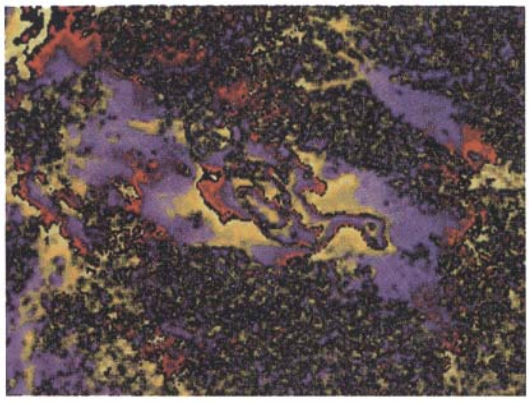

Plate 32. Best descending interferogram at Etna [*Massonnet et al.*, 1995a]. Interferograms from descending orbits (i.e., radar images acquired by day) is generally lower in quality than those from ascending orbits (acquired by night), a phenomenon that we attribute possibly to a more quiescent state of the atmosphere and the vegetation at night.

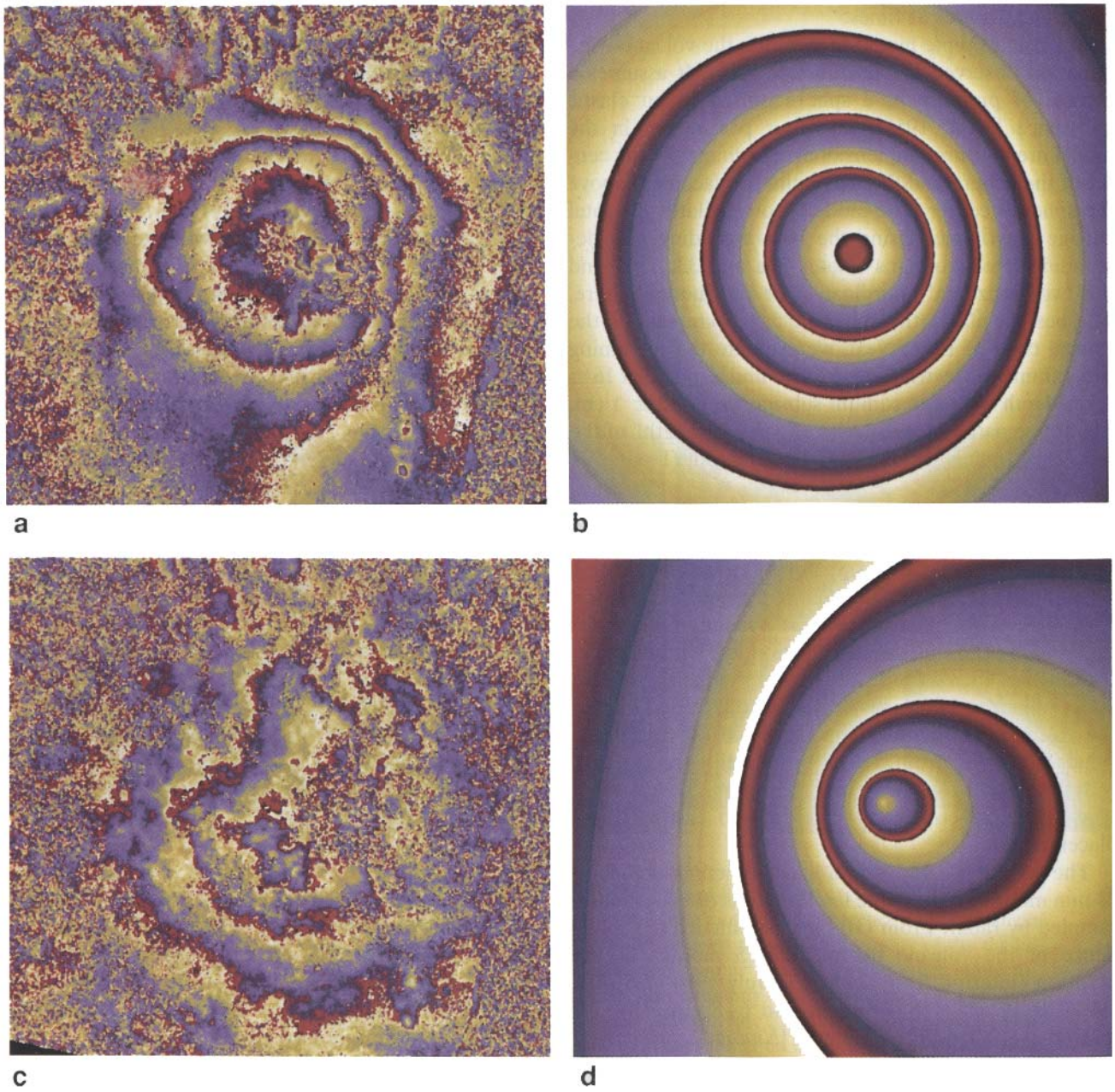

integer combination (section 2.5.4), *Massonnet et al*. [1996b] argue that the signal cannot be an atmospheric artifact. Nor can it be an orbital effect, because the orbital adjustment was obtained by minimizing the phase gradient in selected portions of the interferograms. On the contrary, ground deformation is visible on interferograms spanning [+40, +355] and [+5, +1008] days after the earthquake, albeit with a different amplitude, in the area of the Landers fault.

From the interferogram, we interpret two distinct patterns of deformation. Pattern 1, on the northern and central parts of the surface rupture, consists of a region of range increase southwest of the fault and range decrease to the northeast. It resembles the coseismic fringe pattern (Plate 20) but at much reduced amplitude and without any discontinuity across the fault, immediately suggesting that continued fault slip that does not reach the Earth's surface. Pattern 2, on the southern half of the 1992 fault, shows a much more localized region of range decrease lying within a few kilometers of the Landers fault zone. Local truncations or high gradients in interference fringes near faults indicate near-surface slip at these locations, but these features are exceptional rather than typical. *Massonnet et al*. [1996b] also observe new postseismic slip on the Mojave faults as discontinuities, although no significant events took place in the area.

In addition, *Peltzer et al*. [1996] recognize that the more localized range changes are positive (downward movement) near one compressional jog in the coseismic rupture and negative (upward movement) in two extensional jogs.

Three different mechanisms may operate to produce the observed deformation: (1) afterslip at depth on the fault that ruptured in the earthquake as inferred from GPS surveys [*Shen et al*., 1994], (2) closure of dilatant cracks and fluid expulsion from a transiently overpressured fault zone, suggested by *Massonnet et al*. [1996b] in analogy to *Sleep and Blanpied* [1992], *Byerlee* [1993], and *Savage et al*. [1994]. (3) postseismic movements in the jogs as a consequence of changes in elastic moduli caused by fluid flow in the deformed rocks, favored by *Peltzer et al*. [1996, 1998], using a model proposed earlier [*Nur*, 1972; *Nur and Booker*, 1972].

4.8.2. Iceland. Radar images of the barren, mostly volcanic ground cover in Iceland can remain coherent over at least 3 years if there is no snow on the ground. In practice, the months of August and September seem to be the most reliable, with some successes in July and October.

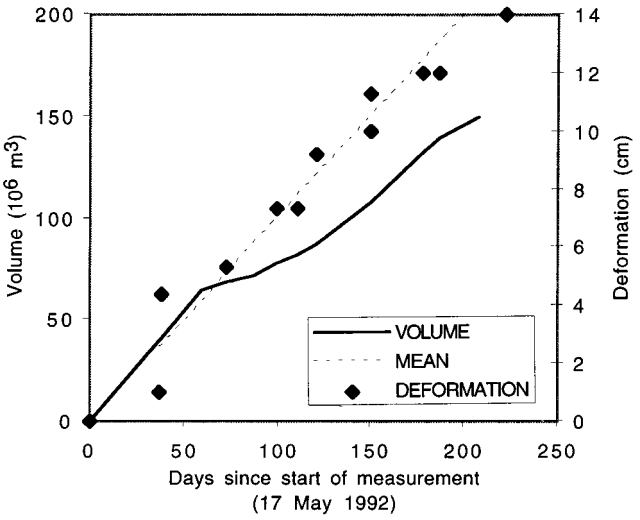

Figure 11. Subsidence of the summit of Etna as a function of time [*Massonnet et al*., 1995a]. The values are deduced from the models that best fit the observed interferograms. The result shows a linear relation between time and displacement that implies a constant rate of volume loss for the volcano (dashed line). The solid line shows the lava production as inferred from field measurements [*Smithsonian Institution*, 1991–1993].

In southwest Iceland, where the Mid-Atlantic Ridge cuts obliquely across the Reykjanes Peninsula, *Vadon and Sigmundsson* [1997] calculated six interferograms from descending orbits spanning intervals of roughly 1 month, 1 year, 2 years, and 3 years. The most obvious deformation signal in their interferograms (Plate 36) is the concentric fringes at the Reykjanes central volcano, which indicate approximately 1.5 fringes (4 cm) of subsidence over 3 years. The underlying geothermal reservoir is the site of a power plant that withdraws fluids, lowering their subsurface pressure. Vadon and Sigmundsson model the resulting surface displacement as if it were a (contracting) spherical volcanic "sink" [*Mogi*, 1958].

In addition, *Vadon and Sigmundsson* [1997] observe a single long, straight fringe striking in a NNE direction, roughly parallel to the plate boundary. Over 3 years this pattern reaches almost a whole fringe (3 cm) of range change. To explain this observation, they use an elastic model to include two effects. The first is the deformation expected from rifting perpendicular to a fault locked to 5-km depth. The magnitude of this displacement decays as an arctangent function of distance. The second effect is the subsidence of the rift itself, which the authors model as a line source of pressure decrease within an elastic half-space.

The complete model includes 11 parameters, which *Vadon and Sigmundsson* [1997] estimate by trial and

Plate 33. (opposite) Observed and modeled fringe patterns for the best ascending interferograms at Etna. One cycle of color corresponds to a 28-mm change in range. About four fringes are visible in *a* indicating a subsidence of the volcano. (b) Best fit model for Plate 33a. The best fit is obtained with a source located 2 ± 0.5 km east of the center cone and at 16-km depth [*Massonnet et al*., 1995a]. (c) Enlargement of Plate 33a, showing posteruptive deformation in the vicinity of a recent (1989) lava flow in the Valle del Bove. The top left corner corresponds to the center of Plate 33a. Fringes have been deliberately obscured where coherence is low. (d) Best fit model for Plate 33c.

error. Their visual inspection suggests that the estimates have uncertainties ranging from 10 to 30%.

In the northern part of Iceland, observed interferograms clearly show the subsidence of Krafla volcano [*Sigmundsson et al*., 1997]. The deformation due to rifting, on the other hand, does not appear clearly. This subtle signal would produce less than a single fringe in a 1-year interferogram. It is probably obscured by a relatively high level of pollution by atmospheric phenomena. It is difficult to separate the rifting signal from the atmospheric noise using pairwise logic because of relative scarcity of pairs, with images acquired only 2 months out of the year. In addition, the orientation of the rifting process produces fringes parallel to the satellite track that could be mistaken for "residual orbit fringes" and thereby partially eliminated by the orbital correction (Plate 3).

4.8.3. Tidal loading. The gravitational potentials of the Sun and the Moon produce an elastic response in the solid Earth that spans the entire planet as spherical harmonic waves of degree 2 with typical amplitudes of 5–50 cm. Their characteristic periods are 0.5 day, 1 day, 1 month, and 1 year [*Melchior*, 1983]. The best available models can predict the vertical displacement as a function of time with an accuracy of about 5 mm, assuming a simple structure for the lithosphere. Even in complex settings, the measured signal deviates by less than about 1% from the predicted value. Such small residuals, combined with long wavelengths, imply that differential satellite radar interferometry will not help refine models for solid Earth tides.

On the other hand, the tidal effects near continental coastlines are both less well understood and easier to measure. Here the potential of the Moon and Sun generates the familiar tides in the oceans, which can be reasonably modeled by the laws of hydrodynamics [*Parker*, 1991]. The rise and fall of the water masses in turn both directly load the crust and induce a second-order gravitational potential perturbation at the same tidal frequency. The total effect of the ocean tide loading produces distortions in the crust of up to 15 cm over continental areas adjacent to strong ocean tides. Typical wavelengths range from 50 to 2000 km, but shorter scales should occur near resonant bays. Theoretical models for calculating the induced load are adequate but reveal shortcomings at ~100-km wavelengths because of insufficient knowledge of both ocean tide patterns and elastic lithospheric structure at these scales [*Francis and Mazzega*, 1990]. Plate 37 shows the vertical displacement calculated from such a model and the deformation measured by satellite radar interferometry in northwestern France. The expected range change varies by only 2 cm over 100 km for a dimensionless gradient of 2×10^{-7}, near the low-gradient limit imposed by orbital errors.

Atmospheric fluctuations also load the solid Earth. Although their spectrum is continuous from a few hours to several months, the response mechanism of the solid Earth is the same as that for tidal loading. The largest variations are a few centimeters in vertical displacement, with typical length scales of 100 to 1000 km, corresponding to the highs and lows of atmospheric pressure [see *Kakkuri*, 1991, and references therein].

All three phenomena produce vertical movements which are difficult to separate from each other because analysis of time series from a few erratically spaced stations can barely decorrelate signals with nearly identical temporal spectra. An interferometric snapshot of the differential displacement between two satellite passes would permit separating the various components by their spatial, rather than temporal, signatures.

4.8.4. Other subtle signals. Here we discuss the prospects for using satellite radar interferometry to measure subtle amounts of crustal deformation. In most cases, either the gradient or the extent is small enough that no radar interferometric measurement has yet been published.

The continental crust rebounds in response to the unloading by melting of the late Pleistocene ice caps. Present rates of uplift in Fennoscandia, for example, approach 1 cm yr^{-1} [*Lambeck*, 1988]. Spread out over 1200 km along the Fennoscandia Peninsula, such a rate produces an annual change in the displacement gradient of the order of 10^{-8}, well below the shallow-gradient limit.

In between large earthquakes, the crust accumulates strain more or less elastically as interseismic deformation. The San Andreas fault in California helps establish the order of magnitude of the signal to expect at a plate boundary. If we suppose that about 35 mm yr^{-1} of deformation is spread over the boundary between the North America and Pacific plates with a width of ~100 km, then we expect the deformation gradient to change by $\sim 3 \times 10^{-7}$ per year. Such a signal would be detectable by radar interferometry if the geometry were more favorable than the 55° angle between the relative velocity vector and the ERS satellite track. Measuring vertical motion, such as on a fold overlying a blind thrust fault, would be easier. Where the deformation is concentrated in a narrow zone, around the creeping section near Parkfield, *Rosen et al*. [1998] detect an offset in a C band interferogram spanning 14 months. *Fujiwara et al*. [1998] consider subtle tectonic deformation on the Izu Peninsula.

Around the southern polar ice cap, variations in precipitation perturb the ice mass loading the Antarctic continent enough to alter the elevation of the rocky coast. Seasonal and annual variations in vertical position do not exceed 1 mm in magnitude over spatial scales approaching ~1000 km, rendering them difficult to detect by any geodetic technique [*Conrad and Hager*, 1995].

Mountain ranges grow at rates of the order of ~1 mm yr^{-1} with respect to the surrounding planes. For a small range ~100 km wide, this value implies an annual change in deformation gradient of 10^{-8}, too small to measure easily with radar interferometry. If, however, the uplift concentrates on a small structure (say, ~1 cm yr^{-1} over 10 km), then the annual change in gradient would be $\sim 10^{-6}$, a much more feasible value. The risk, however, is that such deformation may tend to occur in the highest mountains, where the relief is rugged (and

the elevation model poor) and snow is present (and the coherence low). Furthermore, the rate of erosion, the most problematic parameter in mountain building, cannot be easily measured by radar interferometry. Almost by definition, erosion will alter the reflective properties of the ground surface, reducing the coherence in an interferogram.

Evaporite deposits in upwelling salt domes and oozing salt glaciers can flow at rates of 10^{-15} year^{-1} to 10^{-11} year^{-1} [*Carter and Hansen*, 1983], corresponding to ~0.3 mm yr^{-1} to 3 m yr^{-1} for a salt structure ~1 km in size. Rates as fast as 4 m yr^{-1} on average, or even 50 cm d^{-1} after a rain, have been observed [*Talbot*, 1998]. Such deformation falls within the limits of interferometry provided that the salt surface does not change too much between images and that the feature is large enough to cover at least 10 pixels.

Petroleum extraction also produces subsidence as fast as 8 mm yr^{-1} [*Buchanan-Banks et al*., 1975]. Even in cases where waste fluids are reinjected into the ground, the net result is probably still subsidence of the order of several millimeters per year. Spread over several kilometers, such a signal is just large enough to measure by radar interferometry, but we know of no published example.

Measuring these subtle phenomena will require approaching the practical limits of satellite interferometry. Distinguishing crustal deformation from radar artifacts will necessitate models accurate enough to identify the geophysical signal on the basis of its spatial signature. Furthermore, many of the subtle, interesting signals are slow enough that we will want an interferogram spanning at least a decade in time.

5. CONCLUSIONS AND PERSPECTIVES

Geophysical applications of radar interferometry to measure changes in the Earth's surface have exploded in the early 1990s. This period of rapid progress required the simultaneous presence of data, a technique, and an event.

After the untimely demise of Seasat in 1978, radar specialists had to wait 13 years for a civilian radar satellite orbiting Earth before the successful launch of ERS-1 in 1991. Three more radar satellites, JERS-1, ERS-2, and RADARSAT, followed within 4 years. ERS, for example, images over 5 million square kilometers per day, providing some 0.12 terabytes of raw data, all of it potentially useful for interferometry if a proper partner image exists.

Several space agencies acknowledged the potential for satellite radar interferometry. They allowed development of processing techniques to proceed in parallel with more traditional remote-sensing techniques. Radar research teams flourished in Pasadena, Toulouse, Milan, and Ottawa. Although progress was rapid, the excitement in the late 1980s seemed limited to the "radarist" community before the other two requirements were met.

The Landers, California, earthquake in June 1992, just a few months after ERS-1 first began furnishing data in its 35-day cycle, satisfied all the necessary conditions for a solid test case: hefty surface rupture in a dry desert area in the middle of one of the best surveyed pieces of continental crust on the planet.

The remainder of this period of rapid development and validating applications fills the preceding pages. As this exciting first phase draws to a close, however, can we anticipate future developments?

Yes. We know that the future will build on the past because of the need to span long intervals of time to measure slow, gradual signals, such as interseismic strain accumulation. The huge archive of data acquired since 1992 by ERS-1, and now ERS-2, has imposed a de facto standard for interferometry, even though the C band wavelength, orbit, and incidence angle are not perfectly optimal for interferometric applications. The standard is likely to persist until at least the end of the planned useful life of ERS-2 at the turn of the century.

The four SAR satellites currently in orbit (ERS-1, ERS-2, JERS-1, and RADARSAT) ensure the feasibility of interferometry for many years to come. In addition, three more missions capable of radar interferometry (*ALOS*, ENVISAT, and SRTM) are approved and planned for launch in the first few years of the next millennium. Although geophysicists should consider themselves fortunate to have such a wealth of data, we note with some dismay that none of the new, planned satellites will acquire images that are interferometrically compatible with images acquired by the current generation. For example, an ENVISAT image acquired in 2007 will not combine with an ERS-1 image acquired in 1992 to form a 15-year interferogram.

Because of their concern for long time series of Earth observations, geophysical users of interferometric SAR data must work to ensure that future satellite radar missions can provide data useful for interferometric monitoring of slow moving phenomena. One way to meet this challenge is to dedicate a SAR satellite mission to interferometry alone. The simplest design would duplicate the C band wavelength, orbit, and incidence angle of ERS-1. If launched around 2003, such a satellite would provide data suitable for interferometric combination with early ERS-1 data. Such interferograms would measure ground movements over 12 years and more. We would see anything and everything that moved in the observation period, except, of course, where coherence broke down or no early images were available. This kind of continuity, even if interrupted for a few years, would make it possible to detect movements of the order of 1 mm yr^{-1}. Such a dedicated mission could be optimized for detecting and measuring changes in the Earth's surface. For example, an L band radar instrument capable of looking to either the left or the right of the satellite would allow interferometric measurement of four nonorthogonal components of motion when used in both ascending and descending orbital passes. This would make it possible to recover the entire three-dimensional vector field of crustal deformation, instead of just a single scalar component as for all interferomet-

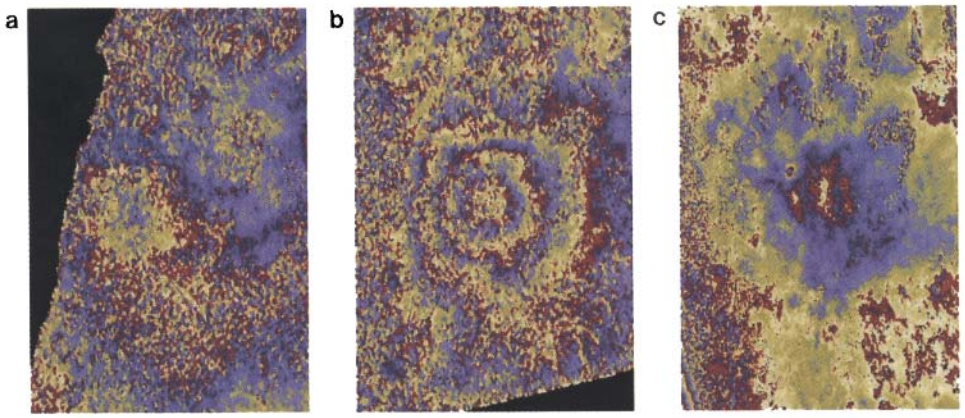

Plate 34. (a) Long Valley interferogram from ERS-1 images acquired on July 3, 1993, and May 22, 1995, on an ascending track (h_a = 394 m, 1.88 years). Each fringe represents 28 mm of motion. Each panel shows the same area centered on the caldera (37 km E-W by 46 km N-S). SAR interferometry confirms the 2-cm uplift already observed by conventional geodetic means. In addition, it provides an accurate map of the limits of the deformed area, bringing new insight into the caldera and possibly contributing to better positioning of conventional instrumentation in the future. (b) Long Valley interferogram from ERS-1 images acquired on July 25, 1992, and May 13, 1996, on a descending track (h_a = 229 m, 3.81 years). This interferogram provides another time interval as well as an opposite sensitivity to east-west displacements. (c) Interferogram from along the same track as Plate 34b, spanning a shorter period (October 3, 1992, and September 18, 1993; almost 1 year) and showing only a fraction of the displacement accumulated in Plate 34b.

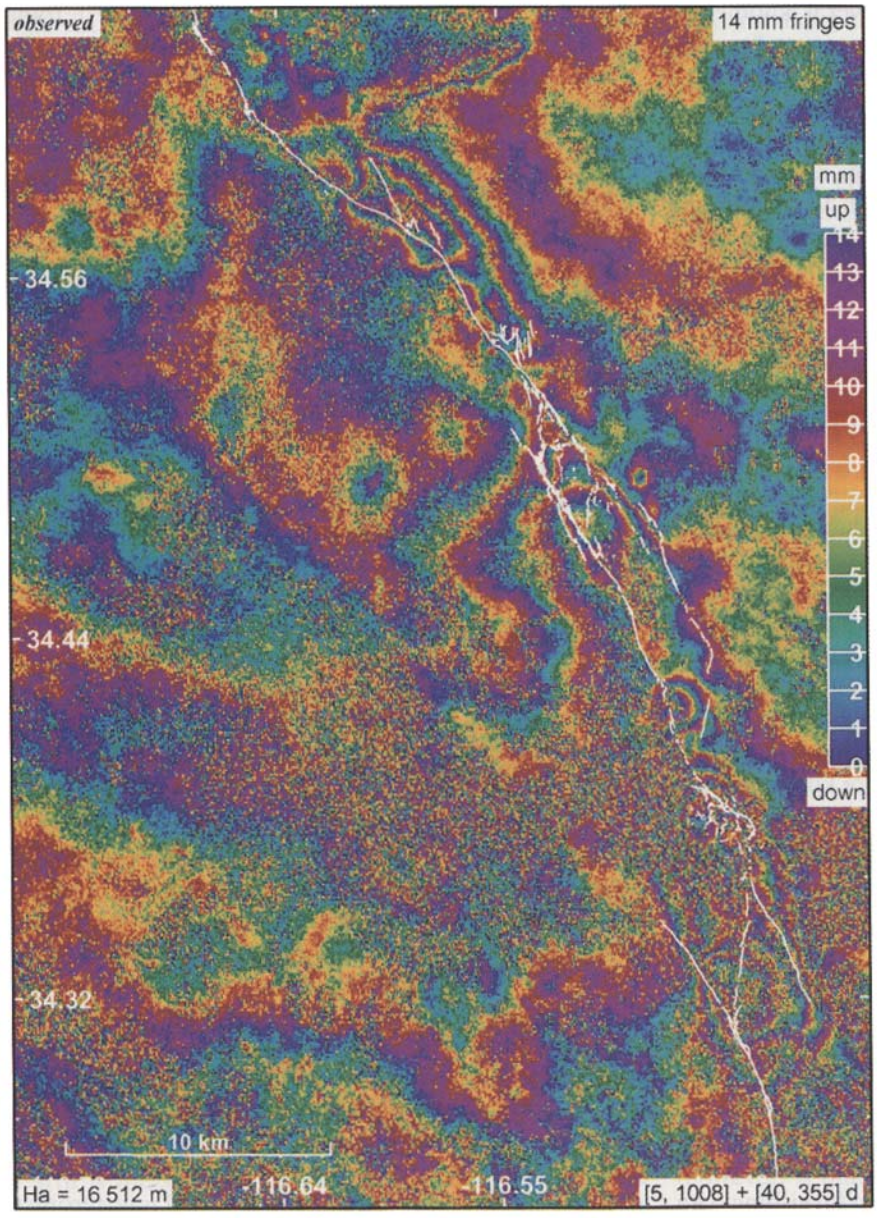

Plate 35. Landers postseismic interferogram constructed by adding two interferograms made of ERS-1 radar images acquired on July 3, 1992, and April 2, 1995, and then again on August 7, 1992, and June 18, 1993. This combined interferogram records deformation between 5 and 1008 days after the June 28, 1992, earthquake [*Massonnet et al.*, 1996b]. We interpret each fringe as approximately 14 mm of change in range, assuming that the stacking doubles the deformation signal during the time interval common to both interferograms and neglecting the deformation outside this common time interval. The effective altitude of ambiguity h_a is more than 16,000 m, eliminating the topographic contribution. White lines indicate coseismic rupture as mapped in the field [*Sieh et al.*, 1993].

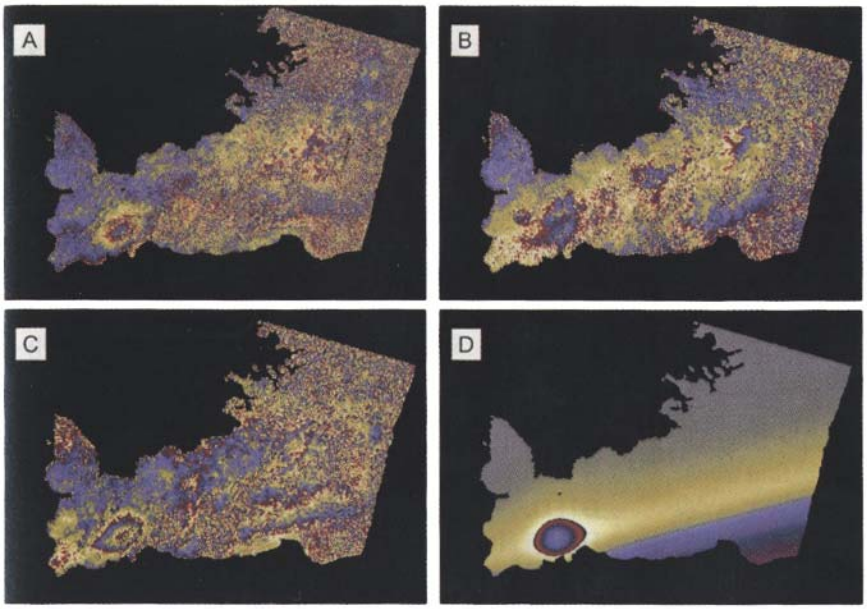

Plate 36. Interferograms of the peninsula near Reykjavík, SW Iceland, spanning (a) 0.83 years, (b) 2.29 years, and (c) 3.12 years, and (d) model interferogram showing best fit simulation of 2.29 years' deformation. Time-progressive fringes appearing consistently in the interferograms are indicative of crustal deformation. Concentric fringes at the Reykjanes central volcano reach up to 1.5 cycle over 3 years, with most of the associated subsidence due to the activity of a geothermal plant (similar to Plate 25). Spreading on the plate boundary is visible especially in the 2- and 3-year interferograms (Plates 36b and 36c), and the rifting process can be observed and modeled [*Vadon and Sigmundsson*, 1997].

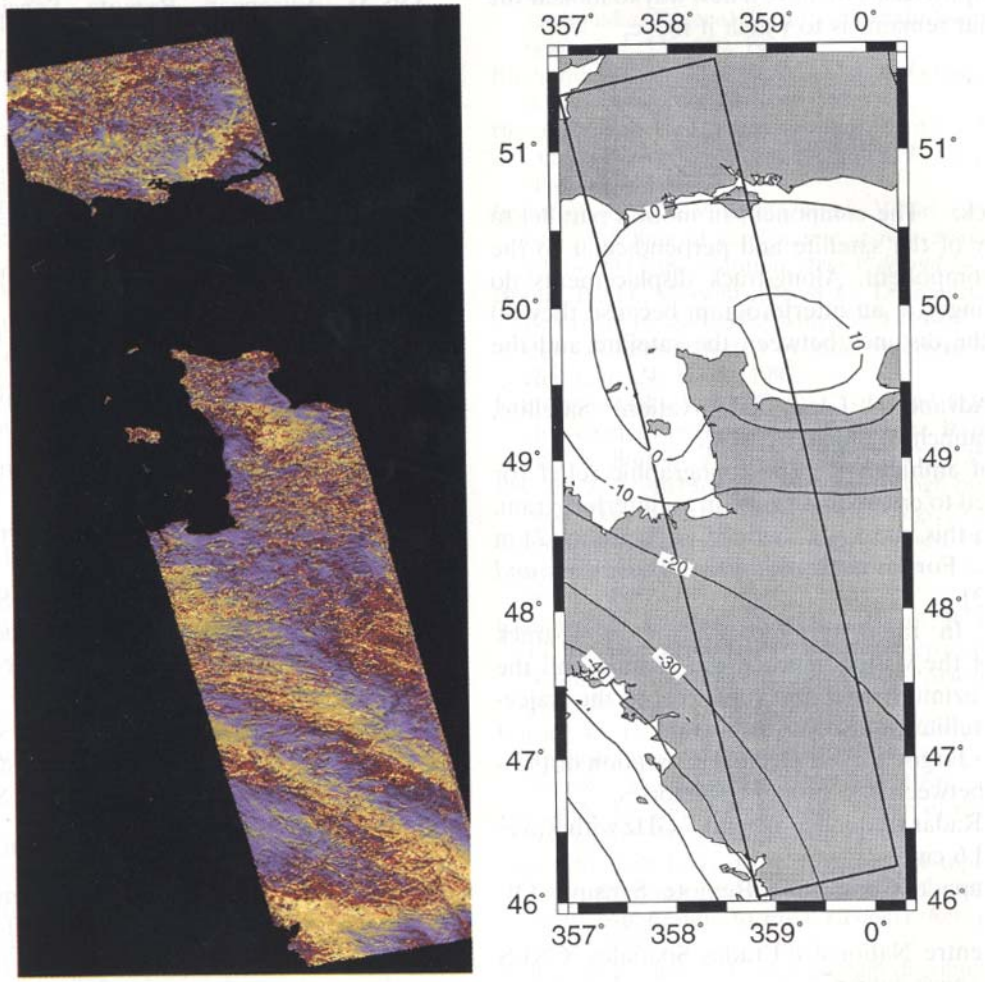

Plate 37. Movement from loading by tides over western France and southern Great Britain. (left) The observed interferogram spans August 28 to September 3, 1991. Both images were acquired at the same time of day, 2212 UTC. The topographic contribution has been approximately removed from the interferogram. (right) A theoretical model predicts movements of the order of 20 mm and over length scales of ~100 km, an exceptionally low deformation gradient [*Llubes and Mazzega*, 1996]. To capture this subtle signal, we employ a long strip of data including six ERS frames, each ~100 km by 100 km, to reach stationary reference points for the orbital correction. The main challenge is distinguishing the very small deformation gradients from artifacts.

ric radar satellites to date. A plan integrating all of these features, ECHO Elsie, has been submitted to NASA and CNES.

Yet geophysical applications of radar interferometry will continue to grow in number even before any of these plans become reality. As the examples in this review illustrate, radar interferograms are a now a valid form of geophysical measurement. They have sampled familiar signals with unprecedented spatial density and have compared favorably with measurements made on the ground, theoretical models, and engineering expectations. In short, the technical state of the art is now sufficiently high that many new and exciting geophysical applications are already within reach without the need for further developments in processing. In that sense, radar interferometry for geophysics in the late 1990s seems to be at about the same position as optical satellite (e.g., SPOT) imagery in the late 1980s or space geodetic surveying techniques (e.g., GPS) in the early 1990s. As geophysicists, we have a new way to look at the Earth. All that remains is to watch it move.

GLOSSARY

Along track: The component of motion parallel to the trajectory of the satellite and perpendicular to the cross-track component. Along-track displacements do not create fringes in an interferogram because they do not change the distance between the satellite and the ground.

ALOS: Advanced Land Observation Satellite, planned for launch by Japan by 2002.

Altitude of ambiguity: The topographic relief (or error) required to create one fringe in an interferogram, denoted h_a in this paper and defined in equation (2) in section 1.2.3. For a derivation, see *Massonnet and Rabaute* [1993].

Azimuth: In radar terminology, the along-track component of the vector between the ground and the satellite. The azimuth direction is parallel to the trajectory of the satellite.

Baseline: Jargon for the (vector) separation or (scalar) distance between two orbital trajectories.

C band: Radar frequency around 5 GHz with wavelength around 6 cm.

CCRS: Canada Centre for Remote Sensing, Ottawa, Canada.

CNES: Centre National d'Etudes Spatiales. CNES is the French space agency.

Coherence: The degree of agreement between neighboring pixels in an interferogram (see section 2.3 and equation (5)).

Cross-track: Component of motion perpendicular to the trajectory of the satellite.

DEM: Digital elevation model. A DEM is a two-dimensional array of topographic elevations.

DIAPASON: Differential Interferometric Automated Process Applied to Survey of Nature, CNES software for calculating interferograms.

DMA: Defense Mapping Agency. DMA is the U.S. military topographic service.

Dip: Angle formed between a fault and the Earth's surface.

Displacement vector: Movement of a point on the Earth's surface. Usually defined in a local (east, north, up) coordinate system. Denoted as **u**.

Doppler: Shift in frequency due to the motion of the radar instrument.

Double-difference: Term sometimes used to denote the difference of two interferograms, each of which is the difference of two radar images.

DTED: Digitial Terrain Elevation Data.

ECHO Elsie: Earth Change Hazard Observatory, a concept for interferometric L and C band radar satellite proposed to NASA and CNES. See section 5.

ERS-1: European Remote Sensing satellite 1, launched in 1991.

ERS-2: Twin of ERS-2, launched in 1995.

ESA: European Space Agency.

Focal mechanism: Three parameters (strike, dip, and rake) describing the geometric orientation of an earthquake slip vector on the fault plane.

Fringe: Line in an interferogram corresponding to half a wavelength of range change or h_a meters of topographic relief.

GPS: Global Positioning System. GPS is a dual-frequency L band satellite navigation system. For reviews, see *Dixon* [1991], *Hager et al*. [1991], and *Segall and Davis* [1997].

IIC: Integer interferogram combination. See section 2.5.4.

InSAR or ISAR: Interferometric synthetic aperture radar.

JERS-1: Japanese Earth Resource Satellite 1.

JPL: Jet Propulsion Laboratory, Pasadena, California.

L band: Radar frequency around 1.2 GHz with wavelength around 25 cm.

Landsat: Series of optical imaging satellites.

MITI: Ministry of Trade and Industry, Japan.

NASA: National Aeronautics and Space Administration, the U.S. space agency.

NASDA: Japanese Space Agency.

Phase: Part of a complex radar image containing the geometric information on the round-trip travel time between the radar instrument and the reflector on the ground.

PRISME: Processeur pour Radars Imageurs Spatiaux, Multi-Etage, CNES SAR focusing (processing) software.

RADARSAT: Multi-mode, C band radar satellite launched by Canada in 1995.

Rake: Angle between the slip vector on a fault plane and the horizontal.

Range: Distance along the line of sight between the satellite and the ground.

SAR: Synthetic aperture radar, a technique for improving radar resolution (see section 1.1.1).

Seasat: L band radar satellite with altimeter that flew only for several months in 1978.

SIR-C: Shuttle imaging radar C.

SLC: Single look complex, a radar image including both phase and amplitude information, after processing by the synthetic aperture resolution reconstruction process. See section 2.1.

Slip: The relative displacement vector produced by an earthquake between two blocks separated by a fault.

SPOT: Satellite Pour l'Observation de la Terre, a series of optical imaging satellites with a resolution of 10 or 20 m for Earth observation.

SRTM: Shuttle Radar Topographic Mission. See section 1.3.5.

Strike: Angle between north and the intersection of a fault plane with the Earth's surface.

Three-pass interferometry: Approach to calculating interferograms that uses three radar images but no elevation model. Also called double differencing. See section 2.4.3.

TOPSAR: A radar instrument for mapping topography developed by JPL and flown aboard a NASA DC-8 airplane.

TOPSAT: A satellite concept proposed by NASA to map the Earth's topographic field [see *Farr et al*., 1995a, b].

Two-pass interferometry: Approach to calculating interferograms that uses two radar images and an elevation model. Also called DEM elimination. See section 2.4.2.

VLBI: Very long baseline interferometry. A geodetic technique for extremely precise estimates of absolute position of bench marks on the Earth's surface. See *Herring* [1992] for a review.

X band: Radar frequency around 9 GHz with wavelength around 3 cm.

X-SAR: X band radar instrument carried aboard the space shuttle *Endeavor* in 1994 [*Moreira et al*., 1995; *Coltelli et al*., 1996].

ACKNOWLEDGMENTS. We thank the Editors, Wayne Thatcher and an anonymous reviewer for interesting discussions and insightful comments. Warm thanks to all who contributed their time to analyze data, in particular Hélène Vadon. Francoise Briot and Celine Arnaud provided useful bibliographic assistance. ESA and NASA provided some of the raw data used for the Etna figures free of charge as part of their investigators' program. The GDR facilitated this work. We thank our respective agencies, CNES and CNRS, for allowing us the flexibility needed to complete this work.

Peter Molnar and Roel Snieder were the Editors responsible for this paper. They thank Wayne Thatcher and an anonymous referee for technical reviews.

REFERENCES

Ainsworth, T. L., S. R. Chubb, R. A. Fusina, R. M. Goldstein, R. W. Jansen, J. S. Lee, and G. R. Valenzuela, INSAR imagery of surface currents, wave fields, and fronts, *IEEE Trans. Geosci. Remote Sens*., *33*, 1117–1123, 1995.

Alberti, G., and S. Ponte, Three dimensional digital elevation model of Mt. Vesuvius from NASA/JPL TOPSAR, *Int. J. Remote Sens*., *17*, 1797–1801, 1996.

Amelung, F., D. Galloway, J. Bell, H. Zebker, and R. Laczniak, Sensing Las Vegas' ups and downs: InSAR reveals structural control of land subsidence and aquifer-system deformation (abstract), *Eos Trans. AGU*, in press, 1998.

Arnaud, A., Etude et analyse des artefacts dans la construction de l'image interferométrique, Ph.D thesis, 194 pp., Inst. Natl. Polytech. de Toulouse, Toulouse, France, 1997.

Bamler, R., and P. Hartl, Synthetic aperture radar interferometry, *Inverse Problems*, *14*, R1–R54, 1998.

Beaudoin, A., T. Le Toan, and Q. H. J. Gwyn, SAR observations and modeling of the C-band backscatter variability due to multiscale geometry and soil moisture, *IEEE Trans. Geosci. Remote Sens*., *28*, 886–895, 1990.

Bernard, P., et al., The *Ms* = 6.2 June 15, 1995, Aigion earthquake (Greece): Results of a multidisciplinary study, *J. Seismol*., *1*, 131–150, 1996.

Bindschlader, R., Monitoring ice sheet behavior from space, *Rev. Geophys*., *36*, 79–104, 1998.

Blom, R., and C. Elachi, Spaceborne and airborne imaging radar observations of sand dunes, *J. Geophys. Res*., *86*, 3061–3073, 1981.

Bonaccorso, A., R. Velardita, and L. Villari, Ground deformation modelling of geodynamic activity associated with the 1991–1993 Etna eruption, *Acta Vulcanol*., *4*, 87–96, 1994.

Briole, P., D. Massonnet, and C. Delacourt, Post-eruptive deformation associated with the 1986–87 and 1989 lava flows of Etna detected by radar interferometry, *Geophys. Res. Lett*., *24*, 37–40, 1997.

Buchanan-Banks, L. M., R. O. Castle, and J. I. Ziony, Elevation changes in the central Transverse Ranges near Ventura, California, *Tectonophysics*, *29*, 113–125, 1975.

Byerlee, J., Model for episodic flow of high-pressure water in fault zones before earthquakes, *Geology*, *21*, 303–306, 1993.

California Division of Mines and Geology, Preliminary fault activity map of California, Calif. Dep. of Conserv., Sacramento, 1992.

Campbell, D. B., R. B. Dyce, F. S. Harris, R. F. Jurgens, and G. H. Pettengill, Radar interferometric observations of Venus at 70-centimeter wavelength, *Science*, *170*, 1090–1092, 1970.

Carnec, C., D. Massonnet, and C. King, Two examples of the application of SAR interferomety to sites of small extent, *Geophys. Res. Lett*., *23*, 3579–3582, 1996.

Carter, N. L., and F. D. Hansen, Creep of rocksalt, *Tectonophysics*, *92*, 275–333, 1983.

Cayol, V., and F. H. Cornet, Effects of topography on the interpretation of the deformation field of prominent volcanoes—Application to Etna, *Geophys. Res. Lett*., *25*, 1979–1982, 1998.

Cohee, B. P., and G. C. Beroza, Slip distribution of the 1992 Landers earthquake and its implications for earthquake source mechanics, *Bull. Seismol. Soc. Am*., *84*, 692–712, 1994.

Coltelli, M., G. Fornaro, G. Franceschetti, R. Lanari, M. Migliaccio, J. R. Moreira, K. P. Papathanassiou, G. Puglisi, D. Riccio, and M. Schwäbisch, SIR-C/X-SAR multifrequency multipass interferometry: A new tool for geological interpretation, *J. Geophys. Res*., *101*, 23,127–23,148, 1996.

Conrad, C. P., and B. H. Hager, The elastic response of the

Earth to interannual variations in Antarctic precipitation, *Geophys. Res. Lett*., *22*, 3183–3186, 1995.

Curlander, J. C., Interferometric radar earns high marks in mapping applications, *Earth Observ. Mag*., *4*, 52–54, 1995.

Curlander, J. C., and R. N. McDonough, *Synthetic Aperture Radar: Systems and Signal Processing*, 647 pp., John Wiley, New York, 1991.

Dammert, P. B. G., and J. O. Hagberg, SAR interferometry for measuring fast ice displacement and ice ridge height, in *Baltic Experiment for ERS-1 (BEERS)*, edited by L. Ulander, *Res. Rep. 51*, pp. 123–136, Winter Navig. Res. Board, Göteborg, Sweden, 1994.

Davis, P. M., Surface deformation due to inflation of an arbitrarily oriented triaxial cavity in an elastic half-space, with reference to Kilauea volcano, Hawaii, *J. Geophys. Res*., *91*, 7429–7438, 1986.

Delacourt, C., P. Briole, and J. Achache, Tropospheric corrections of SAR interferograms with strong topography: Application to Etna, *Geophys. Res. Lett*., *25*, 2849–2852, 1998.

Dixon, T. H., An introduction to the Global Positioning System and some geological applications, *Rev. Geophys*., *29*, 249–276, 1991.

Donald, J. R., F. R. Seglenieks, E. D. Soulis, N. Kouwen, and D. W. Mullins, Mapping partial snowcover during the melt season using C-band SAR imagery, *Can. J. Remote Sens*., *19*, 68–76, 1993.

Elachi, C., Radar images of the Earth from space, *Sci. Am*., *247*(12), 46–53, 1982.

Elachi, C., *Introduction to the Physics and Techniques of Remote Sensing*, 413 pp., John Wiley, New York, 1987.

Farr, T., D. Evans, H. Zebker, D. Harding, J. Bufton, T. Dixon, S. Vetrella, and D. Gesch, The global topography mission gains motentum, *Eos Trans. AGU*, *76*, 213–218, 1995a.

Farr, T., D. Evans, H. Zebker, D. Harding, J. Bufton, T. Dixon, S. Vetrella, and D. Gesch, Mission in the works promises precise global topographic data, *Eos Trans. AGU*, *76*, 225–228, 1995b.

Feigl, K. L., and E. Dupré, RNGCHN: A program to calculate displacement components from dislocations in an elastic half-space with applications for modeling geodetic measurements of crustal deformation, *Comput. Geosci*., in press, 1998.

Feigl, K. L., and D. Massonnet, Seismology from space: Estimation of fault parameters by inversion of radar interferograms (abstract), *Eos Trans. AGU*, *76*(17), Spring Meet. Suppl., S196, 1995.

Feigl, K. L., and G. Peltzer, Estimation of the slip distribution in the June 28 Landers earthquake sequence by inversion of a coseismic radar interferogram (abstract), *Eos Trans. AGU*, *74*(43), Fall Meet. Suppl., 183, 1993.

Feigl, K. L., A. Sergent, and D. Jacq, Estimation of an earthquake focal mechanism from a satellite radar interferogram: Application to the December 4, 1992, Landers aftershock, *Geophys. Res. Lett*., *22*, 1037–1048, 1995.

Follacci, J. P., P. Guardia, and J. P. Ivaldi, Geodynamic framework of La Clapière landslide (Maritimes Alps, France), in *Proceedings of the Fifth International Symposium on Landslides*, edited by C. Bonnard, pp. 1323–1327, A. A. Balkema, Brookfield, Vt., 1988.

Fornaro, G., G. Franceschetti, and R. Lanari, Interferometric SAR phase unwrapping using Green's formulation, *IEEE Trans. Geosci. Remote Sens*., *34*, 720–727, 1996.

Francis, O., and P. Mazzega, Global charts of ocean tide loading effects, *J. Geophys. Res*., *95*, 11,411–11,424, 1990.

Freymueller, J., N. E. King, and P. Segall, The coseismic slip distribution of the Landers earthquake, *Bull. Seismol. Soc. Am*., *84*, 646–659, 1994.

Fruneau, B., J. Achache, and C. Delacourt, Observation and modelling of the Saint-Etienne-de-Tinée landslide using SAR interferometry, *Tectonophysics*, *265*, 181–190, 1996.

Fujiwara, S., P. A. Rosen, M. Tobita, and M. Murakami, Crustal deformation measurements using repeat-pass JERS 1 synthetic aperture radar interferometry near the Izu Peninsula, Japan, *J. Geophys. Res*., *103*, 2411–2426, 1998.

Gabriel, A. K., and R. M. Goldstein, Crossed orbit interferometry: Theory and experimental results from SIR-B, *Int. J. Remote Sens*., *9*, 857–872, 1988.

Gabriel, A. K., R. M. Goldstein, and H. A. Zebker, Mapping small elevation changes over large areas: differential radar interferometry, *J. Geophys. Res*., *94*, 9183–9191, 1989.

Gatelli, F., A. M. Guarnieri, F. Parizzi, P. Pasquali, C. Pratti, and F. Rocca, The wavenumber shift in SAR interferometry, *IEEE Trans. Geosci. Remote Sens*., *32*, 855–865, 1994.

Gens, R., and J. L. Van Genderen, SAR interferometry—Issues, techniques, applications, *Int. J. Remote Sens*., *17*, 1803–1835, 1996.

Ghiglia, D. C., and M. D. Pritt, *Two-Dimensional Phase Unwrapping: Theory, Algorithms, and Software*, 493 pp., John Wiley, New York, 1998.

Ghiglia, D., and L. Romero, Robust two-dimensional weighted and unweighted phase unwrapping using fast transforms and iterative methods, *J. Opt. Soc. Am. A Opt. Image Sci*., *11*, 107–117, 1994.

Ghiglia, D., G. Mastin, and L. Romero, Cellular-automata method for phase unwrapping, *J. Opt. Soc. Am*., *4*, 267–280, 1987.

Goldstein, R., Atmospheric limitations to repeat-track radar interferometry, *Geophys. Res. Lett*., *22*, 2517–2520, 1995.

Goldstein, R. M., and H. A. Zebker, Interferometric radar measurent of ocean surface currents, *Nature*, *328*, 707–709, 1987.

Goldstein, R. M., H. A. Zebker, and C. L. Werner, Satellite radar interferometry: Two-dimensional phase unwrapping, *Radio Sci*., *23*, 713–720, 1988.

Goldstein, R. M., T. P. Barnett, and H. A. Zebker, Remote sensing of ocean currents, *Science*, *246*, 1282–1285, 1989.

Goldstein, R. M., H. Engelhardt, B. Kamb, and R. M. Frolich, Satellite radar interferometry for monitoring ice sheet motion: Application to an Antartic ice stream, *Science*, *262*, 1525–1530, 1993.

Graham, L. C., Synthetic interferometer radar for topographic mapping, *Proc. IEEE*, *62*, 763–768, 1974.

Gray, A. L., and P. J. Farris-Manning, Repeat-pass interferometry with airborne synthetic aperture radar, *IEEE Trans. Geosci. Remote Sens*., *31*, 180–191, 1993.

Griffiths, H., Interferometric synthetic aperture radar, *Electron. Commun. Eng. J*., *7*, 247–256, 1995.

Griffiths, H. D., and A. J. Wilkinson, Improvements in phase unwrapping algorithms for interferometric SAR, *Onde Electr*., *4*, 46–52, 1994.

Guarnieri, A. M., and C. Prati, SAR interferometry: A 'quick and dirty' coherence estimator for data, *IEEE Trans. Geosci. Remote Sens*., *35*, 660–669, 1997.

Hagberg, J. O., L. M. H. Ulander, and J. Askne, Repeat-pass SAR interferometry over forested terrain, *IEEE Trans. Geosci. Remote Sens*., *33*, 331–340, 1995.

Hager, B. H., R. W. King, and M. H. Murray, Measurement of crustal deformation using the Global Positioning System, *Annu. Rev. Earth Planet. Sci*., *19*, 351–382, 1991.

Harris, R. A., and R. W. Simpson, Changes in static stress on southern California faults after the 1992 Landers earthquake, *Nature*, *360*, 251–254, 1992.

Hauksson, E., L. M. Jones, K. Hutton, and D. Eberhart-Phillips, The 1992 Landers earthquake sequence, *J. Geophys. Res*., *98*, 19,835–19,858, 1993.

Hauksson, E., L. M. Jones, and K. Hutton, The 1994 Northridge earthquake sequence in California: Seismolog-

ical and tectonic aspects, *J. Geophys. Res.*, *100*, 12,335–12,355, 1995.

Hernandez, B., F. Cotton, M. Campillo, and D. Massonnet, A comparison between short-term (co-seismic) and long-term (one year) slip for the Landers earthquake: Measurements from strong motion and SAR interferometry, *Geophys. Res. Lett.*, *24*, 1579–1582, 1997.

Herring, T. A., Submillimeter horizontal position determination using very long baseline interferometry, *J. Geophys. Res.*, *97*, 1981–1990, 1992.

Hudnut, K. W., et al., Coseismic displacements of the 1992 Landers earthquake sequence, *Bull. Seismol. Soc. Am.*, *84*, 625–645, 1994.

Hudnut, K. W., et al., Co-seismic displacements of the 1994 Northidge, California, earthquake, *Bull. Seismol. Soc. Am.*, *86*, S49–S70, 1995.

Jaumé, S. C., and L. R. Sykes, Changes in state of stress on the southern San Andreas fault resulting from the California earthquake sequence of April to June, 1992, *Science*, *258*, 1325–1328, 1992.

Johnson, H. O., D. C. Agnew, and K. Hudnut, Extremal bounds on earthquake moment from geodetic data: Application to the Landers earthquake, *Bull. Seismol. Soc. Am.*, *84*, 660–667, 1994.

Jones, L. E., and S. E. Hough, Analysis of broadband recordings of the June 28, 1992, Big Bear earthquake: Evidence for a multiple-source event, *Bull. Seismol. Soc. Am.*, *85*, 688–704, 1994.

Jonsson, S., N. Adam, and H. Bjornsson, Effects of subglacial geothermal activity observed by satellite radar interferometry, *Geophys. Res. Lett.*, *25*, 1059–1062, 1998.

Joughin, I. R., D. P. Winebrenner, and M. A. Fahnestock, Observations of ice-sheet motion in Greenland using satellite radar interferometry, *Geophys. Res. Lett.*, *22*, 571–574, 1995.

Joughin, I., S. Tulaczyk, M. Fahnestock, and R. Kwok, A mini-surge on the Ryder Glacier, Greenland, observed via satellite radar interferometry, *Science*, *274*, 228–230, 1996.

Just, D., and R. Bamler, Phase statistics of interferograms with applications to synthetic aperture radar, *Appl. Opt.*, *33*(20), 4361–4368, 1994.

Kakkuri, J. (Ed.), *Proceedings of the 11th International Symposium on Earth Tides*, 662 pp., Schweizerbartische, Stuttgart, Germany, 1991.

Klees, R., and D. Massonnet, Deformation measurements using SAR interferometry: Potential and limitations, *Geol. Mijnbouw*, in press, 1998.

Kovaly, J. J., *Synthetic Aperture Radar*, 333 pp., Artech House, Dedham, Mass., 1976.

Kwoh, L., E. Chang, W. Heng, and K. Lim, DTM generation from 35-day repeat pass ERS-1 interferometry, in *International Geoscience and Remote Sensing Symposium 94: Surface and Atmospheric Remote Sensing: Technologies, Data Analysis, and Interpretation*, pp. 2288–2290, IEEE Press, Piscataway, N. J., 1994.

Kwok, R., and G. F. Cunningham, Backscatter characteristics of the winter ice cover in the Beaufort Sea, *J. Geophys. Res.*, *99*, 7787–7802, 1994.

Kwok, R., and M. A. Fahnestock, Ice sheet motion and topography from radar interferometry, *IEEE Trans. Geosci. Remote Sens.*, *34*, 189–200, 1996.

Kwok, R., A. Schweiger, D. A. Rothrock, S. Pang, and C. Kottmeier, Sea ice motion from satellite passive microwave imagery assessed with ERS SAR and buoy motions, *J. Geophys. Res.*, *103*, 8191–8214, 1998.

Lambeck, K., *Geophysical Geodesy: The Slow Deformations of the Earth*, 718 pp., Clarendon Press, Oxford, 1988.

Lanari, R., P. Lundgren, and E. Sansosti, Dynamic deformation of Etna volcano observed by satellite radar interferometry, *Geophys. Res. Lett.*, *25*, 1541–1544, 1998.

Langbein, J., D. Dzurisin, G. Marshall, R. Stein, and J. Rundle, Shallow and peripheral volcanic sources of inflation revealed by modeling two-color geodimeter and leveling data from Long Valley caldera, California, 1988–1992, *J. Geophys. Res.*, *100*, 12,487–12,496, 1995.

Li, F. K., and R. M. Goldstein, Studies of multibaseline spaceborne interferometric synthetic aperture radars, *IEEE Trans. Geosci. Remote Sens.*, *28*, 88–97, 1990.

Lin, Q., J. Vesecky, and H. Zebker, New approaches in interferometric SAR data processing, *IEEE Trans. Geosci. Remote Sens.*, *30*, 560–567, 1992.

Lin, Q., J. F. Vesecky, and H. A. Zebker, Phase unwrapping through fringe-line detection in synthetic aperture radar interferometry, *Appl. Opt.*, *33*, 201–208, 1994.

Llubes, M., and P. Mazzega, The ocean tide gravimetric loading reconsidered, *Geophys. Res. Lett.*, *23*, 1481–1484, 1996.

Lu, Z., R. Fatland, M. Wyss, S. Li, J. Eichelberger, K. Dean, and J. Freymuller, Deformation of New Trident volcano measured by ERS-1 SAR interferometry, Katmai National Park, Alaska, *Geophys. Res. Lett.*, *24*, 695–698, 1997.

Madsen, S. N., J. M. Martin, and H. A. Zebker, Analysis and evaluation of the NASA/JPL TOPSAR across-track interferometric SAR system, *IEEE Trans. Geosci. Remote Sens.*, *33*, 383–391, 1995.

Madsen, S. N., N. Skou, J. Granholm, K. W. Woelders, and E. L. Christensen, System for airborne SAR interferometry, *Int. J. Electron. Commun.*, *50*, 106–111, 1996.

Marom, M., R. M. Goldstein, E. B. Thorton, and L. Shemer, Remote sensing of ocean wave spectra by interferometric synthetic aperture radar, *Nature*, *345*, 793–795, 1990.

Marom, M., L. Shemer, and E. B. Thornton, Energy density directional spectra of a nearshore wave field measured by interferometric synthetic aperture radar, *J. Geophys. Res.*, *96*, 22,125–22,134, 1991.

Marroquin, J., and M. Rivera, Quadratic regularization functionals for phase unwrapping, *J. Opt. Soc. Am. A Opt. Image Sci.*, *12*, 2393–2400, 1995.

Marshall, G. A., J. Langbein, R. S. Stein, M. Lisowski, and J. Svarc, Inflation of Long Valley Caldera, California, Basin and Range strain, and possible Mono Craters dike opening from 1990–94 GPS surveys, *Geophys. Res. Lett.*, *24*, 1003–1006, 1997.

Massonnet, D., Etude de principe d'une détection de mouvements tectoniques par radar, *Int. Memo. 326*, Cent. Natl. d'Etudes Spatiales, Toulouse, France, 1985.

Massonnet, D., FOCUS: An experiment for high resolution radar imagery, elevation terrain model derivation, Earth small move detection, in *Remote Sensing Science for the Nineties*, *Proceedings of the International Geoscience and Remote Sensing Symposium*, vol. 2, *IEEE Publ. 90CH2825-8*, pp. 1431–1434, Inst. of Elect. and Electron. Eng., Piscataway, N. J., 1990.

Massonnet, D., Geoscientific applications at CNES, in *SAR Geocoding: Data and Systems*, edited by G. Schreier, chap. 18, pp., 397–415, Wichmann, Karlsruhe, Germany, 1992.

Massonnet, D., Giving an operational status to SAR interferometry, paper presented at ERS-1 Pilot Project Workshop, Eur. Space Agency, Toledo, Spain, June 1994.

Massonnet, D., and K. L. Feigl, Discriminating geophysical phenomena in satellite radar interferograms, *Geophys. Res. Lett.*, *22*, 1537–1540, 1995a.

Massonnet, D., and K. L. Feigl, Satellite radar interferometric map of the coseismic deformation field of the $M = 6.1$ Eureka Valley, California, earthquake of May 17, 1993, *Geophys. Res. Lett.*, *22*, 1541–1544, 1995b.

Massonnet, D., and T. Rabaute, Radar interferometry: Limits

and potential, *IEEE Trans. Geosci. Remote Sens*., *31*, 455–464, 1993.

Massonnet, D., B. Rogron, and C. Carmona, Evaluation des changements de phase de surface sur des grandes zones, in *De l'Optique au Radar, les Applications de SPOT et ERS*, pp. 473–482, Cépaudès, Paris, 1993a.

Massonnet, D., M. Rossi, C. Carmona, F. Adragna, G. Peltzer, K. Feigl, and T. Rabaute, The displacement field of the Landers earthquake mapped by radar interferometry, *Nature*, *364*, 138–142, 1993b.

Massonnet, D., K. L. Feigl, M. Rossi, and F. Adragna, Radar interferometric mapping of deformation in the year after the Landers earthquake, *Nature*, *369*, 227–230, 1994a.

Massonnet, D., M. Rossi, and F. Adragna, CNES General-purpose SAR correlator, *IEEE Trans. Geosci. Remote Sens*., *32*, 636–643, 1994b.

Massonnet, D., P. Briole, and A. Arnaud, Deflation of Mount Etna monitored by spaceborne radar interferometry, *Nature*, *375*, 567–570, 1995a.

Massonnet, D., H. Vadon, and C. Carmona, ERS-1 internal clock drift measured by interferometry, *IEEE Trans. Geosci. Remote Sens*., *33*, 401–408, 1995b.

Massonnet, D., K. L. Feigl, H. Vadon, and M. Rossi, Coseismic deformation field of the $M = 6.7$ Northridge, California, earthquake of January 17, 1994, recorded by two radar satellites using interferometry, *Geophys. Res. Lett*., *23*, 969–972, 1996a.

Massonnet, D., W. Thatcher, and H. Vadon, Detection of postseismic fault zone collapse following the Landers earthquake, *Nature*, *382*, 612–616, 1996b.

Massonnet, D., H. Vadon, and M. Rossi, Reduction of the need for phase unwrapping in radar interferometry, *IEEE Trans. Geosci. Remote Sens*., *34*, 489–497, 1996c.

Massonnet, D., T. Holzer, and H. Vadon, Land subsidence caused by the East Mesa geothermal field, California, observed using SAR interferometry, *Geophys. Res. Lett*., *24*, 901–904, 1997. (Correction, *Geophys. Res. Lett*., *25*, 3213, 1998.)

McLeod, I. H., I. G. Cumming, and M. S. Seymour, ENVISAT ASAR data reduction—Impact on SAR interferometry, *IEEE Trans. Geosci. Remote Sens*., *36*, 589–602, 1998.

Melchior, P., *The Tides of the Planet Earth*, 641 pp., *Pergamon*, Tarrytown, N. Y., 1983.

Meyer, B., R. Armijo, D. Massonnet, J. B. de Chabalier, C. Delacourt, J. C. Ruegg, J. Achache, P. Briole, and D. Panastassiou, The 1995 Grevena (northern Greece) earthquake: Fault model constrained with tectonic observations and SAR interferometry, *Geophys. Res. Lett*., *23*, 2677–2680, 1996.

Mogi, K., Relations between the eruption of various volcanoes and the deformations of the ground surfaces around them, *Bull. Earthquake Res. Inst. Univ. Tokyo*, *36*, 99–134, 1958.

Moreira, J., et al., X-SAR interferometry: First results, *IEEE Trans. Geosci. Remote Sens*., *33*, 950–956, 1995.

Murakami, M., M. Tobita, S. Fujiwara, T. Saito, and H. Masaharu, Coseismic crustal deformations of the 1994 Northridge, California, earthquake detected by interferometric JERS 1 synthetic aperture radar, *J. Geophys. Res*., *101*, 8605–8614, 1996.

Murray, M. H., J. C. Savage, M. Lisowski, and W. K. Gross, Coseismic displacements: 1992 Landers, California, Earthquake, *Geophys. Res. Lett*., *20*, 623–626, 1993.

Nunnari, G., and G. Puglisi, Ground deformation studies during the 1991–1993 Etna eruption using GPS data, *Acta Vulcanol*., *4*, 101–107, 1994.

Nur, A., Dilatancy, pore fluids, and premonitory motions of t_s/t_p travel times, *Bull. Seismol. Soc. Am*., *62*, 1217–1222, 1972.

Nur, A., and J. R. Booker, Aftershocks caused by pore fluid flow?, *Science*, *175*, 885–887, 1972.

Okada, Y., Surface deformation to shear and tensile faults in a half-space, *Bull. Seismol. Soc. Am*., *75*, 1135–1154, 1985.

Orwig, L. P., A. D. Aronoff, P. M. Ibsen, H. D. Maney, J. D. O'Brien, and H. D. Holt Jr., Wide-area terrain surveying with interferometric SAR, *Remote Sens. Environ*., *53*, 97–108, 1995.

Owen, S., P. Segall, J. Freymueller, A. Miklius, R. Denlinger, T. Arandóttir, M. Sako, and R. Burgmann, Rapid deformation of the south flank of Kilauea volcano, Hawaii, *Science*, *267*, 1328–1322, 1995.

Ozawa, S., M. Murakami, S. Fujiwara, and M. Tobita, Synthetic aperture radar interferogram of the 1995 Kobe earthquake and its geodetic inversion, *Geophys. Res. Lett*., *24*, 2327–2330, 1997.

Padgett, D., and T. Rockwell, Timing of past earthquakes and triggered slip events on the Lenwood fault at Soggy Lake playa relative to 1992 Landers triggered slip (abstract), *Eos Trans. AGU*, *74*(43), Fall Meet. Suppl., 68, 1993.

Pandit, S. M., N. Jordache, and G. A. Joshi, Data-dependent systems methodology for noise-insensitive phase unwrapping in laser interferometric surface characterization, *J. Opt. Soc. Am*., *A Opt. Image Sci*., *11*, 2584–2592, 1994.

Parker, B. B., *Tidal Hydrodynamics*, 883 pp., John Wiley, New York, 1991.

Peltzer, G., and P. Rosen, Surface displacement of the 17 May 1993 Eureka Valley, California, earthquake observed by SAR interferometry, *Science*, *268*, 1333–1336, 1995.

Peltzer, G., P. Rosen, F. Rogez, and K. Hudnut, Postseismic rebound in fault step-overs caused by pore fluid flow, *Science*, *273*, 1202–1204, 1996.

Peltzer, G., P. Rosen, F. Rogez, and K. Hudnut, Poro-elastic rebound along the Landers 1992 earthquake surface rupture, *J. Geophys. Res*., in press, 1998.

Posner, F. L., Texture and speckle in high resolution synthetic aperture radar clutter, *IEEE Trans. Geosci. Remote Sens*., *31*, 192–203, 1993.

Prati, C., and F. Rocca, Improving slant-range resolution with multiple SAR surveys, *IEEE Trans. Aerosp. Electron. Syst*., *29*, 135–143, 1993.

Prati, C., F. Rocca, A. Guarnieri, and E. Damonti, Seismic migration for SAR focusing: Interferometric applications, *IEEE Trans. Geosci. Remote Sens*., *28*, 627–640, 1990.

Prati, C., F. Rocca, Y. Kost, and E. Damonti, Blind deconvolution for Doppler centroid estimation in high frequency SAR, *IEEE Trans. Geosci. Remote Sens*., *29*, 934–941, 1991.

Price, E. J., and D. T. Sandwell, Small-scale deformations associated with the 1992 Landers, California, earthquake mapped by InSAR phase gradients, *J. Geophys. Res*., in press, 1998.

Pritt, M. D., Phase unwrapping by means of multigrid techniques for interferometric SAR, *IEEE Trans. Geosci. Remote Sens*., *34*, 728–738, 1996.

Raney, R. K., Synthetic aperture imaging radar and moving targets, *IEEE Trans. Aerosp. Electron. Syst*., *AES-7*, 499–505, 1971.

Raney, R. K., An "exact" wide field digital imaging algorithm, *Int. J. Remote Sens*., *13*, 991–998, 1991.

Raney, R. K., H. Runge, R. Bamler, I. G. Cumming, and F. H. Wong, Precision SAR processing using chirp scaling, *IEEE Trans. Geosci. Remote Sens*., *32*, 786–799, 1994.

Rignot, E., Dual-frequency interferometric SAR observations of a tropical rain forest, *Geophys. Res. Lett*., *23*, 993–996, 1996.

Rignot, E. J., Fast recession of a West Antarctic glacier, *Science*, *281*, 549–551, 1998.

Rignot, E., K. C. Jezek, and H. G. Sohn, Ice flow dynamics of

the Greenland ice sheet from SAR interferometry, *Geophys. Res. Lett*., *22*, 575–578, 1995.
Rosen, P. A., S. Hensley, H. A. Zebker, F. H. Webb, and E. J. Fielding, Surface deformation and coherence measurements of Kilauea volcano, Hawaii, from SIR-C radar interferometry, *J. Geophys. Res*., *101*, 23,109–23,125, 1996.
Rosen, P., C. Werner, E. Fielding, S. Hensley, S. Buckley, and P. Vincent, Aseismic creep along the San Andreas fault northwest of Parkfield, California, measured by radar interferometry, *Geophys. Res. Lett*., *25*, 825–828, 1998.
Rossi, M., B. Rogron, and D. Massonnet, JERS-1 SAR image quality and interferometric potential, *IEEE Trans. Geosci. Remote Sens*., *34*, 824–827, 1996.
Sandwell, D. T., and E. J. Price, Multiple pass INSAR processing for geophysical applications: Stack phase gradient then unwrap (abstract), *Eos Trans. AGU*, *77*(46), Fall Meet. Suppl., F52, 1996.
Savage, J. C., M. Lisowski, and J. L. Svarc, Postseismic deformation following the 1989 (M = 7.1) Loma Prieta, California, earthquake, *J. Geophys. Res*., *99*, 13,757–13,765, 1994.
Scharroo, R., and P. N. Visser, Precise orbit determination and gravity field improvement for the ERS satellites, *J. Geophys. Res*., *103*, 8113–8127, 1998.
Schmidt, A., and M. Bao, The modulation of radar backscatter by long ocean waves: A quadratically nonlinear process?, *J. Geophys. Res*., *103*, 5551–5562, 1998.
Scholz, C. H., *Earthquakes and Fault Mechanics*, 439 pp., Cambridge Univ. Press, New York, 1990.
Segall, P., and J. L. Davis, GPS applications for geodynamics and earthquake studies, *Annu. Rev. Earth. Planet. Sci*., *25*, 301–336, 1997.
Shapiro, I. I., S. H. Zisk, A. E. E. Rogers, M. A. Slade, and T. W. Thompson, Lunar topography: Global determination by radar, *Science*, *178*, 939–948, 1972.
Shemer, L., Analytical presentation of the monochromatic ocean wave image by a regular or an interferometric synthetic aperture radar, *IEEE Trans. Geosci. Remote Sens*., *33*, 1008–1013, 1995.
Shemer, L., and E. Kit, Simulation of an interferometric synthetic aperture radar imagery of an ocean system consisting of a current and a monochromatic wave, *J. Geophys. Res*., *96*, 22,063–22,073, 1991.
Shemer, L., M. Marom, and D. Markman, Estimates of currents in the nearshore ocean region using interferometric synthetic aperture radar, *J. Geophys. Res*., *98*, 7001–7010, 1993.
Shen, Z., D. Jackson, Y. Feng, M. Kim, and M. Cline, Postseismic deformation following the 1992 Landers earthquake, *Bull. Seismol. Soc. Am*., *84*, 780–791, 1994.
Shen, Z. K., B. X. Ge, D. D. Jackson, D. Potter, M. Cline, and L. Y. Sung, Northridge earthquake rupture models based on the Global Positioning System measurements, *Bull. Seismol. Soc. Am*., *86*, 537–548, 1996.
Showstack, R., Radarsat survey provides accurate map of Antarctica, *Eos Trans. AGU*, *78*, 461, 1997.
Sieh, K., et al., Near-field investigations of the Landers earthquake sequence, April to July 1992, *Science*, *260*, 171–167, 1993.
Sigmundsson, F., H. Vadon, and D. Massonnet, Readjustment of the Krafla spreading center segment to crustal rifting measured by satellite radar interferometry, *Geophys. Res. Lett*., *24*, 1843–1846, 1997.
Sleep, N. H., and M. L. Blanpied, Creep, compaction, and the weak rheology of major faults, *Nature*, *359*, 687–692, 1992.
Smithsonian Institution, *Global Volcanism Network Bull. 16–18*, Washington, D. C., 1991–1993.
Snyder, J. P., *Map Projections Used by the U.S. Geological Survey*, 2nd ed., 313 pp., *U.S. Geol. Surv. Bull., 1532*, 1992.
Song, S. M.-H., S. Napel, N. J. Pelc, and G. H. Glover, Phase unwrapping of MR phase images using poisson equation, *IEEE Trans. Image Process*., *4*, 667–676, 1995.
Stacy, N. J. S., and D. B. Campbell, Earth-based measurement of lunar topography using delayed radar, *Proc. Lunar Planet. Sci. Conf*., *24th*(3), 1343–1344, 1993.
Stein, R. S., G. C. P. King, and J. Lin, Change in failure stress on the southern San Andreas fault system caused by the 1992 magnitude = 7.4 Landers earthquake, *Science*, *258*, 1328–1332, 1992.
Stevens, D. R., I. G. Cumming, and A. L. Gray, Options for airborne interferometric SAR motion compensation, *IEEE Trans. Geosci. Remote Sens*., *33*, 409–420, 1995.
Talbot, C. J., Extrusions of Hormuz salt in Iran, in *Lyell: The Past is the Key to the Present*, edited by D. J. Blundell and A. C. Scott, *Geol. Soc. Spec. Publ*., *143*, 315–334, 1998.
Tarayre, H., Extraction de modèles numériques de terrain par interférométrie radar satellitaire: Algorithmie et artefacts atmosphériques, Ph.D. thesis, 230 pp., Inst. Natl. Polytec. de Toulouse, Toulouse, France, 1994.
Tarayre, H., and D. Massonnet, Atmospheric propagation heterogeneities revealed by ERS-1 interferometry, *Geophys. Res. Lett*., *23*, 989–992, 1996.
Thatcher, W., and D. Massonnet, Crustal deformation at Long Valley caldera, eastern California, 1992–1996 inferred from satellite radar interferometry, *Geophys. Res. Lett*., *24*, 2519–2522, 1997.
Thompson, D. R., and J. R. Jensen, Synthetic aperture radar interferometry applied to ship-generated internal waves in the 1989 Loch Linnbe experiment, *J. Geophys. Res*., *98*, 10,259–10,269, 1993.
Trouvé, E., Imagerie differentielle en radar à ouverture synthétique, Ph.D., Ecole Natl. Super. de Telecommun., Paris, 1996.
U.S. Geological Survey (USGS), Rodman Mountains quadrangle, 15 minute series (topographic), map, Denver, Colo., 1955.
U.S. Geological Survey (USGS), *Digital elevation models: Data users guide 5*, 34 pp., U.S. Gov't Print. Off., Washington, D. C., 1993.
U.S. Geological Survey (USGS) and Southern California Earthquake Center, The magnitude 6.7 Northridge, California, earthquake of January 17, 1994, *Science*, *266*, 389–397, 1994.
U.S. Geological Survey (USGS) Staff, Pattern of surface ruptures associated with the June 28, 1992, Landers earthquake, *Eos Trans. AGU*, *73*(43), Fall Meet. Suppl., 357–358, 1992.
Vachon, P. W., D. Geudtner, A. L. Gray, and R. Touzi, ERS-1 synthetic aperture radar repeat-pass interferometry studies: Implications for RADARSAT, *Can. J. Remote Sens*., *21*, 441–454, 1995.
Vadon, H., and F. Sigmundsson, 1992–1995 Crustal deformation at Mid-Atlantic ridge, SW Iceland, mapped by radar interferometry, *Science*, *275*, 194–197, 1997.
Villari, L. (Ed.), The 1991–1993 Etna eruption, *Acta Vulcanol*., *4*, 1–177, 1994.
Vincent, P., and J. Rundle, Synthetic aperture radar interferometry capability now available to universities, *Eos Trans. AGU*, *79*, 34, 1998.
Wald, D. J., and T. H. Heaton, Spatial and temporal distribution of slip for the 1992 Landers, California earthquake, *Bull. Seismol. Soc. Am*., *84*, 668–691, 1994.
Wald, D. J., T. H. Heaton, and K. W. Hudnut, A dislocation model of the 1994 Northridge, California, earthquake determined from strong-motion, GPS and leveling-line data, *Bull. Seismol. Soc. Am*., *86*, S49–S70, 1996.
Wegmuller, U., and C. Werner, Retrieval of vegetation param-

eters with SAR interferometry, *IEEE Trans. Geosci. Remote Sens.*, *35*, 18–24, 1997.

Wicks, C., W. Thatcher, and D. Dzurisin, Migration of fluids beneath Yellowstone caldera inferred from satellite radar interferometry, *Science*, in press, 1998.

Williams, C. A., and G. Wadge, The effects of topography on magma chamberinflation models: Application to Mt. Etna and radar interferometry, *Geophys. Res. Lett.*, *25*, 1549–1552, 1998.

Wolf, M., and D. Wingham, The status of the world's public-domain digital topography of the land and ice, *Geophys. Res. Lett.*, *19*, 2325–2328, 1992.

Wu, C., B. Barkan, B. Huneycutt, C. Leans, and S. Pang, An introduction to the interim digital SAR processor and the characteristics of the associated Seasat SAR imagery, *JPL Publ.*, *81-26*, 123 pp., 1981.

Zebker, H., and R. Goldstein, Topographic mapping from interferometric SAR observations, *J. Geophys. Res.*, *91*, 4993–5001, 1986.

Zebker, H. A., P. A. Rosen, R. M. Goldstein, A. Gabriel, and C. L. Werner, On the derivation of coseismic displacement fields using differential radar interferometry: The Landers earthquake, *J. Geophys. Res.*, *99*, 19,617–19,634, 1994a.

Zebker, H. A., J. F. Vesecky, and Q. Lin, Phase wrapping through fringe-line detection in synthetic in synthetic aperture radar interferometry, *Appl. Opt.*, *33*, 201–208, 1994b.

Zebker, H. A., C. L. Werner, P. A. Rosen, and S. Hensley, Accuracy of topographic maps derived from ERS-1 interferometric radar, *IEEE Trans. Geosci. Remote Sens.*, *32*, 823–836, 1994c.

Zebker, H. A., P. A. Rosen, and S. Hensley, Atmospheric effects in interferometric synthetic aperture radar surface deformation and topographic maps, *J. Geophys. Res.*, *102*, 7547–7563, 1997.

Zisk, S. H., Lunar topography; First radar-interferometer measurements of the Alphonsus-Ptolemaeus-Arzachel Region, *Science*, *178*, 977–980, 1972a.

Zisk, S. H., A new, Earth-based radar technique for the measurement of lunar topography, *Moon*, *4*, 296–306, 1972b.

K. L. Feigl, Department of Terrestrial and Planetary Dynamics, Unité Mixte de Recherche 5562, Centre National de la Recherche Scientifique, 14, avenue Edouard Belin, 31400 Toulouse, France. (e-mail: kurt.feigl@cnes.fr).

D. Massonnet, Department of Radar Systems Performance, Centre National d'Etudes Spatiales, 18, avenue Edouard Belin, 31041 Toulouse Cedex 4, France. (e-mail: didier.massonnet@cnes.fr).